EXPERIMENTAL CHARACTERIZATION OF SHAPE MEMORY ALLOYS USING DIGITAL IMAGE CORRELATION AND INFRA-RED THERMOGRAPHY

A Thesis

by

STEPHEN ROBERT CORNELL

Submitted to the Office of Graduate and Professional Studies of
Texas A&M University
in partial fulfillment of the requirements for the degree of

MASTER OF SCIENCE

Chair of Committee,	Dimitris C. Lagoudas
Co-Chair of Committee,	Darren J. Hartl
Committee Member,	Ibrahim Karaman
Head of Department,	Rodney Bowersox

May 2015

Major Subject: Aerospace Engineering

ABSTRACT

Characterization of shape memory alloy materials is demonstrated using modern full-field experimental techniques. The methods presented are designed to reduce the number of experiments required for full characterization of the material. Several experiments have been explored in this work; for each type of experiment, particular attention has been given to the particular measurement methods that have been utilized. For characterization of shape memory alloys as actuators, a new experimental method has been presented as an alternative to testing multiple separate specimens or performing several experiments on the same specimen. For the actuator material experiments, temperature was measured using infra-red thermography with an accuracy of up to 2.14 °C, and a resolution of 0.39 mm. Strain was measured using digital image correlation (DIC) with a resolution of 0.09 mm. For pseudoelastic shape memory alloy material characterization, experiments have been designed which provide data demonstrating the anisotropic behavior of the material, which are not shown by previous methods of characterization. For these experiments, the DIC measurement had a resolution of 0.08 mm. For microscopic shape memory alloy applications, particular in-situ characterization has been demonstrated which is not possible by traditional methods of characterization. DIC measurements were performed simultaneously at a micro-scale with a resolution of 0.25 μm and at a macro-scale with a resolution of 0.022 mm. The information provided herein presents these experiments in great detail in order to demonstrate characterization methods which are currently the most reliable and efficient for analysis of shape memory alloy materials.

ACKNOWLEDGEMENTS

This thesis work contains a synopsis of my graduate studies at Texas A&M University. I am sincerely indebted to the many research professors and scholars that I have worked with who provided key contributions, ideas, suggestions, and guidance to produce this completed work.

First, I would like to thank my committee chairs, Dr. Darren Hartl and Dr. Dimitris Lagoudas. Dr. Hartl has supported and guided my work from the beginning until now. In every project and experimental study, his suggestions and ideas have helped to drive me forward, and he has kept me oriented so that my research will have the most significant impact in my research field. He has been both an advisor and my primary mentor. Dr. Hartl has always taken a special effort to strengthen my research endeavors and encourage my further effort. Dr. Dimitris Lagoudas has been a great help to me as my advisor, and has always provided sincere guidance for the direction that I have taken in my work. He has always given me challenges related to my research to which I should direct my efforts. I sincerely appreciate his experience and wisdom concerning how to conduct effective and impactful research, and his support of my work. I would also like to thank my committee member Dr. Ibrahim Karaman for his support of all of my research at Texas A&M. Being satisfied with nothing less than a professional, clearly presented and impactful product of research, these members of my committee have been the foundation of all my work.

The experiments demonstrated in Section 3 were performed through a student exchange program at Arts et Métiers ParisTech University in Metz, France. This research was a collaborative effort between scholars at Arts et Métiers ParisTech University and Texas A&M University. All experiments and simulations were per-

formed at Arts et Métiers ParisTech University under the guidance of Yves Chemisky, Fodil Meraghni, and Etienne Patoor.

Dr. Yves Chemisky, my advisor during internship in Metz, France, has been an adamant supporter and guide since my stay in Metz. Dr. Meraghni has also always been eager to support my research and encourage my further studies.

I would also like to thank Dr. Jacob Hochhalter for sponsoring my stay at NASA Langley Research Center, and for his unequivocal support for every aspect of my work and research. It was a great privilege to work with Dr. Hochhalter, and the researchers of the Durability, Damage Tolerance and Reliability Branch at NASA Langley.

I am especially grateful to Mr. James Mabe for his unwavering support, especially for his help with my experiments at Texas A&M. He was constantly patient and understanding, and with his wisdom from so many years of experience he introduced me to many basic procedures in the lab in order to inspire me to design my own experiments; he has always encouraged me to drive my research forward.

Finally, I would like to thank and acknowledge all of my colleagues, coworkers, and classmates. Brian Lester, Majid Tabesh, and Babatunde Agboola, my senior lab mates, have always been eager to help me work through challenges in my research, brainstorm with me, and even help to provide comments on my papers and presentations. Thanks also to Rob Wheeler, my office mate, who always seemed to know the answer whenever I couldn't quite figure it out. Thank you to all of the students in the TiiMS group, who have always been a great support to me. I would also like to thank my co-mentor and co-workers at NASA Langley, Dr. Andy Newman and Paul Leser and others, for their help and support in my work.

TABLE OF CONTENTS

LIST OF FIGURES

FIGURE Page

LIST OF TABLES

TABLE Page

1. INTRODUCTION

1.1 Motivation

Experimental methods for characterizing shape memory alloy (SMA) materials are the focus of the work presented in this thesis. The work was motivated by a need for more suitable methods for characterization which utilize modern measurement and combined measurement/ computation techniques to optimize the process of material characterization. Due to the fact that the behavior of SMAs is highly dependent on the application intended for the particular SMA material in question, the work review herein was performed from several separate standpoints, each based on a different intended application of the material system. In particular, three sets of experiments were performed, each separate and distinct from the next. This introductory section provides a review of measurement techniques and of past characterization methods and other concepts, as well as an introduction to each experimental method. First, experiments were performed which demonstrate an experimental technique for characterizing SMAs as would be used for actuation devices. Second, experiments were demonstrated which are ideal for characterizing SMAs utilized in the pseudoelastic sense as dampening or sensing mechanisms. Finally, a method to characterize microscopic SMAs for use as sensory particles embedded within a structural material is reviewed.

1.2 A definition of shape memory alloys

Shape memory alloys (SMAs) are a class of material that are able to be restored to a set shape even after severe non-linear deformations (D. Lagoudas (2008), ch. 1). These deformations may be achieved via either stress or temperature induced diffusionless phase transformation between two solid phases (J. A. Shaw & Kyri-

akides, 1995). Under sufficient load at a sufficiently cool temperature, SMA material regions in the low temperature *martensite* phase may be induced to reconfigure their many martensitic variants into a load-favored assembly, which remain after the load is removed. Sufficient heating will transform the regions toward the parent high temperature *austenite* phase, eliminating the load-favored variants and restoring the original shape. This is known as the *shape memory effect*. Furthermore, when a material is initially in austenite (i.e., it is at a sufficiently high temperature), it may experience large non-linear deformations when a load is applied as the stress induces phase transformation to martensite. If the material has been properly processed, these deformations may be completely recovered upon unloading and this effect is known as *pseudoelasticity*. These two phenomena (shape memory effect and pseudoelasticity) are used widely in different types of applications. Classified by the phenomenon employed, SMA actuators can be designed by taking advantage of the shape memory effect (SME); SMA pseudoelasticity is utilized in applications for dampening, vibration control, and sensing.

Figure 1.1 shows a phase diagram schematic typical for SMA materials, and demonstrates the temperature and stress-induced phase transformation loading path variations. For example, consider the SMA thermally induced actuation loading path, $\alpha - \beta - \gamma - \delta - \varepsilon$. Describing the transformation behavior according to four descriptive phase transformation boundaries: when the material is cooled at a applied stress level from austenite to below the martensite start temperature (M_s) at point β, the material begins forward transformation from austenite to martensite. When the temperature is below martensite finish (M_f), point γ, the material is fully-martensite. When the material is reheated and reaches the austenite start (A_s) temperature at point δ, reverse transformation begins. The material returns to the parent austenite phase when the temperature is above austenite finish (A_f) at

point ε. From the standpoint of stress induced pseudoelastic loading indicated by points $1-2-3-4-5$ in Figure 1.1, the material undergoes forward transformation from zero load under a high temperature (point 1) from the stress level of the M_s boundary (point 2) until a load above the M_f boundary (point 3). During unloading, reverse transformation will occur when the load is between the A_s (point 4) and A_f (point 5) boundaries. As phase transformation occurs for both temperature and stress induced transformation, the martensitic volume fraction (ξ) changes from zero as austenite to unity as martensite. This parameter is useful for describing the state of the material, and is especially used in constitutive modeling of the material (D. Lagoudas, Hartl, Chemisky, Machado, & Popov, 2012) which will be discussed in a later section. As phase transformation occurs in the material, ξ changes between zero and unity linearly with either temperature or stress.

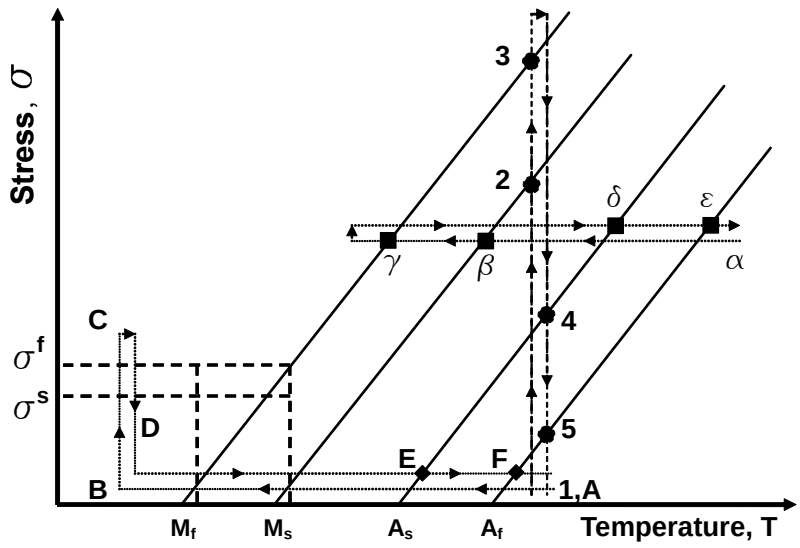

Figure 1.1: Phase diagram schematic showing temperature induced and stress induced loading paths for SMA (D. J. Hartl & Lagoudas, 2007).

Furthermore, SMA phase transformation occurs as a solid-to-solid phase transformation between the austenite and martensite phases. The austenite phase, or high temperature parent phase, exhibits a highly ordered cubic microstructure. The low temperature martensite phase has a tetragonal or monoclinic microstructure. Furthermore, for temperature induced load-free forward transformation, the crystal structure adopts an energetically favorable twinned configuration (Otsuka & Wayman, 1999) (Patoor, Lagoudas, Entchev, Brinson, & Gao, 2006) (D. C. Lagoudas et al., 2006). When a critical level of stress is applied to the cooled material, the martensite variants become reoriented causing severe non-linear displacements which are recovered upon reheating. This behavior is seen by path $A-B-C-D-E-F$ in Figure 1.1. For stress-induced forward transformation, reorientation of the martensitic varients occurs as a consequence to the load applied for phase transformation, and again the resulting severe non-linear displacements are recovered upon unloading. An example of these phenomena is seen in Figure 1.2, which summarizes this discussion in a stress-strain-temperature space for an experiment performed on NiTiCu SMA material (D. J. Hartl & Lagoudas, 2007).

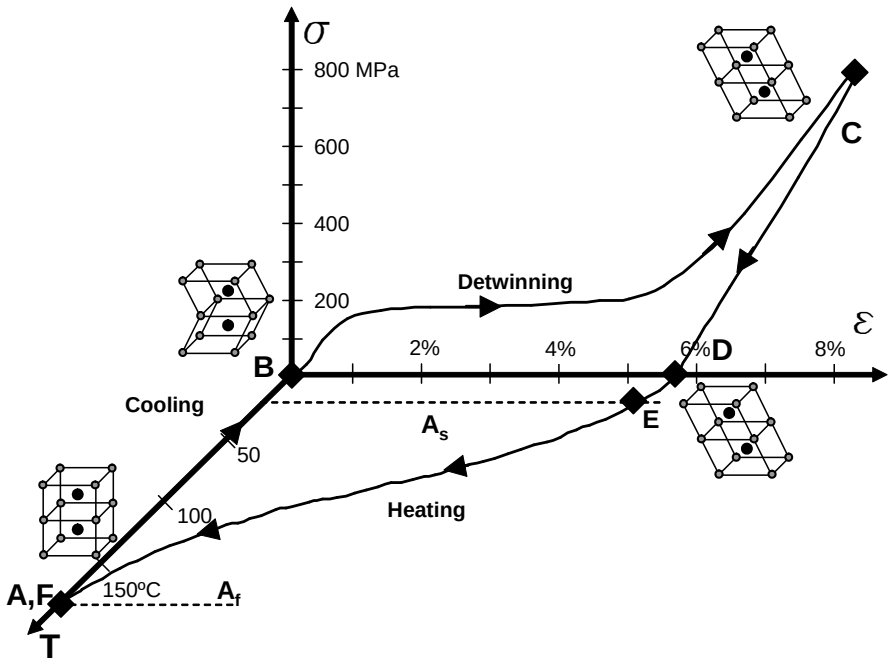

Figure 1.2: Example stress-strain-temperature curve for SMAs. An experiment performed for NiTiCu is shown (D. J. Hartl & Lagoudas, 2007).

It should be noted that several mechanical properties of the material depend on the SMA material phase. In the bulk material the martensite phase is generally an easily deformable, and seemingly low modulus material though this is partly due to the existence of a number of recoverable inelastic phenomena. The austenite phase on the other hand normally exhibits a modulus much greater than that of martensite, having a modulus comparable to that of aluminum. Additionally, the yield strength, CTE, and thermal and electrical conductivities all depend on the material phase. A comprehensive table of NiTi SMA material phase-dependent physical properties is included by Jani, Leary, Subic, and Gibson (2014).

1.3 Characterization methods for SMAs

Many efforts have been made in the past for characterization of SMA materials and identification of their material parameters (M_s, M_f, A_s, A_f and others). ASTM International has recorded some standards related to calibration of SMA parameters which were written primarily for pseudoelastic stress-induced transformation based loading of SMAs as used in the medical industry. ASTM Standard F2004 (2010) presents a standard for using differential scanning calorimetry to identify the transformation temperatures for an SMA specimen under no load. This is a widely used method for initial identification of an SMA material, and is especially useful to determine the range of temperature between the martensite and austenite finish temperatures (c.f. J. A. Shaw, Churchill, and Iadicola (2008)). Also, it is useful for comparing various alloy compositions, as well as different material processing techniques and heat treatments. However, this technique cannot be used exclusively for calibration of SMA material parameters because no stress is applied to the material in this method and only the parameters at zero load may be determined. ASTM Standard F2082 (2006) specifies a bend and free recovery test, which is an alternative method to determine transformation temperatures, however, once again no stress is applied to the material. Furthermore, in order to identify the parameters of an SMA material, construction of a stress-temperature SMA phase diagram must be performed (Meraghni et al., 2013) by testing the material isothermally under various loads, or isobarically under several temperatures depending on the application to be performed.

Methods which are not yet included in the records of internationally recognized standards organizations also exist for characterizing SMA materials. These make an effort to obtain more comprehensive response data for the material, especially

to characterize the material under various loads and temperatures. However, even these methods which are currently most commonly used for characterizing SMAs introduce several limiting factors, which are addressed in the experimental studies performed here.These include but may not be limited to the following:

1. *1-D specimen confuguration.* Characterization experiments for SMAs most commonly performed are limited to single dimensional geometries. A leading group on this topic is that of Shaw et al. who have performed a thorough multi-faceted study of characterization methods for SMAs (J. A. Shaw et al., 2008) (Churchill, Shaw, & Iadicola, 2009a) (Churchill, Shaw, & Iadicola, 2009b) (Churchill, Shaw, & Iadicola, 2010) (Reedlunn, Daly, Hector, Zavattieri, & Shaw, 2011). J. A. Shaw and Kyriakides (1995) demonstrates the authority in characterization of NiTi wire under pseudoelastic (isothermal) loading; in that work, the researchers performed DSC studies followed by a series of uniaxial tension testing of NiTi wire using uniaxial tension in liquid bath. They used a series of isothermal experiments to determine the behavior of the SMA wire material as it depends on temperature. However, single-dimensional experiments provide limited information about anisotropic material behavior, or about the highly coupled stress state characteristic of "multi-dimensional'' specimens.

2. *Uniform geometry.* In contrast not only to single dimensional specimens but also to any specimens with symmetric and rectangular geometries, an effort is made to go beyond uniformly specimen geometries and explore the use of non-uniform geometry in the characterization experiments. The benefit of such specimen types lies primarily in mimicking SMA devices which would have non-uniform geometry. In particular, the behavior under certain types of stress concentrations and loading schemes such as high amounts of shear are explored.

3. *Number of experiments required for characterization.* The nature of characterization experiments for SMAs until now has required multiple tests to be performed, and in many cases multiple specimens have been used. In the work performed by D. Hartl, Lagoudas, Calkins, and Mabe (2010), actuator SMA characterization was performed through a series of six separate constant-stress thermally loaded tests at various stress levels. For these experiments, the same material specimen was used for each test. Churchill et al. (2009a) performed a series of experiments on different uniaxial specimens. In both D. J. Hartl and Lagoudas (2007) and Churchill et al. (2009a) however, inconsistencies are introduced by performing characterization using multiple testing cycles. The testing performed in this work emphasizes mitigation of these adverse affects by performing characterization on single specimens which give sufficient information for full identification of the material's parameters.

1.4 Characterization of SMAs as actuators

The characterization method performed on SMA materials used for actuators is introduced in this section. SMA actuators have applications in a wide variety of fields, especially the automotive, aerospace, robotic, and biomedical fields (Jani et al., 2014). They demonstrate high energy, high strain, and low shock actuation while being very simplistic in design (Van Humbeeck, 1999). For example, SMA actuators in wire configurations are very common, and are used in both a straight wire configuration, which may perform actuating work via axial strains up to 6% even under loads exceeding 700 MPa, as well as in a helical spring configuration which may generate and recover actuation extensions of much more than 100%. Additionally, many SMA actuating systems employ more geometrically complex 2D and 3D configurations such as the variable geometry chevron (D. Hartl et al., 2010)

(D. J. Hartl, Mooney, Lagoudas, Calkins, & Mabe, 2010) (Oehler, Hartl, Lopez, Malak, & Lagoudas, 2012), the SMA medical heart stent (Morgan, 2004), and the reconfigurable rotor blade (Bushnell, Arbogast, & Ruggeri, 2008), among others.

Some recent reviews exist concerning SMA actuator devices. D. J. Hartl and Lagoudas (2007) as well as Calkins and Mabe (2010) present reviews of recent applications of SMA actuators in the aerospace community. Jani et al. (2014) includes a highly inclusive review of possible and existing applications of SMAs across disciplines, addresses recent developments in SMA research, and provides an overview of the existing types of SMAs. Van Humbeeck (1999) also presented a detailed overview of past applications of SMA actuators, organizing them into various categories including fashion, fasteners, micro-actuators, hybrid composites (adaptive materials), and damping mechanisms. SMA actuators may also be divided into two subgroups, as outlined by Otsuka and Wayman (1999), ch. 11: *i)* the SMA acts as both sensor and actuator, where the environment acts as a stimulus, as in safety control devices (Van Humbeeck, 1999); *ii)* the SMA is actively heated via a controlled power input to perform an actuation sequence.

The actuator material experimentes performed utilized a concept to obtain variable temperature-induced phase transformation on a single specimen. by such localized heating, sufficient data was obtained by testing of only a single specimen. THis one experiment provides more reliable data at a higher volume than the most detailed testing matrix for a single material for a single isobaric stress level.

Furthermore, two types of SMA actuation are possible. The *two-way shape memory effect (TWSME)* requires no load to demonstrate strain generation and recovery (*i.e.*, actuation), and it is known that high cyclic fatigue life is possible for such actuators (Jani et al., 2014). To induce the TWSME in an SMA, the material must undergo a training procedure which is tailored to the specific application of the ac-

tuator. On the other hand, the *one-way shape memory effect (OWSME)* is often acceptable and even preferred for single-use actuators, where much larger actuation strains may be demonstrated (Jani et al., 2014). These OWSME actuators are normally in the form of untrained SMA components that have not previously been cycled. (D. J. Hartl & Lagoudas, 2007) (Jani et al., 2014)

1.5 Characterization of pseudoelastic shape memory alloys using non-uniform specimen geometry

The experiments performed for characterizing pseudoelastic SMAs is introduced in this section. The work presented in this section is to show the experimental results of uniaxial testing for a specimen shape with heterogeneous geometry.

Progressively more complex loading schemes may used to demonstrate material response to irregular loading, from uniaxial testing of SMA wire to biaxial loading of SMA cruxiform specimens. Pseudoelastic uniaxial tensile testing of SMA wire is widely accepted and published (J. A. Shaw & Kyriakides, 1995). Furthermore, Meraghni et al. (2013) demonstrated tension testing of non-wire dogbone shaped specimens.

Heterogeneously shaped specimens were tested at constant temperature in this unique testing concept for pseudoelastic SMAs. According to Avril et al. (2008), increasing the complexity of experimentation allows for identification of additional material parameters which may describe anisotropic material behavior, or phenomenon occuring due to inhomogeneity in the material specimen. Furthermore, more complex experiments allow for more information to be gathered from a fewer number of tests, and with increased reliability. The tests performed using non-uniform geometries were an attempt to address these issues.

1.6 Characterization of microscopic shape memory alloys

This section of this work is unique, as it is highly oriented to a specific application of the particular material being studied. Thus, instead of paying very close attention to the material characterization by a general method of study, a specific application is used as an example of the characterization process for this class of microscopic SMA materials; the concepts introduced by this work may be applied to characterize SMAs which have similar applications.

Figure 1.3 provides an illustration of the sensory particle concept. A sensory particle located near the crack tip has a response (mechanical, acoustic, magnetic, resistive) to the intensified stress field which can be detected using existing NDE methods. Various material systems may be used as sensory particles, allowing various NDE sensing methods to be incorporated. Some possible NDE methods include acoustic sensing of phase transformation in shape memory alloys (SMAs, e.g., NiTi) (Bogdanoff & Fultz, 2001), magnetic sensing of reorientation of martensitic variants in magnetic shape memory alloys (MSMAs, e.g., NiMnGa) (Karaca, Karaman, Basaran, Chumlyakov, & Maier, 2006), or detection of changes in resistance of piezoelectric materials (e.g.,$BaTiO_3$) (Hiruma, Aoyagi, Nagata, & Takenaka, 2004). In the present work, the NiTi shape memory alloy (SMA) was used as the sensory particle material, which emits an acoustic signal upon the onset of stress-induced martensitic phase transformation.

Characterization of the sensory particles is of primary concern to this work. In fact, this specific application of SMAs serves to demonstrate the power and utility of the characterization methods emphasized in this thesis. Specifically, a phenomenal application of the 3D-DIC displacement field measurement method was applied here by simultaneous measurement at both the micro-scale as well as the macro-scale.

The introduction of this technique was a major contribution of the study of this material characterization method.

1.7 A review of experimental deformation measurement techniques

Choice of appropriate experimental measurement methods is of primary interest to this work. Full-field measurement techniques have been nearly exclusively used, especially various forms of digital image correlation. Formerly, measurement techniques needed to be based upon the best available form of signal processing, which convert the mechanical response of the material to a form of voltage change. With increasing power of modern computational power, signal processing techniques such as strain gages, extensometers, laser extensometers, and thermocouples are no longer the most accurate and reliable forms of experimental measurements. It is more beneficial to obtain the most available information from the experiment, giving less attention to the computational cost to perform more detailed measurements. The

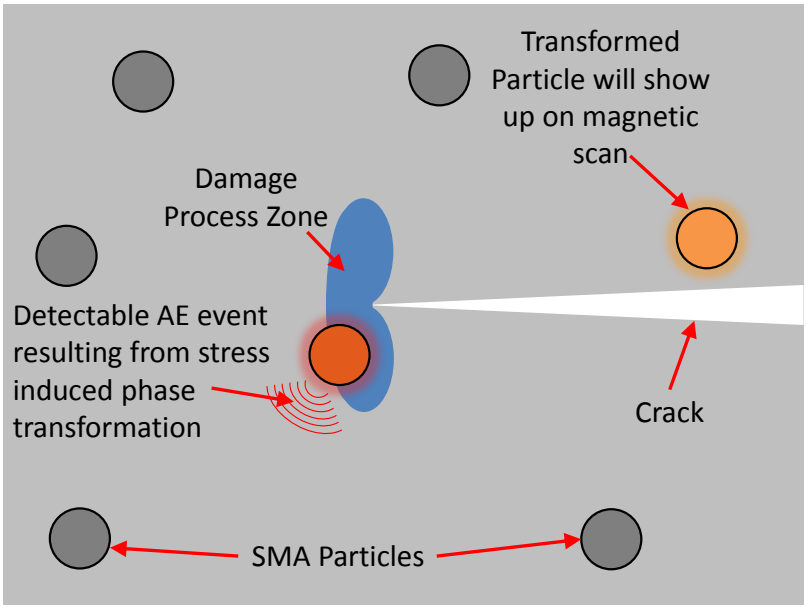

Figure 1.3: A schematic of the sensory particle concept.

following sections give an overview of the existing methods for strain measurement, as well as a detailed review of the digital image correlation method.

1.7.1 Photogrammetry

Full-field measurement techniques by image correlation is a type of photogrammetry, or measurements performed by comparison or two or more images. In 1480 Leonardo da Vinci wrote "Perspective is nothing else than the seeing of an object behind a sheet of glass, smooth and quite transparent, on the surface of which all things may be marked that are behind this glass. All things transmit their images to the eye by pyramidal lines, and these pyramids are cut by the said glass. The nearer to the eye these are intersected, the smaller the image of their cause will appear.'' (Doyle, 1964) This early quotation marks the beginning of the world of optical measurements, and is the basis for measurements performed by image correlation. After the invention of photography, the ideas set forth by Leonardo da Vinci became what is known as analytical photogrammetry through the works of S. Finsterwalder (1900), Von Gruber (1924), Earl Church (1930), Hellmut Schmid (1951), and Duane Brown (1957) (Doyle, 1964). Today, "photogrammetry'' most commonly refers to aerial photogrammetry which is a method of geographical mapping.

1.7.2 Moire strain measurement

An early version of image correlation is strain measurement by moiré analysis. First proposed for strain measurement by Weller and Shephard in 1948, Moiré is a phenomenon which occurs due to superimposing two or more patterns resulting in a mutual 'interference' which is a new pattern (Bromley, 1956). Moiré is used as a two-dimensional full-field strain measurement technique, utilized by identifying changes in regular patterns in thin fabrics, leather, or sheets. The patterns could be either naturally occurring (e.g., fabric weave or leather follicles) or could be imposed

on the material (e.g., a printed pattern on paper). The pattern must be a uniformly repeating pattern in all directions on the material. When the material is in its undeformed state, if a naturally occurring repeating pattern is not present, one may be printed. A record should be made of the reference pattern; this may be made by either taking a photograph of the pattern and printing it on a transparent material, or reproducing the pattern on a transparent material. The original pattern is compared to the deformed material in post processing. After deformation, the pattern will be warped, and measurements may be performed between the original and deformed images. Since the reference pattern is a uniformly repeated pattern, any irregularity in the deformation may be identified as irregularities in the new pattern created by superimposing the reference and deformed images. Today, Moiré is used primarily is microscopic strain measurement, especially utilized by the electron beam moiré or SEM moiré method (Dally & Read, 1993) (Zhao, Lei, Xing, Hou, & Bai, 2014) for which microscopic moiré-pattern gratings are drawn using the electron beam.

1.7.3 Video extensometry

Video extensometry (Francois, Gaucher, & Seguela, 1994) is a non-contact measurement technique for recording local deformations in real time. G'Sell, Hiver, Dahoun, and Souahi (1992) performed plastic deformation analysis of hourglass-shaped specimens of various materials, paying special attention to the necking phenomenon by recording and analyzing in real time the variation in the necking-region profile of the specimen by video recording; these tests were performed for various polymeric (which exhibit early necking behavior) as well as metallic ductile materials. Similarly, Francois et al. (1994) also demonstrated a similar method by recording the neck width profile of a specimen during tensile testing by video extensometry; a more complete review of the method is shown in this work. Both G'Sell et al. (1992)

and Francois et al. (1994) used these data to demonstrate the stress vs. strain behavior of the material, using the real-time profile data to simultaneously record the evolution of stress and strain during occurance of the necking phenomenon. As a parallel method, Coimbra, Greenwood, and Kendall (2000) tracked "extensometer'' markers on a thin ceramic fiber tensile test specimen via video recording and simultaneous real-time tracking, thus creating a non-contact method to replace traditional clip-on extensometers. Poulain et al. (2013) provides a direct comparison between three methods: the previously mentioned method used by G'Sell et al. (1992) and Francois et al. (1994), or video-based radial extensometry (VSE); the method used by Coimbra et al. (2000), or video-based surface extensometry (VRE); and digital image correlation. The methods were compared by testing a cylindrical dumbbell-shaped specimen, while simultaneously performing the three measurement methods. The results show that there is good agreement between the VSE and VRE methods but that the results differ at the onset of plastic deformation. The conclusion is that VSE is useful for measuring linear-elastic deformation, but not necessarily for after the onset of plastic yielding, particularly for compression testing; by contrast, VRE is quite useful to measure plastic yielding by measurement of the evolution of the necking profile, but may inaccurately depict deformations during linear-elastic deformation since the specimen profile will not undergo significant change. Finally, as the name "extensometer'' implies, both VSE and VRE are limited in their ability to measure localized deformation, and digital image correlation is recommended for such cases. In conclusion, both VSE and VRE provide excellent non-contact alternatives to clip-on extensometers or strain gages, but are not useful for measuring localized deformation.

1.7.4 Digital volume correlation

Digital volume correlation was proposed by Bay, Smith, Fyhrie, and Saad (1999) and is a method similar to digital image correlation. X-ray diffraction images of a volume during deformation are taken, and the motion of points inside a volume during deformation may be tracked, to provide a volume-based full-field 3D strain map. The method has been used for testing bone structures (Bay et al., 1999), geological structures (Lenoir, Bornert, Desrues, Bsuelle, & Viggiani, 2007), and volumetric analysis of composite materials (De Almeida, Lagattu, & Brillaud, 2008). However, this method is computationally expensive, and requires sophisticated x-ray imaging hardware which varies depending on desired resolution from lab-based x-ray diffraction equipment with a loading stage to international syncrotron facilities (Morgeneyer, Helfen, Mubarak, & Hild, 2013).

1.8 Digital image correlation

Digital image correlation (DIC) was chosen as the most desirable method for strain measurements in these experiments for SMA characterization for the following reasons. First, DIC is a non-contact method which is designed to measure strains at many (thousands, ten-thousands) points throughout the measured region of the specimen. This method is especially useful as a strain measurement technique for SMAs, because localized deformations are often present which are caused by either induced localized heating of an SMA actuator which causes large localized non-linear deformations due to phase transformation, as well as naturally occurring localized deformations characteristic to SMAs, such as Lüders bands (J. Shaw & Kyriakides, 1997) (Hall, 1951). Furthermore, this method is good for capturing non-homogeneous deformations due to non-uniform surface geometries, which is explored in a later section. Secondly, DIC provides a relatively cost-effective, accurate, and reliable mea-

surement technique which is ideal for the characterization measurements performed in this work.

First developed in the early 1980's, DIC was derived from early attempts at imaging analysis techniques, crediting such imaging measurement techniques as the basic concepts of photogrammetry, and moire. The first publication was from a research group at the University of South Carolina in 1982; the concept of DIC was presented in Peters and Ranson (1982), including the principle of comparing the 'deformed image' to the 'reference image,' the selection of subsets, as well as the idea of using a speckle pattern to provide sufficient contrast on a specimen surface for point tracking. These ideas were further developed the following year by M. Sutton, Wolters, Peters, Ranson, and McNeill (1983) who implemented the approach in preliminary experiments. More information about the development and history of DIC may be found in M. A. Sutton, Orteu, and Schreier (2009).

Two styles of DIC may be performed: 2D-DIC, which measures in-plane deformations, and 3D-DIC, which additionally measures out-of-plane deformations. 3D-DIC is especially useful for cylindrical or other non-planar shaped specimens, but is also useful to demonstrate the out-of-plane deformations occurring due to phenomenon such as out-of-plane transverse strain, or out-of-plane shape change due to SMA phase transformation, for example. In contrast to digital volume correlation, 2D- and 3D- DIC provide strain measurement only on the surface of a specimen. Both 2D-DIC and 3D-DIC have been utilized in this work.

DIC measurement is performed by comparison of two gray-scale digital images: the reference image, or image taken at the beginning of an experiment, and the deformed image, taken during the experiment. Different locations on the testing surface are identified by a random pattern of high contrast on the surface of the specimen which are identified within the digital image by areas of high contrast,

that is, severe differences in the gray values of groups of pixels. Point-to-point mapping is performed by dividing the surface testing surface into a uniform grid of square *subsets*, such that multiple speckles exist in each subset, and each subset contains a certain number of the pixels of the digital image. Sometimes a contrasted pattern exists naturally on the surface of a specimen. However, typically the pattern is applied to the specimen in the form of speckles which result in a random grid of small groups of pixels (black speckles) with gray values at either the high or low extreme of the gray-value spectrum but opposite of the surrounding substrate (white background). A common method for applying the speckles is to paint the entire specimen white, then spray speckles with black paint such that the pixels which are part of speckles have very low gray values and the pixels which are part of the substrate have very high gray values according to the gray value distribution which uniquely defines each subset. The DIC algorithm tracks the differences between the subsets. A good example of a speckle pattern is shown in Figure 1.4.

1.8.1 A review of the DIC optimization algorithm

An extensive review of the DIC algorithm is shown here. Since its original formulation, the work performed by Peters and Ranson (1982) and M. Sutton et al. (1983) has been modified, implemented, and prepared for use in commercially used software (Correlated Solutions, Inc., 2014), and the up-to-date algoritms used for DIC are crystallized in the recent book, M. A. Sutton et al. (2009). The derivations presented in Section 5 of that book are the basic principles of the DIC method, and it is worth while to thoroughly review them here. The method is performed by obtaining two or more gray-scale images: the reference image taken before the test, and the deformed image(s) taken during the test such that the deformed image taken at a time step represents a displacement field in the specimen at that time step. The

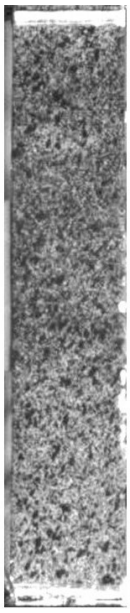

Figure 1.4: An example of a good DIC speckle pattern is shown. The NiTi specimen was painted with a white background and black speckles. A good distribution of similar-sized black speckles was used with a white background.

displacement field is then calculated by tracking the subsets between the reference and deformed image. The subsets in the reference image are identified by the unique spatial distribution of pixels for each subset. A model is formed which is a function of space and time to represent the gray value distribution of the pixels which represent the object being photographed. The gray value of a pixel may be represented as the intensity of that pixel, thus the gray value distribution of the pixels representing the object with respect to space and time at a specific location on the object, x, is the stated as the light-intensity function

$$G = G(x, t). \tag{1.1}$$

At location $x + \Delta x$ on the same object, therefore, the gray value distribution is represented by $G = G(x + \Delta x, t)$. In comparison to the original location, x, the gray

value distribution at the new location may be represented by the first order Taylor series expansion (M. A. Sutton et al., 2009)

$$G(x + \Delta x, t) = G(x, t) + \frac{\partial G}{\partial x}\Delta x. \tag{1.2}$$

In 1-D, $G(x, t)$ at time t may be thought of as a function which can be drawn on the $G - x$ axes. After a change in time, Δt, the function $G(x, t)$ shifts by a constant offset value due to the deformation which occurs in the object at location x over the time step Δt. It is assumed here that the local motion $\dot{u}$ is constant with respect to space and time. After a time interval Δt the change in gray value distribution may be written as (M. A. Sutton et al., 2009)

$$\Delta G = G(x, t + \Delta t) - G(x, t). \tag{1.3}$$

However, we would like to know what is the shift spatially for the point x over time, Δt. Equation (1.3) tracks the global location (from the point of view of an external observer) over time, but we want to track the change in position locally (from the point of view of a local observer on the specimen). Therefore, the original location, x, is "found'' after Δt by subtracting the offset in the distribution function, $G(x, t)$, due to the spatial shift. Thus (M. A. Sutton et al., 2009)

$$\begin{aligned} \Delta G &= G(x, t + \Delta t) - G(x, t) \\ &= G(x - \dot{u}\Delta t, t) - G(x, t) \\ &= G(x - \Delta x, t) - G(x, t). \end{aligned} \tag{1.4}$$

Writing the first order Taylor series expansion gives

$$G(x - \Delta x, t) = G(x, t) - \frac{\partial G}{\partial x}\Delta x, \tag{1.5}$$

thus

$$\Delta G = -\frac{\partial G}{\partial x}\Delta x. \tag{1.6}$$

The spacial evolution of the point may now be written as

$$\Delta x = \dot{u}\Delta t = -\frac{\Delta G}{\frac{\partial G}{\partial x}}, \tag{1.7}$$

where ΔG may be thought of as the difference in gray value distribution between the reference (at time $t = 0$) and deformed images (after time $\Delta t = \frac{\Delta x}{\dot{u}}$). For the limit $\Delta t \to 0$ (M. A. Sutton et al., 2009),

$$\frac{\partial G}{\partial t} + \dot{u}\frac{\partial G}{\partial x} = 0. \tag{1.8}$$

For the scope of this derivation the two-dimensional displacement field is considered, thus expansion to 2-D is written as (M. A. Sutton et al., 2009)

$$\mathbf{x} = \begin{bmatrix} x_1 \\ x_2 \end{bmatrix}, \quad \boldsymbol{\nabla} G = \begin{bmatrix} \frac{\partial G}{\partial x_1} \\ \frac{\partial G}{\partial x_2} \end{bmatrix}, \tag{1.9}$$

and writing $v = \frac{\boldsymbol{\Delta x}}{\Delta t}$, Equation (1.8) rewritten for 2-D is (M. A. Sutton et al., 2009)

$$\frac{\partial G}{\partial t} + \boldsymbol{v} \cdot \boldsymbol{\nabla} G = 0 \tag{1.10}$$

which is the well known *brightness change constraint equation* for optical flow, for which a solution is sought here. For the discrete case, Equation (1.10) is (M. A. Sut-

ton et al., 2009)

$$\frac{\Delta G}{\Delta t} = \boldsymbol{v} \cdot \boldsymbol{\nabla} G, \tag{1.11}$$

thus

$$\boldsymbol{\Delta x} \cdot \boldsymbol{\nabla} G = \Delta G. \tag{1.12}$$

Equation (1.12) represents the difference in gray value distribution between the reference and deformed images, which is expressed as the change in gray value distribution with respect to change in position, multiplied by the change in position.

The pixels which make up the subsets take the form of discretely sized squares which are aligned orthogonally throughout the digital image. Thus we consider that the gradient of the gray value distribution is in the direction perpendicular to the current edge of the pixel, so that Equation (1.12) represents the gradient component of $\boldsymbol{\Delta x}$ that is perpendicular to the current edge, while the other component is zero. Thus Equation (1.12) may be written as (M. A. Sutton et al., 2009)

$$\Delta_{\perp} = -\Delta G / \left| (\nabla G)_{\perp} \right|. \tag{1.13}$$

This equation may be solved for the average local displacements $\Delta\bar{x}$ and $\Delta\bar{y}$ for a neighborhood group of points of interest which make up a subset, assuming that displacements within that neighborhood are approximately constant.

An example is explored at this time using a discrete number of points of interest each of which are surrounded by a discrete number of pixels. Consider Equation (1.12) which represents a point of interest surrounded by a number of pixels. As an example, this point is represented by Figure 1.5, which shows the point at location

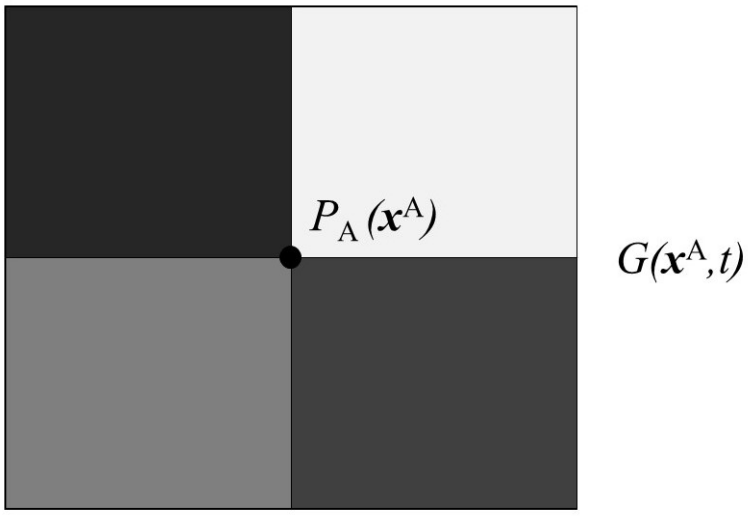

Figure 1.5: A point of interest, P^{A} at location $\mathbf{x}^{\mathrm{A}}$, surrounded by four pixels with gray value distribution $G(\mathbf{x}^{\mathrm{A}}, t)$.

x^{A} surrounded by a number of pixels. The gray value distribution for this point of interest is $G(\mathbf{x}^{\mathrm{A}}, t)$.

For this example, consider four similar points which together form a subset, where each point may be identified by a distinct gray value distribution. This is represented in Figure 1.6.

The points of interest, points $P_1 - P_4$, are each surrounded by four pixels with gray value distributions $G(\mathbf{x}^1, t)$, $G(\mathbf{x}^2, t)$, $G(\mathbf{x}^3, t)$, $G(\mathbf{x}^4, t)$, which for simplicity will be denoted as $G^1 - G^4$. The motion of each point in the subset is distinct, yet are assumed to be approximately equal. Thus, the average displacements, $\Delta\bar{x}$ and $\Delta\bar{y}$, are the displacements of the entire subset. The average displacements may be solved by expansion of Equation (1.13) to 2-D and for the subset of Figure 1.6 is written as (M. A. Sutton et al., 2009)

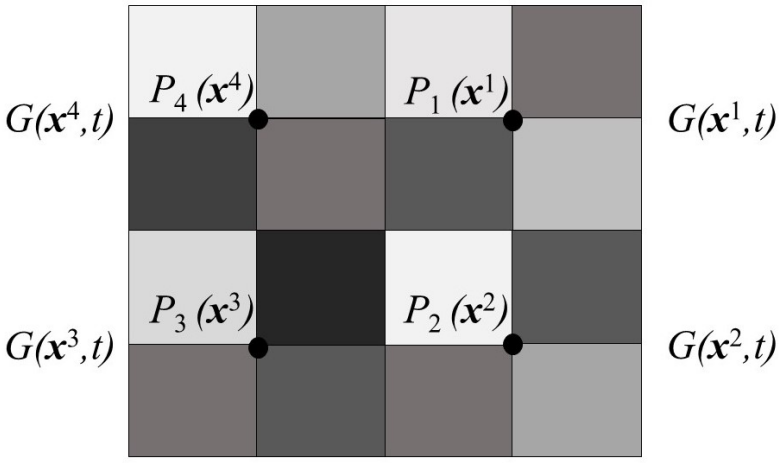

Figure 1.6: Four points with local gray value distributions $G(\mathbf{x}^{1-4}, t)$ which form a subset.

$$\begin{bmatrix} \frac{\partial G^1}{\partial x} & \frac{\partial G^1}{\partial y} \\ \frac{\partial G^2}{\partial x} & \frac{\partial G^1}{\partial y} \\ \frac{\partial G^3}{\partial x} & \frac{\partial G^1}{\partial y} \\ \frac{\partial G^4}{\partial x} & \frac{\partial G^1}{\partial y} \end{bmatrix} \begin{bmatrix} \Delta\bar{x} \\ \Delta\bar{y} \end{bmatrix} = - \begin{bmatrix} \Delta G^1 \\ \Delta G^2 \\ \Delta G^3 \\ \Delta G^4 \end{bmatrix}, \tag{1.14}$$

which may be expressed as (M. A. Sutton et al., 2009)

$$\mathbf{G} \cdot \boldsymbol{\Delta}\bar{\mathbf{x}} = -\mathbf{g}, \tag{1.15}$$

which is an overdetermined system of equations. A solution may be found by multiplying both sides by $\mathbf{G}^T$ as

$$\boldsymbol{\Delta}\bar{\mathbf{x}} = -\left(\mathbf{G}^T\mathbf{G}\right)^{-1}\mathbf{G}^T\mathbf{g}, \tag{1.16}$$

such that the two-dimensional diagonal Hessian matrix may be written as

$$
\begin{aligned}
H &= \begin{bmatrix} \partial_x G^1 & \partial_x G^2 & \partial_x G^3 & \partial_x G^4 \\ \partial_y G^1 & \partial_y G^2 & \partial_y G^3 & \partial_y G^4 \end{bmatrix} \cdot \begin{bmatrix} \partial_x G^1 & \partial_y G^1 \\ \partial_x G^2 & \partial_y G^2 \\ \partial_x G^3 & \partial_y G^3 \\ \partial_x G^4 & \partial_y G^4 \end{bmatrix} = \\
&= \begin{bmatrix} \left(\partial_x G^1\right)^2 + \left(\partial_x G^2\right)^2 + \left(\partial_x G^3\right)^2 + \left(\partial_x G^4\right)^2 & \partial_x G^1 \partial_y G^1 + \partial_x G^2 \partial_y G^2 + \partial_x G^3 \partial_y G^3 + \partial_x G^4 \partial_y G^4 \\ \partial_x G^1 \partial_y G^1 + \partial_x G^2 \partial_y G^2 + \partial_x G^3 \partial_y G^3 + \partial_x G^4 \partial_y G^4 & \left(\partial_y G^1\right)^2 + \left(\partial_y G^2\right)^2 + \left(\partial_y G^3\right)^2 + \left(\partial_y G^4\right)^2 \end{bmatrix} = \\
&= \begin{bmatrix} \sum_{i=1}^{4} \left(\partial_x G^i\right)^2 & \sum \partial_x G \partial_y G \\ \sum \partial_x G \partial_y G & \sum \left(\partial_y G\right)^2 \end{bmatrix},
\end{aligned}
\tag{1.17}
$$

and the vector $\mathbf{b}$ is written as

$$
\mathbf{b} = \mathbf{G}^T \mathbf{g} = \begin{bmatrix} \partial_x G^1 & \partial_x G^2 & \partial_x G^3 & \partial_x G^4 \\ \partial_y G^1 & \partial_y G^2 & \partial_y G^3 & \partial_y G^4 \end{bmatrix} \begin{bmatrix} \Delta g^1 \\ \Delta g^2 \\ \Delta g^3 \\ \Delta g^4 \end{bmatrix} = \begin{bmatrix} \sum \partial_x G \Delta g \\ \sum \partial_y G \Delta g \end{bmatrix}, \tag{1.18}
$$

where $\partial_x G$ represents the partial derivative $\frac{\partial G}{\partial x}$. Equation (1.16) now becomes (M. A. Sutton et al., 2009)

$$
\begin{bmatrix} \Delta \bar{x} \\ \Delta \bar{y} \end{bmatrix} = \begin{bmatrix} \sum_{i=1}^{4} \left(\partial_x G^i\right)^2 & \sum \partial_x G \partial_y G \\ \sum \partial_x G \partial_y G & \sum \left(\partial_y G\right)^2 \end{bmatrix}^{-1} \begin{bmatrix} \sum \partial_x G \Delta g \\ \sum \partial_y G \Delta g \end{bmatrix}. \tag{1.19}
$$

As long as $(\mathbf{G^T G})$ is not singular, the motion $\mathbf{\Delta \bar{x}}$ may be estimated. It should be noted that $(\mathbf{G}^T\mathbf{G})$ takes a singular form in regions of constant gray value, or in areas where the intensity gradients are aligned in a single direction, i.e., when $\frac{\partial G^N}{\partial x} = 0$ or

$\frac{\partial G^N}{\partial y} = 0$. In such regions, motions cannot be detected by this algorithm.

So far, we have demonstrated how we can solve for the motion of subset by tracking the gray value distribution at different points within the subset. This solution should now be presented as an optimization problem to identify the gray value distribution between the reference image and the deformed image. In general, the gray value distribution is time dependent. However, it has been shown how this time dependence may be alternatively represented by assuming constant velocity motions during the time interval between each captured image. Therefore, the gray value distributions are written as being only spatially dependent. An optimization of the spatial displacement of a subset may be found by locating the same subset in the deformed image as the reference image, which by definition is found by finding the minimum value of $\Delta G = G^{def} - G^{ref}$. In the equations that follow, the reference gray value distribution is denoted as $F(\mathbf{x})$ and the deformed image distribution is $G(\mathbf{x} + \bar{\mathbf{d}})$. For the example problem of Figure 1.6, the optimum solution to the displacement of a point between the reference and deformed images may be expressed as (M. A. Sutton et al., 2009)

$$\begin{aligned} \bar{\mathbf{d}}_{opt} &= \text{argmin} \sum_{\boldsymbol{i=1}}^{\mathbf{4}} \left| G^i(\mathbf{x} + \bar{\mathbf{d}}) - F^i(\mathbf{x}) \right|^2, \\ &= \text{argmin} \left[\left(G^1 - F^1 \right)^2 + \left(G^2 - F^2 \right)^2 + \left(G^3 - F^3 \right)^2 + \left(G^4 - F^4 \right)^2 \right] \end{aligned} \tag{1.20}$$

which is known as the *sum of squares deviation* (SSD) algorithm, giving the average displacement d_{opt} over the four points in the subset. The summation is written out in Equation (1.20) to demonstrate the form adopted by the summation, but from now on will be represented by the summation operator alone. Taking the partial derivatives of G^N with respect to x and y in the sense of a first order Taylor series

expansion, an iterative optimization algorithm may be written in the form of a cost function as (M. A. Sutton et al., 2009)

$$\chi^2\left(\bar{d}_x+\Delta_x,\bar{d}_y+\Delta_y\right)=\sum_{\boldsymbol{i=1}}^{\mathbf{4}}\left|G^i(\mathbf{x}+\bar{\mathbf{d}})-\frac{\partial G^i}{\partial x}\Delta_x-\frac{\partial G^i}{\partial y}\Delta_y-F^i(\mathbf{x})\right|^2. \tag{1.21}$$

Taking the partial derivatives with respect to Δ_x and Δ_y and setting to zero gives

$$\begin{aligned}\sum_{\boldsymbol{i=1}}^{\mathbf{4}}\partial_x G^i(F^i-G^i)&=\sum\left|-(\partial_x G)^2\Delta_x-\partial_x G\partial_y G\Delta_y\right|\\ \sum\partial_y G(F-G)&=\sum\left|-\partial_x G\partial_y G\Delta_x-(\partial_y G)^2\Delta_y\right|.\end{aligned} \tag{1.22}$$

Thus (M. A. Sutton et al., 2009),

$$\begin{bmatrix}\Delta_x\\ \Delta_y\end{bmatrix}=\begin{bmatrix}\sum_{\boldsymbol{i=1}}^{\mathbf{4}}\left(\partial_x G^i\right)^2 & \sum\partial_x G\partial_y G\\ \sum\partial_x G\partial_y G & \sum\left(\partial_y G\right)^2\end{bmatrix}^{-1}\begin{bmatrix}\sum\partial_x G\left(F-G\right)\\ \sum\partial_y G\left(F-G\right)\end{bmatrix}, \tag{1.23}$$

which may be solved iteratively until convergence of $\bar{d}_{opt}$ is reached, which is updated as

$$\bar{d}^{k+1}_{opt_{x,y}}=\bar{d}^{k}_{opt_{x,y}}+\Delta_{x,y}. \tag{1.24}$$

This technique is known as the Lucas-Kanade tracker algorithm (Lucas, Kanade, et al., 1981).

Up to this point, calculations for the displacements of the subset in a deformed image have been performed. However, this algorithm must be expanded to account for relational deformations within each subset (such as elongation, rotation, and shear). For infinitesimal deformation, the infinitesimal strain tensor may be written with respect to displacements, u_i, as

$$\varepsilon_{ij} = \frac{1}{2}\left(\partial_{x_j} u_i - \partial_{x_i} u_j\right). \tag{1.25}$$

Distortions within the subset may be represented by coupling terms between $\bar{d}_x$ and $\bar{d}_y$ in Equation (1.20). We may write a shape function $\xi(\mathbf{x}, \mathbf{p})$ such that (M. A. Sutton et al., 2009)

$$\chi^2(\mathbf{p}) = \sum_{\boldsymbol{i=1}}^{\mathbf{4}} \left(G^i\left(\xi\left(\mathbf{x}, \mathbf{p}\right)\right) - F^i(\mathbf{x})\right)^2. \tag{1.26}$$

For pure translation, the shape function is written as (M. A. Sutton et al., 2009)

$$\xi\left(\mathbf{x}, \mathbf{p}\right) = \begin{bmatrix} x_1 \\ x_2 \end{bmatrix} + \begin{bmatrix} p_0 \\ p_1 \end{bmatrix} \tag{1.27}$$

for which Equation (1.20) is recovered, and the terms p_0 and p_1 are used to iteratively update the values of $\bar{d}_x$ and $\bar{d}_y$. Distortions are represented when the shape function for affine transformation is written as

$$\xi\left(\mathbf{x}, \mathbf{p}\right) = \begin{bmatrix} p_0 \\ p_1 \end{bmatrix} + \begin{bmatrix} 1 + p_2 & p_3 \\ p_4 & 1 + p_5 \end{bmatrix} \cdot \begin{bmatrix} x_1 \\ x_2 \end{bmatrix}. \tag{1.28}$$

An iterative algorithm is found by plugging in the shape function of Equation (1.28) to Equation (1.26), taking the partial derivatives with respect to p_n ($n = 0, 1, 2, 3, 4, 5$), and setting them to zero. Thus, we have

$$\boldsymbol{\Delta p} = \mathbf{H}^{-1}\mathbf{q} \tag{1.29}$$

where $\boldsymbol{\Delta p}$ represents the updates to p_n in the iterative solver. The Hessian matrix may be calculated to be (M. A. Sutton et al., 2009)

$$\mathbf{H} = \begin{bmatrix} \sum_{i=1}^{4} (G_x^i)^2 & \sum G_x G_y & \sum G_x^2 x & \sum G_x^2 y & \sum G_x G_y x & \sum G_x G_y y \\ \sum G_x G_y & \sum G_y^2 & \sum G_x G_y x & \sum G_x G_y y & \sum G_y^2 x & \sum G_y^2 y \\ \sum G_x^2 x & \sum G_x G_y x & \sum G_x^2 x^2 & \sum G_x^2 xy & \sum G_x G_y x^2 & \sum G_x G_y xy \\ \sum G_x^2 y & \sum G_x G_y y & \sum G_x^2 xy & \sum G_x^2 y^2 & \sum G_x G_y xy & \sum G_x G_y y^2 \\ \sum G_x G_y x & \sum G_y^2 x & \sum G_x G_y x^2 & \sum G_x G_y xy & \sum G_y^2 x^2 & \sum G_y^2 xy \\ \sum G_x G_y y & \sum G_y^2 y & \sum G_x G_y xy & \sum G_x G_y y^2 & \sum G_y^2 xy & \sum G_y^2 y^2 \end{bmatrix},$$

and

$$\mathbf{q} = \begin{bmatrix} \sum_{i=1}^{4} G_x^i (F^i - G^i) \\ \sum G_y (F - G) \\ \sum G_x x (F - G) \\ \sum G_x y (F - G) \\ \sum G_y x (F - G) \\ \sum G_y y (F - G) \end{bmatrix},$$

where G_x represents the partial derivative of G with respect to x in this notation. The possibility of a solution to Equation (1.29) depends on whether or not the Hessian matrix can be inverted.

A key consideration in the solution of Equation (1.26) is that it depends on the absolute gray value of each pixel, and the solution is achieved by minimizing the difference in the actual gray values of pixels for a particular subset between two images. However, this solution is valid only if lighting is absolutely constant, which is not possible in most experiments. Even due to very small deformations in the specimen or environmental perturbations each image taken during an experiment

will have a slightly different lighting distribution. Therefore it is necessary to provide an algorithm which takes account of the *relative* gray value distribution in a subset instead of the actual gray values. Though the lighting in a subset may change, the relative gray value distribution will be the same, and optimization is not affected by lighting changes. An attractive option is to replace the SSD algorithm (Equation (1.26) with the normalized cross-correlation criterion (M. A. Sutton et al., 2009)

$$\chi^2_{NCC} = \frac{\sum FG}{\sqrt{\sum F^2 \sum G^2}}, \tag{1.30}$$

which provides an ideal optimization criterion for determining the gray value distribution as it is independent of scale. However, this method is inefficient with its complex derivatives. Instead, the SSD algorithm can be modified to account for changes in offset and scale in lighting by creating a photometric transformation of the gray value distribution, $\Phi(G)$. Substituting to Equation (1.26) (M. A. Sutton et al., 2009),

$$\chi^2 = \sum \left|\Phi(G) - F\right|^2, \tag{1.31}$$

and different forms of $\Phi(G)$ may be implemented to forgo offset or scale in lighting.

Different variations of the photometric transformation have been explored by M. A. Sutton et al. (2009), and are reviewed here. For displacement of lighting by an offset, the transformation becomes (M. A. Sutton et al., 2009)

$$\Phi(G) = G + b, \tag{1.32}$$

and the the cost function may be written as (M. A. Sutton et al., 2009)

$$\chi^2 = \sum \left(G + b - F\right)^2, \tag{1.33}$$

where the offset parameter b may be solved either as an additional parameter of the optimization, or by developing an implicit minimization of Equation (1.33) for the value b, as (M. A. Sutton et al., 2009)

$$b_{opt} = \text{argmin}_b \sum \left(G + b - F\right)^2. \tag{1.34}$$

The optimization of this squared sum difference for the value of b is found by taking the partial derivative of χ^2 with respect to b as (M. A. Sutton et al., 2009)

$$\begin{aligned}
\frac{\partial \chi^2}{\partial b} &= 2 \sum \left(G + b - F\right), \\
\frac{\partial \chi^2}{\partial b} &= 0, \text{ thus,} \\
b_{opt} &= \bar{F} - \bar{G}, \\
\bar{F} &= \frac{\sum F}{n}, \\
\bar{G} &= \frac{\sum G}{n},
\end{aligned} \tag{1.35}$$

where n is the number of points of interest in the subset. The optimum value of b, b_{opt} can be substituted into Equation (1.33) to give the zero-mean sum of square difference criterion (M. A. Sutton et al., 2009)

$$\chi^2_{ZSSD} = \sum \left(\left(G - \bar{G}\right) - \left(F - \bar{F}\right)\right)^2. \tag{1.36}$$

Similarly, for change in lighting by a factor of scale, the photometric transformation of G is written as (M. A. Sutton et al., 2009)

$$\Phi(G) = aG, \tag{1.37}$$

such that the cost function becomes (M. A. Sutton et al., 2009)

$$\chi^2 = \sum \left(aG - F\right)^2. \tag{1.38}$$

In a similar manner as was done for the optimized offset parameter (b_{opt}), the optimized scale factor a_{opt} may be calculated by the optimization algorithm (M. A. Sutton et al., 2009)

$$a_{opt} = \text{argmin}_a \sum \left(aG - F\right)^2. \tag{1.39}$$

such that a_{opt} is calculated to be

$$a_{opt} = \frac{\sum FG}{\sum G^2}, \tag{1.40}$$

and Equation (1.38) becomes the so called normalized sum of squared difference equation

$$\chi^2_{NSSD} = \sum \left(\frac{\sum FG}{\sum G^2} G - F\right)^2. \tag{1.41}$$

The photometric transformations for offset and scale have been introduced. Now Equations (1.32) and (1.37) may be combined to give the combined photometric transformation of the gray value distribution for offset and scale (M. A. Sutton et al., 2009),

$$\Phi\left(G\right) = aG + b. \tag{1.42}$$

The sum of squared difference optimization algorithm is now (M. A. Sutton et al., 2009)

$$\chi^2 = \sum \left(aG + b - F\right)^2, \tag{1.43}$$

and the optimized parameters b_{opt} and a_{opt} are written as (M. A. Sutton et al., 2009)

$$\begin{aligned} a_{opt} &= \frac{\sum \left(F - b\right) G}{\sum G^2}, \\ b_{opt} &= \frac{\sum F - aG}{n}, \end{aligned} \tag{1.44}$$

and the so-called zero-mean normalized sum of squared difference equation is (M. A. Sutton et al., 2009)

$$\chi^2_{ZNSSD} = \sum \left(\left(\frac{\sum \bar{F}\bar{G}}{\sum \bar{G}^2} G - \bar{G} \frac{\sum \bar{F}\bar{G}}{\sum \bar{G}^2} \right) - F + \bar{F} \right)^2, \tag{1.45}$$

where all F, $\bar{F}$, G, and $\bar{G}$ are functions of $\xi(\mathbf{x}, \mathbf{p})$. Equation (1.45) may be used to solve for the parameters $\mathbf{p}$ such that relative gray value distributions are utilized instead of the absolute gray values.

1.8.2 Factors affecting DIC measurement accuracy

The DIC deformation measurement technique has many variables which may affect the accuracy and precision of the measurements, and an attempt is made here to review these measurement error sources. In Reedlunn et al. (2011) the authors provide an outline of the factors which may affect the accuracy of DIC measurements, which are reviewed here.

1. *Specimen surface preparation.* In order to make measurements by DIC, the surface of the specimen must demonstrate a random and highly contrasted optical pattern. For best accuracy, the appropriate size of the variations in

the pattern depends on the resolution of the chosen camera; a speckle on a given specimen should contain 3-7 pixels (M. A. Sutton et al., 2009), and the speckles should have a spacing of 5-10 pixels. Also, reflection on the specimen surface negatively affects correlation accuracy because small changes in lighting will greatly affect the gray value distributions in the subsets such that the distributions will not necessarily be retained within offset and scale of lighting. Therefore, a matte-colored surface is best so that the only consequences of changes in lighting are offset and scale of the gray value distributions.

2. *Camera, lens, and environment.* Good digital photography practices should be followed for performing DIC, taking into consideration the field of view (FOV), depth of field (DOF), focus, aperature, and illumination. Also, the camera should face the specimen directly (2D- and 3D-DIC), and be perpendicular to the specimen for a single camera (2D-DIC) or two cameras both at 15° to the specimen and pointing at the same location on the specimen (3D-DIC) (Reedlunn et al., 2011) to minimize distortions in the collected images. This criterion is especially critical for 2D-DIC. Furthermore, it is not advised to use mirrors because of the possibility of optical aberrations and introduction of new lighting to the camera sensor which are not from the specimen surface. (Reedlunn et al., 2011)

3. *Gray-scale range.* In general an increase in the number of discrete gray levels decreases the minimum value of the cost function in searching for the optimum gray value distribution, thus increasing the accuracy of the measurement. Color images are not advised because a simplistic gray-value based algorithm is no longer possible with the introduction of color. Furthermore, color CCD cameras should be avoided because the construction of the device affords a

non-monotonic intensity scale (Reedlunn et al., 2011).

4. *Number of images captured.* Sufficient data should be gathered to appropriately capture the motion of the specimen. Actually, DIC measurement does not depend on the frequency of images taken, as each image is compared to the original reference image individually. That being said, capturing more images will provide more data regarding the history of deformation, making post-analysis more accurate. The image capture rate should be chosen based on the duration of the experiment, the speed at which key phenomena will occur during the experiment, the amount of storage space available, and the size of the images.

5. *Choice of interpolation function and subset size.* The possible interpolation functions for the DIC calculation were shown previously; while the normalized cross-correlation criterion provides a more accurate optimization, the squared sum differences algorithm is less costly computationally. Furthermore, the squared sum differences algorithm for example is based on a taylor series expansion of the gray value distribution. The first order taylor series was used in the previous review. A higher order function may be used to increase accuracy of the correlation. The subset size should be chosen according to the resolution as well as the distribution of the speckles. As mentioned before the speckles should contain 3-7 pixels. The subset should be chosen such that each subset contains 3-5 speckles.

6. *Out-of-plane displacements for 2D-DIC.* 2D-DIC may provide less accurate results if there are significant out-of-plane displacements. Although out-of-plane displacements cannot be completely avoided, the effects may be minimized by either placing the camera further from the specimen, using a telecentric

lens, or performing a prediction or separate measurement of the out-of-plane displacements (Reedlunn et al., 2011).

1.9 Full-field temperature measurement methods

The method chosen for full-field temperature measurement was IR thermography which will be reviewed here. Infra-red (IR) thermography is identified as an ideal metrology for the thermal assessment of coupled thermomechanical response of SMAs. The method measures the intensity of radiative heat transfer from the surface of a target (Minkina & Dudzik, 2009) which may be converted to temperature measurement through careful calibration. Objects emit varying amounts of radiation with respect to the object's physical temperature depending on certain material properties; the key experimental parameter is the emissivity (ϵ) of the object, which is defined as the ratio between a material's radiant exitance and the radiant exitance of a black body (Minkina & Dudzik, 2009). The emissivity ranges from $\epsilon = 0$ or low radiation for very shiny objects, to $\epsilon = 1$, or high radiation for nearly-black bodies. IR thermography provides a technique for measuring the temperature on the same surface of an object that is simultaneously being tracked via DIC. This method is ideal for the experiments designed for characterization of actuator SMA materials, in which the temperature fields are intended to be varied in two dimensions only.

1.10 Modeling and model calibration

Effective utilization of SMA materials requires some degree of optimization of the material performance which is best understood via accurate predictive analysis of the simulation model. Furthermore, an effort has been made in this work to perform an estimation of the full mechanical response of a specimen through utilization of an SMA model using the full-field deformation and temperature measurements. A review of SMA modeling efforts in general, as well as a detailed derivation of the

SMA constitutive model used in this work are shown in this section.

Extensive research has been performed regarding the formulation of such methods for shape memory alloys. Existing constitutive models may be classified in two groups: micromechanics-based models and phenomenological models (D. C. Lagoudas et al., 2006). The micromechanics based models use information about the crystal stucture in the material to predict the macromechanical response. The macro-scale response of the SMA material may be predicted by knowledge of the granular structure for (generally) polycrystalline SMAs by using the knowledge of single crystal SMAs and then applying homogenization techniques to approximate polycrystalline SMAs. Given the underlying differences between single crystal and polycrystalline SMA materials, the most visible of which is the anisotropy of single-crystal SMAs versus the more isotropic response of randomly distributed grains in annealed polycrystalline SMA materials, the process of predicting macroscopic SMA behavior requires computationally expensive methods as described by D. C. Lagoudas et al. (2006). Efforts toward the development of micromechanical models include the works of Patoor, Eberhardt, and Berveiller (1996), Gao and Brinson (2002), among others. On the other hand, phenomenological SMA models are formulated from a continuum mechanics standpoint, utilizing thermodynamic potential functions to formulate the expected macroscopic thermomechanical response in polycrystalline SMA systems. This type of model uses internal and state variables within a set of evolution equations to describe the evolution of the solid-to-solid phase transformation in the material. This is based on a set of macroscopic parameters identified by extensive experimental observations, rather than micromechanical material properties re-arranged to approximate the response of a polycrystalline material, as is the case for micromechanics-based models. The most referenced phenomenological models include D. C. Lagoudas et al. (2006), Helm and Haupt (2003), Boyd and Lagoudas

(1996), Brinson, Bekker, and Hwang (1996), and Auricchio, Taylor, and Lubliner (1997), among others. Consideration of micromechanical models is beyond the scope of this work; rather, this work is motivated by phenomenological models such as that of D. Lagoudas et al. (2012), as we aim to demonstrate the integrity of a comprehensive experimental approach for characterization of SMAs and identification of parameters to be used in phenomenological modeling.

In order to utilize any SMA constitutive model, calibration of the identifying parameters used in that model must be performed. No SMA material is the same as the next; to use an SMA material in a design requires careful calibration of the constitutive model to that specific material. Therefore, the need for reliable experimental methods for the identification of SMA material parameters for constitutive model calibration is emphasized in this work. Previous efforts for material characterization will be described; but phenomenological SMA constitutive model calibration requires the understanding of very particular material response features via the execution of well-chosen experiments. In fact, an increasingly complex menu of material modeling options requires a greater number of experiments, where the type of SMA application in consideration also guides the experimentation to be performed (e.g., isothermal experiments for pseudoelastic SMAs, isobaric experiments for actuator applications). However, in this work the goal is to reduce the number of isobaric experiments necessary to identify the parameters associated with arbitrarily complicated SMA constitutive models, while simultaneously maximizing understanding regarding the performance of future SMA actuator systems.

1.11 Review of an SMA constitutive model

The SMA constitutive model has been proposed which is derived from thermodynamic first principles in D. Lagoudas et al. (2012), and is reviewed here. A Gibbs

free energy relation has been formulated which is dependent on the stress ($\boldsymbol{\sigma}$) and temperature (T) state variables, as well as a set of internal state variables which include the *transformation strain* ($\boldsymbol{\varepsilon^t}$), the *total martensitic volume fraction* (ξ), and a *transformation hardening energy* term (g^t) which defines the non-linear change in mixing energy during phase transformation. By relating the Gibbs free energy, $G = G(\boldsymbol{\sigma}, T, \boldsymbol{\varepsilon^t}, \xi, g^t)$, to the internal energy through the *Legandre transformations*, the Clausius-Planck inequality form of the second law may be written in terms of the rate of change of Gibbs free energy, as (D. Lagoudas et al., 2012)

$$-\rho\dot{G} - \dot{\boldsymbol{\sigma}} : \boldsymbol{\varepsilon} - \rho s\dot{T} \geq 0, \tag{1.46}$$

where $\boldsymbol{\varepsilon}$ is the total infinitesimal strain and ρ, s, and T are the density, entropy, and temperature state variables, respectively. By the chain rule,

$$-\rho\left(\frac{\partial G}{\partial \boldsymbol{\sigma}} : \dot{\boldsymbol{\sigma}} + \frac{\partial G}{\partial T}\dot{T} + \frac{\partial G}{\partial \boldsymbol{\varepsilon^t}} : \dot{\boldsymbol{\varepsilon}}^{\boldsymbol{t}} + \frac{\partial G}{\partial \xi}\dot{\xi} + \frac{\partial G}{\partial g^t}\dot{g}^t\right) - \dot{\boldsymbol{\sigma}} : \boldsymbol{\varepsilon} - \rho s\dot{T} \geq 0. \tag{1.47}$$

The total infinitesimal strain may be decomposed according to three distinct phenomena: the linear-elastic strain, thermal stain, and also the non-linear recoverable strain due to phase transformation. Therefore,

$$\boldsymbol{\varepsilon} = \boldsymbol{\varepsilon^{el}} + \boldsymbol{\varepsilon^{th}} + \boldsymbol{\varepsilon^t}. \tag{1.48}$$

Using the procedure of Coleman and Noll (1963), the total strain and entropy state variables may be written as (D. Lagoudas et al., 2012)

$$\boldsymbol{\varepsilon} = -\rho\frac{\partial G}{\partial \boldsymbol{\sigma}} = \mathbf{S}\boldsymbol{\sigma} + \boldsymbol{\alpha}\left(T - T_0\right) + \boldsymbol{\varepsilon^t}, \tag{1.49}$$

$$s = -\rho\frac{\partial G}{\partial T} = \frac{1}{\rho}\boldsymbol{\alpha} : \boldsymbol{\sigma} + c\ln\left(\frac{T}{T_0}\right) + s_0, \tag{1.50}$$

and the remaining three partial derivatives of Gibbs free energy with respect to the three internal state variables are the *generalized thermodynamic forces* (Qidwai & Lagoudas, 2000),

$$-\rho\frac{\partial G}{\partial \xi} = p, \quad -\rho\frac{\partial G}{\partial \boldsymbol{\varepsilon^t}} = \boldsymbol{\sigma}, \quad -\rho\frac{\partial G}{\partial g^t} = -1. \tag{1.51}$$

Thus, the second law becomes

$$p\dot{\xi} + \boldsymbol{\sigma} : \dot{\boldsymbol{\varepsilon}}^{\boldsymbol{t}} - \dot{g}^t \geq 0. \tag{1.52}$$

The generalized thermodynamic force p (D. Lagoudas et al., 2012)

$$p = \frac{1}{2}\boldsymbol{\sigma} : \boldsymbol{\Delta S}\boldsymbol{\sigma} + \boldsymbol{\sigma} : \boldsymbol{\Delta\alpha}\,(T - T_0) - \rho\Delta c\left[(T - T_0) - T\ln\left(\frac{T}{T_0}\right)\right] + \rho\Delta s_0 T - \rho\Delta u_0, \tag{1.53}$$

where $\boldsymbol{\Delta S}$, $\boldsymbol{\Delta\alpha}$, Δc, Δs_0, and Δu_0 are the difference in material constants between the austenite and martensite phases. It is assumed that the evolution of the internal state variables is linked to the change in ξ, therefore the transformation strain internal state variable is written as (D. Lagoudas et al., 2012)

$$\dot{\boldsymbol{\varepsilon}}^{\boldsymbol{t}} = \boldsymbol{\Lambda}^{\boldsymbol{t}}\dot{\xi}, \quad \boldsymbol{\Lambda}^{\boldsymbol{t}} = \begin{cases} \boldsymbol{\Lambda}^{\boldsymbol{t}}_{\boldsymbol{fwd}}, & \dot{\xi} > 0, \\ \boldsymbol{\Lambda}^{\boldsymbol{t}}_{\boldsymbol{rev}}, & \dot{\xi} < 0, \end{cases} \tag{1.54}$$

where the transformation direction tensor ($\boldsymbol{\Lambda}^{\boldsymbol{t}}$) for forward and reverse transformation are defined as (D. Lagoudas et al., 2012)

$$\boldsymbol{\Lambda}^{\boldsymbol{t}}_{\boldsymbol{fwd}} = \frac{3}{2} H^{cur}\left(\bar{\sigma}\right) \frac{\boldsymbol{\sigma'}}{\bar{\sigma}}, \quad \boldsymbol{\Lambda}^{\boldsymbol{t}}_{\boldsymbol{rev}} = \frac{\boldsymbol{\varepsilon}^{\boldsymbol{t-r}}}{\xi^{r}}, \tag{1.55}$$

where $H^{cur}(\bar{\sigma})$ is the maximum achievable transformation strain at a given effective stress level, ε^{t-r} and ξ^{r} are the strain and total martensitic volume fraction at the beginning of reverse transformation, and $\boldsymbol{\sigma'}$ is the deviatoric part of the stress tensor. The hardening energy term is written as (D. Lagoudas et al., 2012)

$$\dot{g^{t}} = f^{t}\dot{\xi}, \quad f^{t} = \begin{cases} f^{t}_{fwd}, & \dot{\xi} > 0, \\ f^{t}_{rev}, & \dot{\xi} < 0, \end{cases} \tag{1.56}$$

where f^{t} is known as the *hardening function*, which is proposed as (D. Lagoudas et al., 2012)

$$\begin{aligned} f^{t}_{fwd} &= \frac{1}{2} a_1 \left(1 + \xi^{n_1} - (1-\xi)^{n_2}\right) + a_3, \\ f^{t}_{rev} &= \frac{1}{2} a_2 \left(1 + \xi^{n_3} - (1-\xi)^{n_4}\right) + a_3, \end{aligned} \tag{1.57}$$

where n_1, n_2, n_3, and n_4 are smoothing parameters for the transformation behavior where $0 < n \leq 1$, and a value of $n \neq 1$ results in a smooth transition in the prediction of the transition from inelastic phase transformation behavior to linear-elastic deformation. For this work, unity has been assigned to the smoothing parameters. a_1, a_2, a_3, as well as $\rho\Delta u_0$ are model parameters denoted as (D. Lagoudas et al., 2012)

$$\begin{aligned} &a_1 = \rho\Delta s_0 \left(M_f - M_s\right), \quad a_2 = \rho\Delta s_0 \left(A_s - A_f\right), \\ &a_3 = -\frac{a_1}{4}\left(1 + \frac{1}{n_1+1} - \frac{1}{n_2+1}\right) + \frac{a_2}{4}\left(1 + \frac{1}{n_3+1} - \frac{1}{n_4+1}\right), \\ &\rho\Delta u_0 = \frac{\rho\Delta s_0}{2}\left(M_s + A_f\right). \end{aligned} \tag{1.58}$$

The second law may now be written as

$$\left[\boldsymbol{\sigma} : \boldsymbol{\Lambda^t} + p - f^t\right] \dot{\xi} = \pi^t \dot{\xi} \geq 0, \tag{1.59}$$

where π^t denotes the total thermodynamic driving force. When $\dot{\xi} = 0$, Equation 1.59 is identically satisfied and a strictly dissipative inequality may be imposed (Anand & Gurtin, 2003) such that for $\dot{\xi} \neq 0$,

$$\left[\boldsymbol{\sigma} : \boldsymbol{\Lambda^t} + p - f^t\right] \dot{\xi} = \pi^t \dot{\xi} > 0. \tag{1.60}$$

In order for Equation 1.60 to be satisfied, π^t is positive during forward transformation ($\dot{\xi} > 0$) and negative during reverse transformation ($\dot{\xi} < 0$). A critical thermodynamic driving force, Y^t, is defined for initiating and sustaining transformation such that when π^t is equal to and does not exceed Y^t then transformation is occurring (D. Lagoudas et al., 2012). This relationship is demonstrated by defining the transformation function, Φ^t, as follows:

$$\begin{aligned} \Phi^t_{fwd} &= \pi^t_{fwd} - Y^t_{fwd}, \\ \Phi^t_{rev} &= -\pi^t_{rev} - Y^t_{rev}, \end{aligned} \tag{1.61}$$

which must obey the Kuhn-Tucker conditions for forward and reverse transformation, written as (D. Lagoudas et al., 2012)

$$\Phi^t \leq 0, \quad \Phi^t \dot{\xi} = 0. \tag{1.62}$$

During transformation, $\dot{\xi} \neq 0$, therefore $\Phi^t = 0$ is the thermodynamic constraint during transformation. The stress dependent critical thermodynamic driving force is written as

$$Y^t = Y_0^t + D\boldsymbol{\sigma} : \boldsymbol{\Lambda^t}, \quad Y_0^t = \frac{\rho \Delta s_0}{2} \left(M_s - A_f\right) - a_3, \tag{1.63}$$

where D is the stress-dependent term.

2. EXPERIMENTATION PART I: CHARACTERIZATION OF MACROSCOPIC ACTUATOR SHAPE MEMORY ALLOYS VIA NON-UNIFORM LOCALIZED HEATING

2.1 Introduction

The experimental method explored in this section demonstates a method for characterization of SMA materials used for actuators. SMA actuators have applications in a wide variety of fields, especially the automotive, aerospace, robotic, and biomedical fields (Jani et al., 2014). They demonstrate high energy, high strain, and low shock actuation while being very simplistic in design (Van Humbeeck, 1999). For example, SMA actuators in wire configurations are very common, and are used in both a straight wire configuration, which may perform actuating work via axial strains up to 6% even under loads exceeding 700 MPa, as well as in a helical spring configuration which may generate and recover actuation extensions of much more than 100%. Additionally, many SMA actuating systems employ more geometrically complex 2D and 3D configurations such as the variable geometry chevron (D. Hartl et al., 2010) (D. J. Hartl et al., 2010) (Oehler et al., 2012), the SMA medical heart stent (Morgan, 2004), and the reconfigurable rotor blade (Bushnell et al., 2008), among others.

Some recent reviews exist concerning SMA actuator devices. D. J. Hartl and Lagoudas (2007) as well as Calkins and Mabe (2010) present reviews of recent applications of SMA actuators in the aerospace community. Jani et al. (2014) includes a highly inclusive review of possible and existing applications of SMAs across disciplines, addresses recent developments in SMA research, and provides an overview of the existing types of SMAs. Van Humbeeck (1999) also presented a detailed overview

of past applications of SMA actuators, organizing them into various categories including fashion, fasteners, micro-actuators, hybrid composites (adaptive materials), and damping mechanisms. SMA actuators may also be divided into two subgroups, as outlined by Otsuka and Wayman (1999), ch. 11: *i)* the SMA acts as both sensor and actuator, where the environment acts as a stimulus, as in safety control devices (Van Humbeeck, 1999); *ii)* the SMA is actively heated via a controlled power input to perform an actuation sequence.

2.1.1 Physical mechanisms for SMA actuation

For actuation of SMA devices, cooling the material stress-free from the high temperature austenite phase (highly ordered cubic microstructure) results in a phase transformation to the low temperature martensite phase (tetragonal or monoclinic microstructure) in an energetically favorable twinned configuration (Otsuka & Wayman, 1999) (Patoor et al., 2006) (D. C. Lagoudas et al., 2006). When a critical level of stress is applied to the cooled material, the martensite variants become reoriented causing severe non-linear displacements which are recovered upon reheating. These phenomena are modeled by four descriptive phase transformation boundaries, as follows: when the material is cooled at zero stress from austenite to below the martensite start temperature (M_s), the material begins forward transformation from austenite to martensite. When the temperature is below martensite finish (M_f), the material is fully-martensite. As this phase transformation occurs, the martensitic volume fraction (ξ) changes from zero as austinite to unity as martensite. When the material is reheated under zero load and reaches the austenite start (A_s) temperature, reverse transformation begins. The material returns to the parent austenite phase ($\xi = 0$) when the temperature is above austenite finish (A_f). Identification of these four parameters (as well as others) for the material at various isobaric loads

shows the primary goal in SMA actuator material characterization. Further details regarding the behavior of SMA phase transformation are inlcuded in Patoor et al. (2006), and D. J. Hartl and Lagoudas (2007).

2.2 SMA actuator material experimental characterization

An experimental method is presented for SMA actuator material characterization which reduces the method to a single-stage experimental process. The primary goal of this experimental characterization is to identify the specific material parameter values for the calibration of a material constitutive model. These material parameters rely on information that quantifies certain expected material phenomenon. Specifically, for SMA actuators we desire to demonstrate the austenite start (A_s^0) and finish (A_f^0) temperatures, the martensite start (M_s^0) and finish (M_f^0) temperatures, the transformation strain (H), as well as information about the phase diagram. Note that these parameters are described in detail in the previous section.

The experemental method commonly used in the past to characterize SMA actuator materials consists of several experimental stages in order to demonstrate the required phenomenon. For example, D. Hartl et al. (2010) performed differential scanning calorimetry (DSC) testing, as well as constant-stress ambient cooling/heating cycles at eight different stress levels in order to demonstrate the desired phenomenon. For the proposed experimentation, instead of using several different material specimens in a multi-stage process, sufficient information may be obtained by using a single specimen in a single experiment in the following proposed experimental method.

For SMA actuator systems, the SMA component will provide an actuation force when a solid-to-solid phase transformation is induced through the component by a change in temperature. Traditionally, this phenomenon is demonstrated by globally cooling and heating SMA material specimens in a controlled, ambient temperature

environment (D. Hartl et al., 2010), (Clingman, Calkins, & Smith, 2003). Several ambient cooling/heating cycles are performed at several different levels of stress so that sufficient information is gathered concerning the transformation behavior; additionally, DSC testing may be performed to identify the transformation behavior at the zero stress condition; the material may also undergo a tensile test at one or more ambient temperatures so that the elastic properties of the material may be determined. However, we propose to replace these multiple testing cycles and specimens with a single-specimen, single-cycle localized heating experiment.

The localized heating experiment is to apply a power input to a small portion of the material specimen, such that some locations on the specimen experience a large change in temperature, while other locations experience very little change in temperature. Thus, while some areas on the specimen undergo full phase transformation, other areas will experience no phase transformation. By experimentally identifying the temperature and deformation at every location on the specimen during the experiment, sufficient data is provided to identify the specific values of the material parameters for the constitutive model.

In addition to simplifying the experimental process, using localized heating for experimental characterzation of the SMA material has a second advantage. Many SMA actuator systems utilizing temperature induced transformation for their actuation power cannot be heated in an ambient enviornment. Rather, for devices which do not have a wire configuration, it is common to place an electrically powered heat source at one or more locations on the mechanism so that the temperature is homogeneous through the body of the actuator for the duration of the actuation of the device (D. Hartl et al., 2010). Since variable heating of SMA actuators is more common, it is more accurate to characterize the SMA actuator material using localized heating: in addition to capturing the mechanical properties of the mate-

rial, the calibrated constitutive model takes into account the heat flow properties in the specimen, and any other phenomenon which could be caused by non-ambient heating. Also, though localized heating was used in these experiements, studying heat conduction properties of SMAs is beyond the study performed here. Rather, quasistatic heating steps have been utilized and a steady state temperature field has been recorded after each heating step.

Calibration of material model parameters using distributed field data from localized heating experimentation relies on solving an inverse problem. Iterative computational simulation of a boundary value problem representing the experiment assuming different (improved) sets of model parameters is used to find the best full library of model parameters for describing the specimen in question. This requires the use of optimization agorithms, and has been described in full detail elsewhere. See Meraghni et al. (2013) for an example of model parameter value optimization work. Recall that deformation data as well as temperature data are known at every point on the specimen. Thus, given this data, one is capable of calibrating the thermal and mechanical aspects of a coupled model. However, to date, the thermal data described in this work has been used only to provide known distributed temperature inputs to an FEA model for calibration (via iterative matching) of the mechanical response.

An overview of the experimental studies performed is presented in the following sections. First, the experimental setup will be presented. Next, experiments which were performed that lead up to the localized heating experiment will be shown. These include a validation experiment for the DIC deformation measurement method, followed by a series of ambient cooling/heating experiments at various stress levels. Finally, two localized heating experiment will be presented.

2.2.1 Specimen description

All experimental data described herein was obtained from tests performed on one of two different material specimens. Both specimens came from an equiatomic NiTi (at. 50.0% Ni) thin plate, heat treated at 450°C, water quenched, and cold-rolled (see Figure 2.1a). The first specimen had a total aspect ratio of 4.0, and will be referred to as the *thin strip* specimen (Figure 2.1b); the second had a smaller aspect ratio of 1.5, and will be referred to as the *plate* specimen (Figure 2.1c). For each specimen, the loading direction was parallel to the direction of rolling applied to the original source plate sample. For each specimen, ambient heating/cooling was performed at two different loads: 200 MPa followed by 100 MPa. An additional cycle at 10 MPa was performed for the thin strip specimen. Immediately following the ambient cooling/heating experiments, a localized heating experiment was performed for each specimen.

(a) Original raw NiTi (at. 50.0% Ni) Sample.

(b) *Thin Strip* specimen.

(c) *Plate* specimen.

Figure 2.1: The thin plate sample sheet and specimens are shown. The load applied to each specimen was in the direction of the sample processing rolling direction.

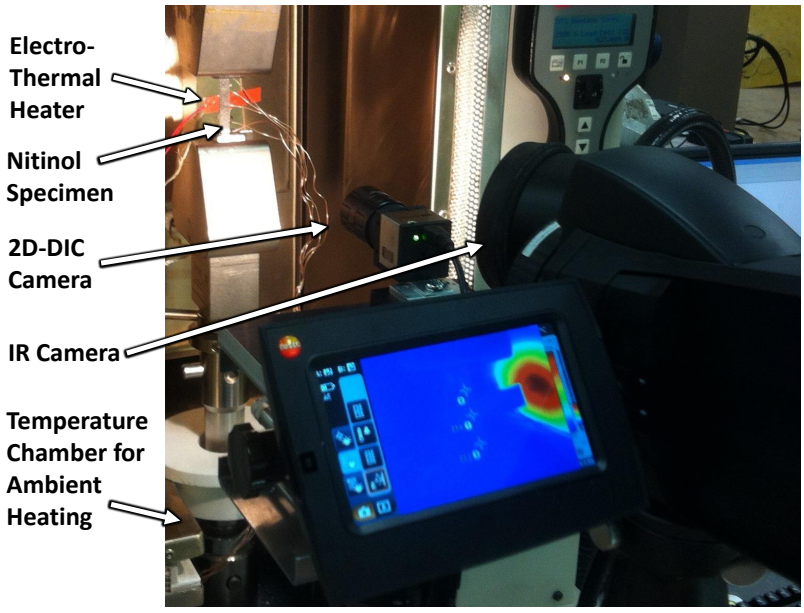

Figure 2.2: Experimental setup, showing the electro-mechanical test stand, the IR camera, and the CCD camera for 2D-DIC.

2.2.1.1 Experimental setup

All experiments were performed using an electro-mechanical screw-driven test stand in a tensile test configuration with a 2500 N load cell. All 2D-DIC measurements were taken using an Edmond Optics 2 megapixel CCD camera with 23 mm lens and all deformation fields were calculated using Correlated Solutions VIC-2D 2009 software. IR measurements were performed using a Testo 885-1 infra-red camera system with a camera precision of 2.0 °C. These equipment are shown in Figure 2.2 in the experimental setup.

Note that in Figure 2.2, the axes of the 2D-DIC camera and IR camera were aligned to provide nearly the same line of sight,maximizing accuracy of measurements by ensuring a nearly-perpendicular orientation relative to the material specimen. Through careful comparison between the IR camera results and associated

thermocouple results, a high degree of confidence was established in the precision of the temperature measurement using the IR camera as calibrated.

The images captured with the IR camera give a value of the temperature for every pixel in the image which depends on the value of the IR emissivity parameter (ϵ). The IR camera resolution is 240x320 pixels; the spatial resolution of the measurement on the specimen was 0.39 mm. ϵ was calibrated in post-processing through careful comparison between the IR temperature results and the TC results. TCs were placed on the back side of the thin (0.03 mm) specimen, and the IR measurement was performed on the front side. The highly reliable results of the TC measurements were compared directly to the IR measurement at the exact locations of the TCs. Comparison of five IR images were made to two TC's. The mean error between the TC and IR measurements after calibration to the TC results was 1.41 °C, with a maximum error of 5.6 °C, and a minimum error of 0.08 °C. The mean error was 2.14 °C. There were two results for which the error was not reasonable which were not used in the analysis. The error was assumed to be in the TC reading at those time points due to noise.

The location of the TC's were identified before the beginning of the experiment, compared to an easily identifiable location. The exact location of the TC's on the IR image we found by measuring the converted distance from a reference location to the TC location on the IR image. Highly reflective aluminum tape was placed at the top and bottom boundary of the specimen (near the grips) in order to easily distinguish the boundary of the specimen in the IR image.

2.2.1.2 Specimen preparation

The specimens were prepared for experimentation in a multi-step process that considered the temperature calibration measurement, 2D-DIC deformation measure-

ment, IR thermography measurement, and application of localized heating. Figure 2.3 shows the processing steps performed for the specimens. First, the specimen was treated to remove the outer oxidation layer then cleaned. Next, thermocouples (TC) were attached to the specimens using a spot-welding technique. Figures 2.3a and 2.3b show the thermocouple placement used for the plate and thin strip specimens, respectively. Subsequently, the electro-thermal heater was attached to the specimen, also shown in Figures 2.3a and 2.3b. Next, a speckle pattern was applied to the specimens for the DIC measurement, where a flat white spray paint was chosen for the background. For the DIC method, a target with very low reflectivity (high emmisivity) is desired, so that there is no reflection from the lighting source during the experiment. A material with a high emissivity value is also desired for IR measurement. Therefore, performing these two tests are highly compatible in terms of surface preparation needs. The black speckle pattern was applied using a flat black acrylic paint with a *TC Omni 3000* airbrush. Figures 5.1b and 5.1a show the speckle pattern used for the plate and thin strip specimens, respectively.

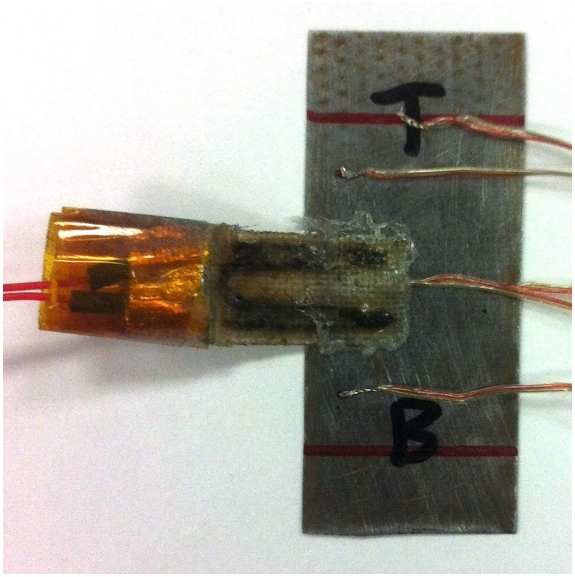

(a) Plate specimen, back: TC and heater.

(b) Thin strip specimen, back: TC and heater.

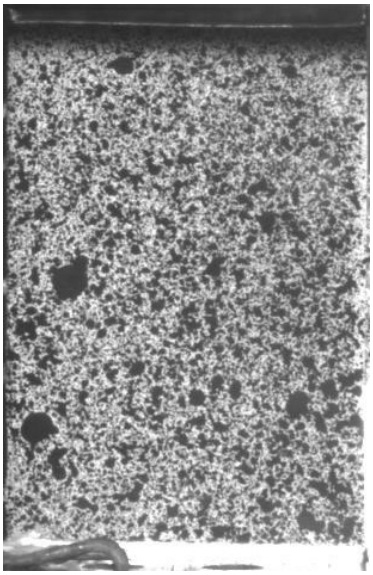

(c) Plate specimen, front: DIC speckle pattern.

(d) Thin strip specimen, front: DIC speckle pattern.

Figure 2.3: Specimen processing is shown. Thermocouples were placed on the specimen for calibrating the IR images. Aluminum tape was placed at the top and bottom of the specimen to mark the boundary of the specimen for IR thermography.

2.2.1.3 Comparison of 2D-DIC to laser extensometry

To demonstrate the consistency of 2D-DIC with other deformation measurement techniques, a separate test was performed previously to compare the 2D-DIC deformation measurement to highly reliable and highly precise laser extensometry data. The specimen used for this test is shown in Figure 2.4a. This specimen was cut from a similar sample as shown in Figure 2.1a, and was used only to show the consistency between 2D-DIC and laser extensometry. The specimen was ambiently heated to 150°C under zero load, then loaded to 200 MPa. Then an ambient heating/cooling cycle was applied during which deformation was measured using 2D-DIC as well as laser extensometry. Temperature was measured by a thermocouple placed next to the specimen.

Figure 2.4 demonstrates the results of this study, showing axial strain ($\varepsilon_{11}=\Delta L/L_0$) vs temperature. The area of interest (AOI) used for the 2D-DIC analysis is indicated in the figure. The DIC ε_{11} results in Figure 2.4b are the average DIC ε_{11} results in this area. The laser extensometer measures the distance from bottom-to-bottom of the reflective markers. To accurately verify the 2D-DIC method by comparison to laser extensometry, the AOI for 2D-DIC should measure a region similar to the one used for laser extensometry, thus the AOI was placed as indicated. Figure 2.4b shows the results of this verification; the strain measurement using 2D-DIC is clearly consistent with laser extensometry. A similar comparison method was used by Reedlunn et al. (2011) in representing their use of 3D-DIC for measuring displacement in SMA wires. This shows that 2D-DIC is a reliable method for deformation and thus strain measurements, and attests to its utility for the present study as a full-field measurement technique.

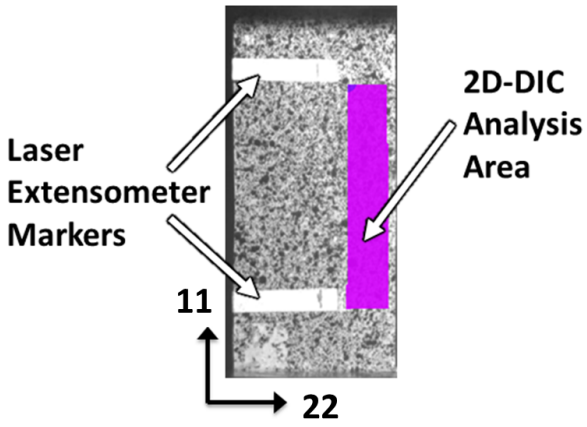

(a) Specimen for 2D-DIC validation and measured regions.

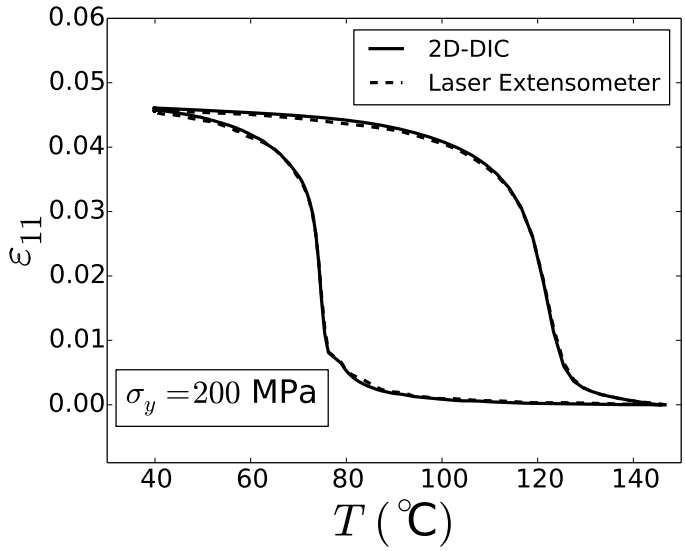

(b) Axial strain (ε_{11}) vs temperature measured by 2D-DIC and laser extensometry.

Figure 2.4: Comparison between 2D-DIC and laser extensometry.

2.2.2 Ambient heating/cooling

To fully understand the response of the material used in this experiment, an ambient heating/cooling cycle study was performed in the traditional manner of SMA actuator material testing (D. Lagoudas (2008), Ch. 2). An additional motive was the verification of the new localized heating calibration method against a more common approach.

In order to reliably demonstrate consistency between the two types of characterization experiments, the ambient heating/cooling cycle experiment was performed on the same specimen subsequently used for the localized heating experiments. Both experiments were performed one right after the other in order to minimize discrepancy with regard to preparation, gripping, loading, and load control, etc.

The following steps describe the process used to perform the ambient heating/cooling cyclic testing and prepare the specimen for the localized heating tests:

1. Heat specimen to above austenite finish temperature.

2. Apply 200 MPa to specimen.

3. Cool to 40°C, and heat to 160°C.

4. Unload specimen to 100 MPa.

5. Cool to 40°C, and heat to 160°C.

6. Apply 200 MPa to specimen.

7. Cool specimen to 40°C.

8. Perform localized heating on the specimen.

Figure 2.5 shows the ε_{11} ($^{\Delta L}/_{L_0}$) vs. temperature results of the ambient heating/cooling experiment for both specimens. These tests were performed by ambient heating/cooling the material under constant applied load using a heating chamber (see Figure 2.2). Temperature was measured by a thermocouple placed next to the specimen, and strain was measured by 2D-DIC through the window of the heating chamber. In these figures, the effects of transformation induced plasticity (TRIP) can be seen. The specimens were first cycled at 200 MPa, then again at 100 MPa: with increased cycles, the material behavior stabilizes. The difference in TRIP between cycles is much more prevalent in the first few cycles than subsequent cycles. Therefore, the rapid decrease in TRIP between the 200 MPa and the 100 MPa cycles is expected (Reedlunn et al., 2011). Figure 2.5a also shows the cycle performed at 10 MPa for the thin strip specimen. Because the load applied was below the required stress for the selection of preferred martensitic varients, no actuation strain was observed in the material during the temperature cycle.

For the plate specimen, the applied load data was lost after the completion of the test due to a software malfunction. However, it may be said with high confidence that the load applied to the specimen during the test was as reported. Furthermore, the DIC data and temperature data were both retained, with high confidence. Each stage of the experiment was performed at a constant stress/applied load.

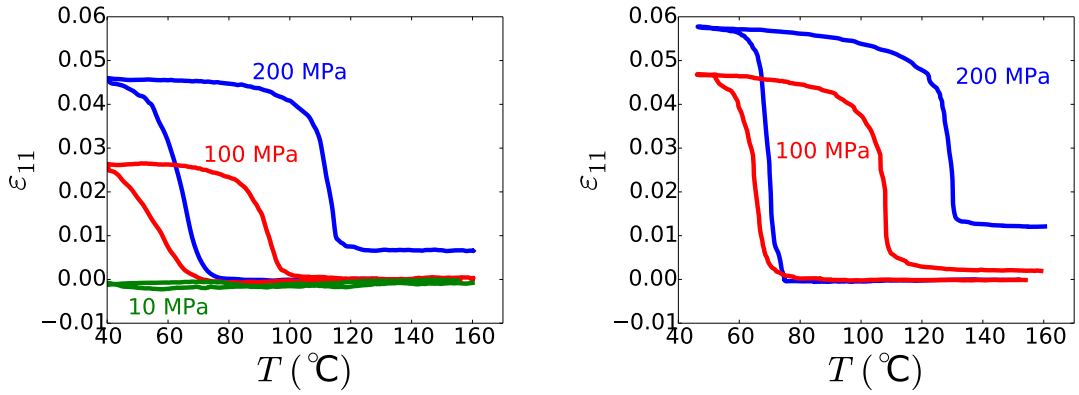

(a) Thin strip specimen.

(b) Plate specimen.

Figure 2.5: Axial strain (ε_{11}) vs temperature showing the ambient heating/cooling of the two specimens. There are noticeable effects of transformation induced plasticity (TRIP) in the 200 MPa response.

Figure 2.6 shows the ambient heating/cooling results modified to not include the effects of TRIP. Figure 2.5 was reduced to create Figure 2.6. These figures demonstrate the recoverable strain from the experiment, and may be used to obtain information about the material behavior.

Figure 2.7 shows the phase diagram for the thin strip and plate specimens. In the stress (F/A_0) vs temperature space, when the material state is to the left of the M_f line, the material is in martensite ($\xi = 1$). When the material state is to the right of the A_f line, the material is in the austenite phase. The points indicated are data obtained from Figure 2.6 by the tangent line method (D. Lagoudas (2008), Section 2). The slope of the M_f and M_s lines (C_M) as well as the slope of the A_s and A_f lines (C_A) were determined by the equation

$$C_\gamma = 1 \,/\, \left(\frac{1}{C_{\gamma_s}} + \frac{1}{C_{\gamma_f}} \right) \tag{2.1}$$

where $\gamma = M,\ A$; C_{γ_s} and C_{γ_f} are the slopes of the γ_s and γ_f lines (i.e., the lines passing through the data points). For the current experimental results, the critical transformation temperatures (A_f, A_s, M_f, M_s) in the phase diagram were assumed to have a linear realationship with applied load, although not always the case (Wu, Sun, & Wu, 2003).

2.2.2.1 DIC measurement method

The DIC measurement performed for the data of Figures 2.6 and 2.5 was taken as an average of the DIC data over a small area near the center of the specimens. Figure 2.8 shows a comparison between different types of DIC measurement. The analysis of a single point in the center of the specimen is slightly different than the analysis of an average over a line or an area, which are both very similar to each other, with a maximum difference of 0.2% axial strain between the analysis at a single point and the average along a line. This comparison shows that the DIC measurement method

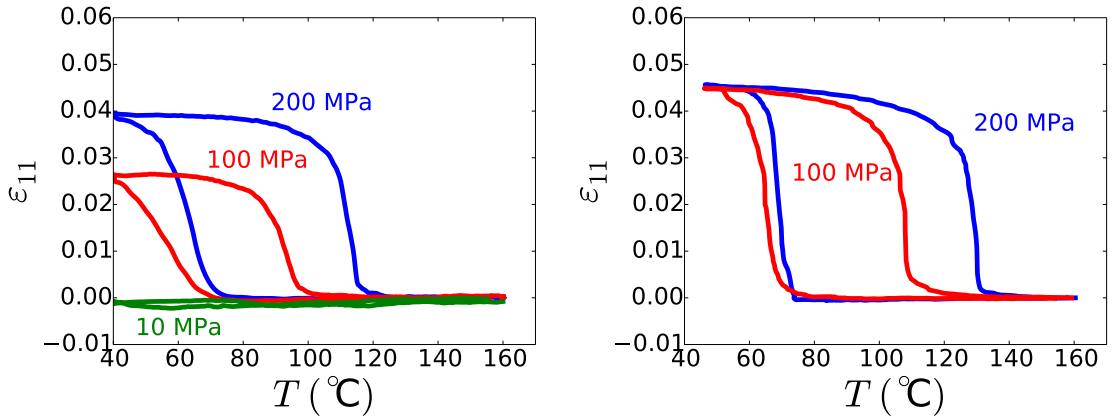

(a) Thin strip specimen.

(b) Plate specimen.

Figure 2.6: ε_{11} vs temperature showing the ambient heating/cooling for each of the two specimens. The figures were modified to exclude the effects of TRIP in these initial thermal cylces of the material.

used for the data in Figures 2.6 and 2.5 is valid and is comparable to a traditional extensometer measurement (represented by the average over the line).

2.2.3 Localized heating

A visual representation of the localized heating experiments is provided by Figures 2.9 and 2.10. Figures 2.9a and 2.10a show how the localized heating was supplied to

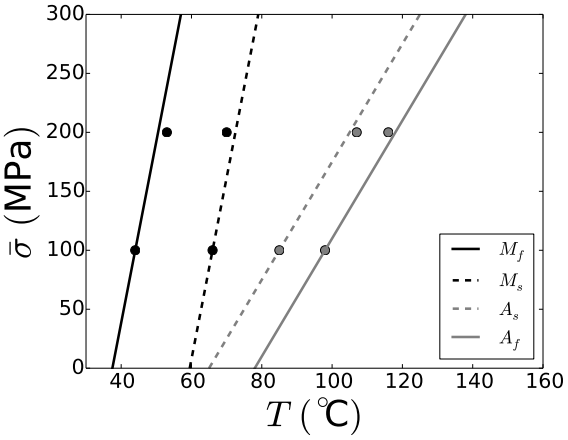

(a) Thin strip specimen material phase diagram.

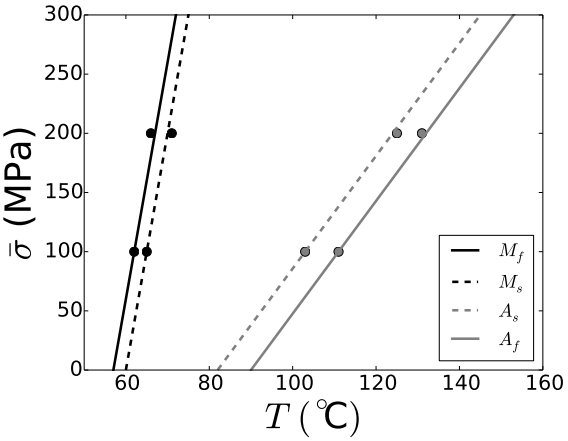

(b) Plate specimen material phase diagram.

Figure 2.7: Stress vs temperature phase diagram estimated by data from Figure 2.6. $\bar{\sigma}$ represents the effective applied stress.

the specimen via an electro-thermal fabric heater attached to the specimen opposite the painted side for the thin strip and plate specimens, respectively. Quasistatic heating was performed by supplying stepwise increasing DC power to the heater via an OTE HY3003 power supply.

Infrared thermography (Testo 885-1 infrared camera system, see Figure 2.2) captured the temperature distribution resulting from the localized application of heating power. The emissivity was calibrated to be 0.43. Figures 2.11 and 2.12 show the temperature fields for the thin strip and plate specimens, respectively recorded using

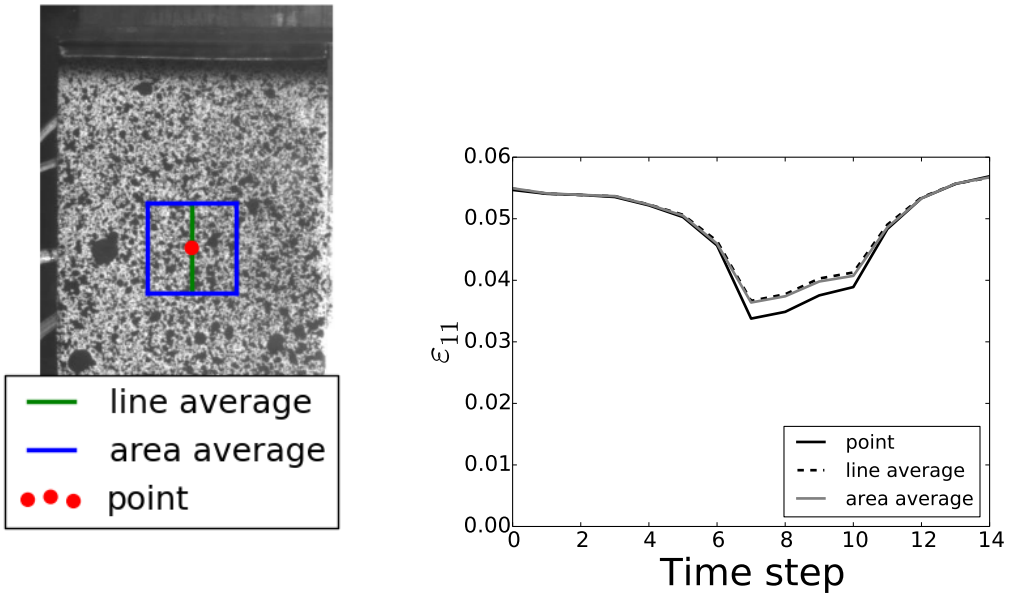

(a) A picture showing the analysis point, line average, and area average on the specimen surface used in this analysis.

(b) Axial strain (ε_{11} vs time plot demonstrating the difference in different types of measurements using DIC.

Figure 2.8: Comparison of three different types of DIC measurement. Analysis at a single point in the center of the specimen is compared to analysis via an average over an area, and an average along a line.

IR thermography at the indicated time steps (1-22 for thin strip, 1-15 for plate). For localized heating, it is assumed that the variation of temperature through the thickness of the specimen is negligible. Note that the power values shown for the thin strip (Figure 2.11a) are significantly higher than the power reported for the plate specimen (Figure 2.12a). This discrepancy is due to the difference between the type and installation of electro-thermal heater used, where the heater used for the thin strip specimen was only partially attached to the specimen (see Figure 2.11a), and thus was less efficient in transferring power into the material.

(a) Specimen configuration (back side).

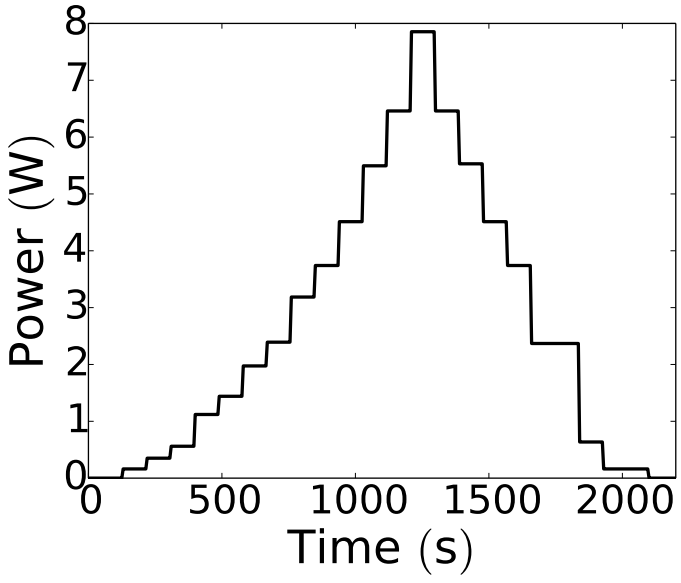

(b) Power applied to thin strip specimen heater.

Figure 2.9: Power applied to thin strip specimen.

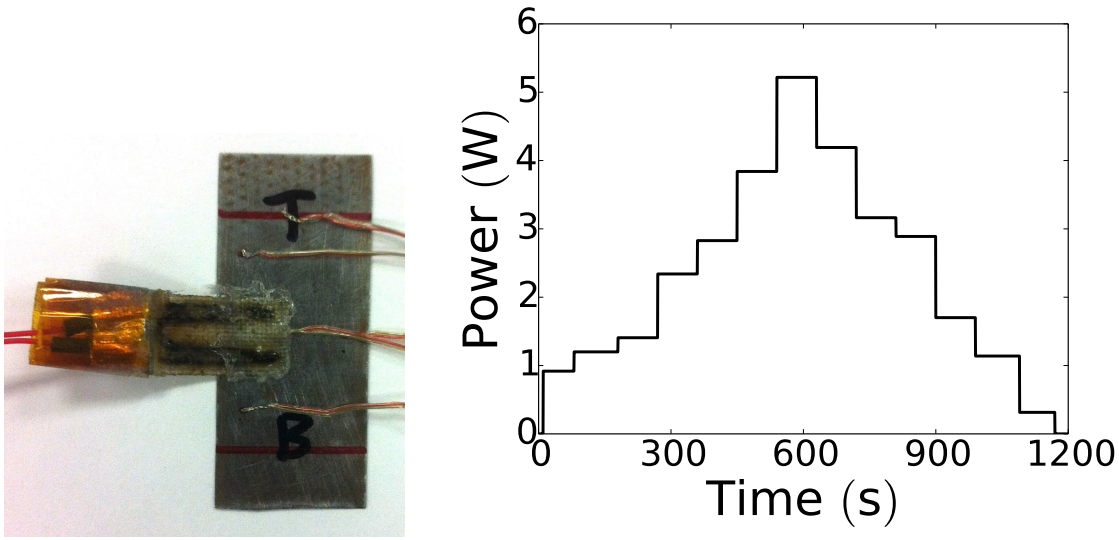

(a) Specimen configuration (back side).

(b) Power applied to plate specimen heater.

Figure 2.10: Power applied to plate specimen.

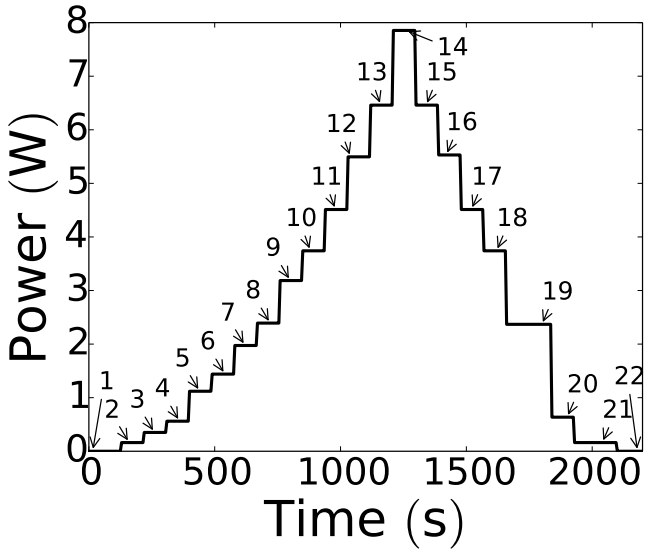

(a) Power applied over time.

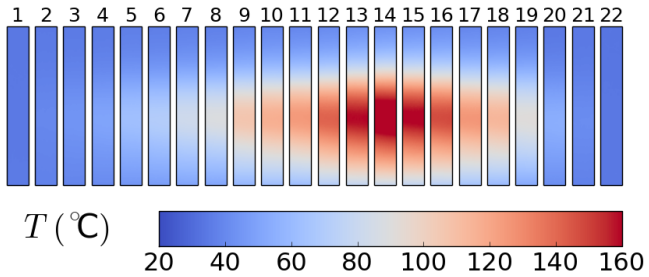

(b) Spatial temperature distribution over time.

Figure 2.11: Temperature fields at the indicated time steps (1-22) for the thin strip specimen.

2.2.4 Localized heating in a single dimension: thin strip specimen

Note that all results provided herein are associated with a planar region of the specimen that does not include specimen edges. This is illustrated via the contour colored region of Figure 2.13, which shows an example of the DIC results. While this image shows the boundaries of the specimen, the response at the boundaries cannot be calculated by DIC analysis because extrapolation to the boundaries is not reliable

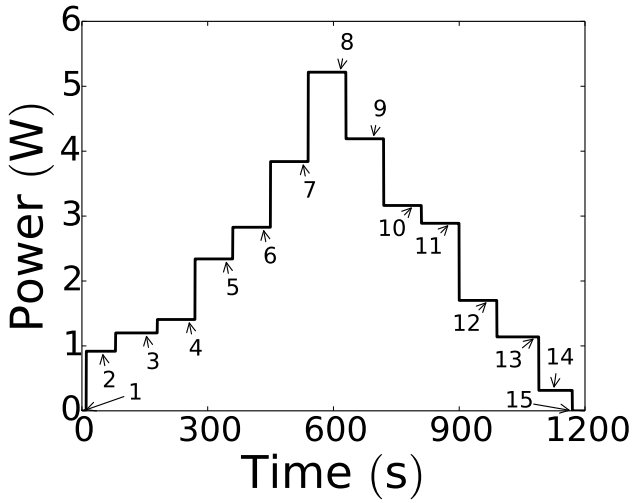

(a) Power applied over time.

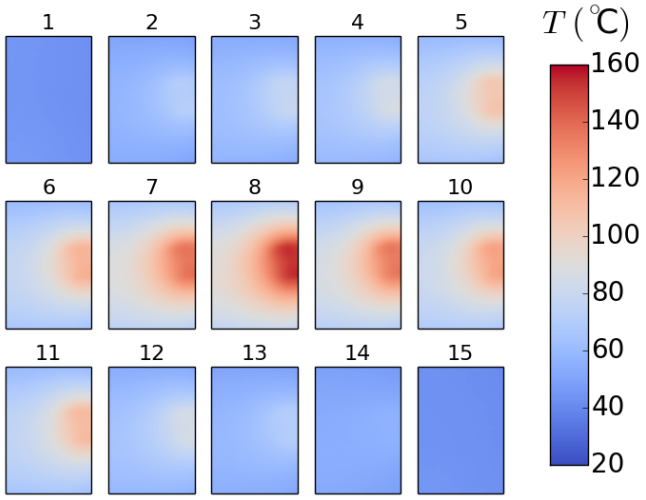

(b) Spatial temperature distribution over time.

Figure 2.12: Temperature fields at the indicated time steps (1-15) for the plate specimen.

in this framework, especially when the boundary moves in response to loading and transformation. Therefore, in the following representations of distributed strain, the full specimen is not completely represented, but only the colored contour subdomain shown in Figure 2.13. The boundaries for the temperature field data were defined such that they match the boundaries of the DIC data exactly.

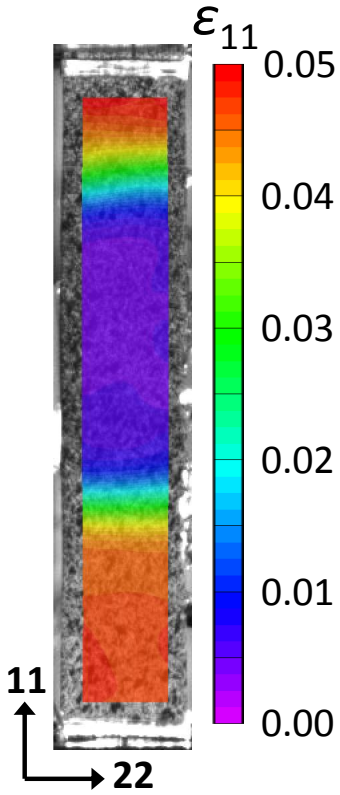

Figure 2.13: Illustration of the DIC-analyzed subdomain (and, by extension, thermography subdomain) used in the subsequent figures. This figure shows the axial strain (ε_{11}) contour plot at the time step for maximum power (P=7.9 W).

All distributed field data (temperature and in-plane strain components) are shown simultaneously in Figure 2.14. Specifically, the temperature, axial strain, transverse strain, and shear strain fields at each time step (1-22, see Figure 2.11) are provided. The spatial resolution of the DIC measurement for the strain results is 0.136 mm per image pixel, and the results shown in Figure 2.14 have a spatial resolution 0.544 mm per reported analysis point. The strain resolution was calculated by dividing the spatial resolution by the length of the primary axis of the specimen, and was calculated to be 0.004 mm/mm. The localized strain response to the applied temperature variation in the specimen is observed throughout, where it is clear that the effect of the upper and lower grips has little effect and is highly localized.

One of the key advantages to this approach is the ability to quantify a range of thermally induced transformation responses, from full hysteresis loops in sufficiently heated regions, to partial loops, to closed paths in non-transforming regions. While Figure 2.14 provides all of this information simultaneously, it is difficult to interpret quantitatively. For this purpose, Figure 2.15 directly illustrates the thermally induced actuation strain responses at points ranging from fully to non-transformed.

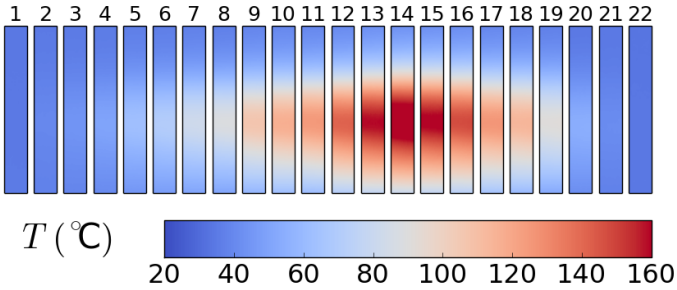

(a) Temperature measured with IR camera.

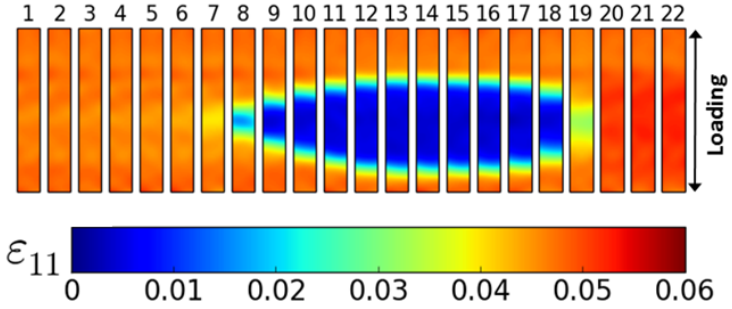

(b) Axial strain (ε_{11}) in the loading direction.

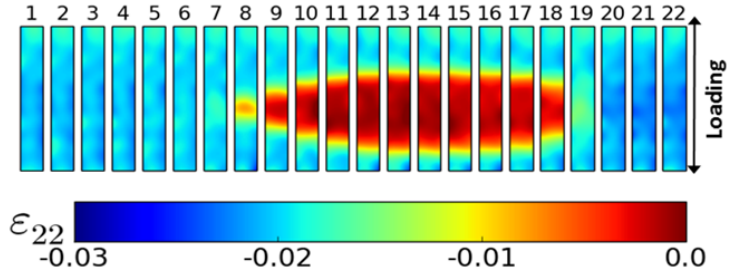

(c) Transverse strain (ε_{22}).

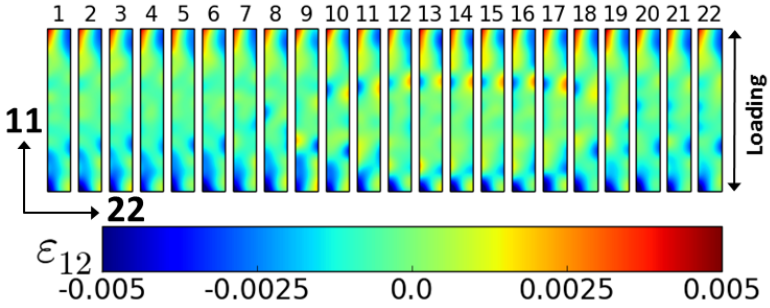

(d) Engineering shear strain ($\gamma_{12} = 2\varepsilon_{12}$).

Figure 2.14: Full-field temperature and strain measurements for the thin strip specimen.

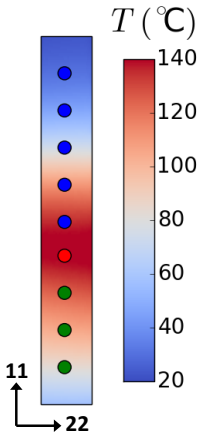

(a) Location of plotted points ($P = 7.9\ W$).

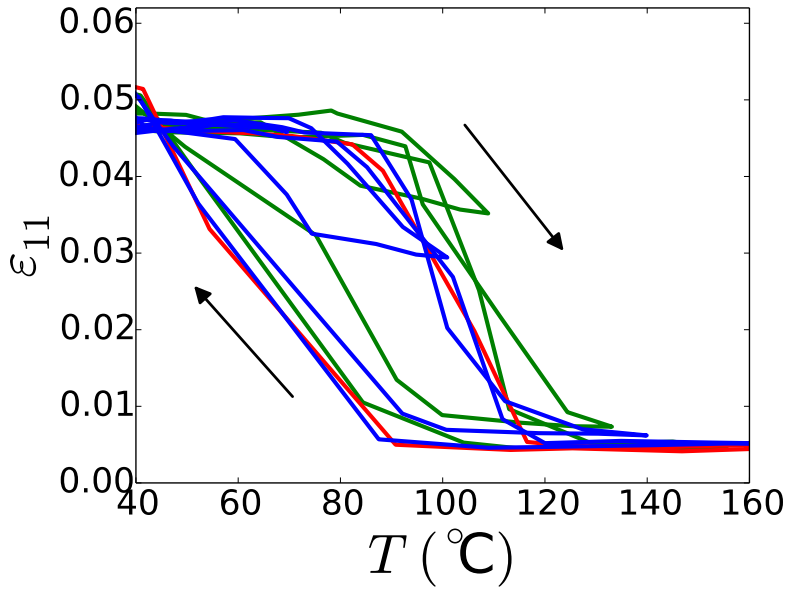

(b) ε_{11} vs temperature response of indicated points during temperature cycle.

Figure 2.15: ε_{11} vs temperature at identified analysis points. The red curve in (b) is the point which experienced the most temperature variation. The points with more temperature variation show greater hysteresis.

2.2.5 Localized heating in two dimensions: plate specimen

Here we repeat the exploration previously described for the thin strip, but applied to the plate specimen. A richer experimental response is ensured by the asymmetric placement of the heater, which results in temperature gradients and induced stress gradients. The low aspect ratio of the specimen also induces additional stress gradients. The same general results (contour and line plots) are presented as for the thin strip, although a more nuanced discussion is made possible by the 2-D field distributions.

The regions for the analyses performed herein are shown graphically in Figure 2.16. The plate specimen is shown and the subdomain that was used for DIC analysis is clarified (ε_{11} results at the 8^{th} time step, P=5.3 W). Thus for the strain results, the full specimen is not completely represented, but only the colored contour area shown in Figure 2.16. The boundaries for the temperature field data were defined such that they match the boundaries of the DIC data exactly.

The data obtained by this experiment are graphically summarized in Figure 2.17, where the temperature, axial strain, transverse strain, and shear strain fields at each time step are all shown. The spatial resolution of the DIC measurement for the strain results is 0.0901 mm per image pixel, and the results shown in Figure 2.17 have a spatial resolution 0.360 mm per reported analysis point. The strain resolution was calculated as the spatial resolution divided by the length of the primary axis of the specimen, and was calculated to be 0.003 mm/mm. In Figures 2.17b and 2.17c the strong transformation-induced strain gradients arising from the temperature variation in the specimen are observed. We can make a few qualitative observations from these results. First, we observe the expected 2-D distributions that are not present in the strip experiments. These large strain gradients in particular will lead to sharp

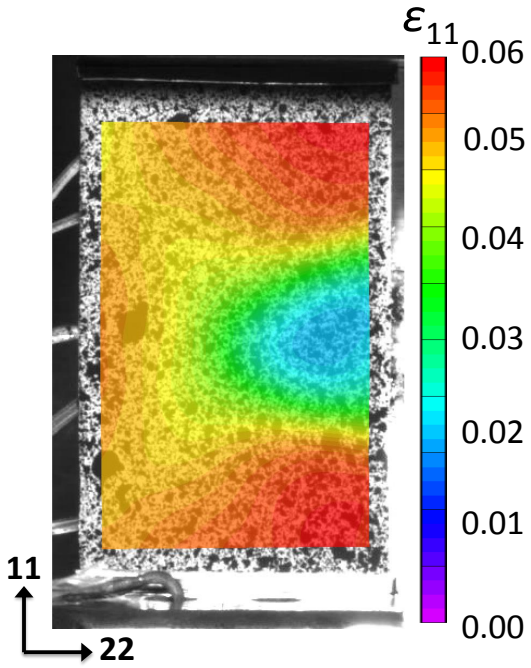

Figure 2.16: Illustration of the DIC-analyzed subdomain (and, by extension, thermography subdomain) used in the subsequent figures. This figure shows the axial strain (ε_{11}) contour plot at the time step of maximum power (P=5.3 W).

stress gradients across the specimen width given the coordinated application of force and deformation to the gripped (i.e., top and bottom) boundaries. Secondly, we notice a shear symmetry in the thermal and axial to transverse strain results, and an associated anti-symmetry in the shear strains. The minor deviation from perfect symmetry is thought to be a result of non-ideal heater installation. Finally, we notice the more pronounced interaction between boundary (grip) effects and thermal non-homogeneity resulting from the low aspect ratio of the specimen. It is expected that all these features will increase the utility of the data for the purposes of iterative constitutive model calibration.

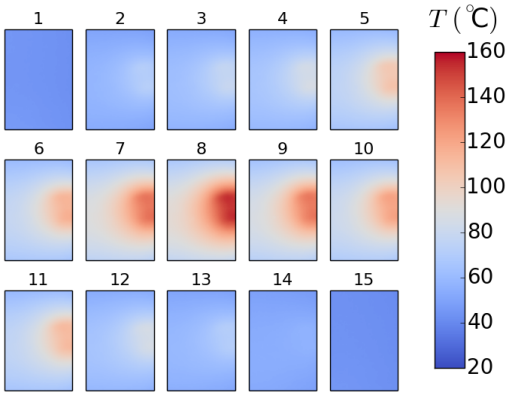

(a) Temperature measured by IR camera.

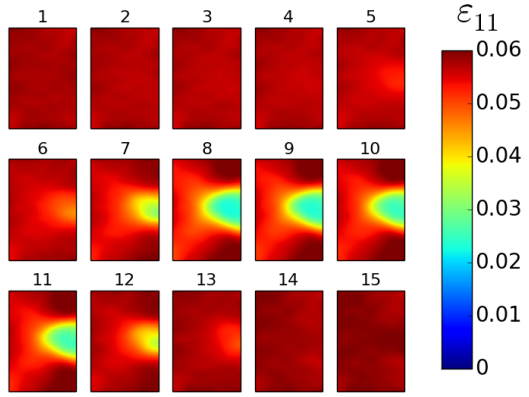

(b) Axial strain (ε_{11}) in the loading direction.

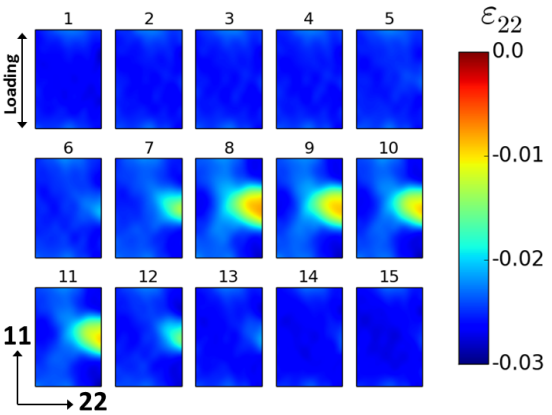

(c) Transverse strain (ε_{22}).

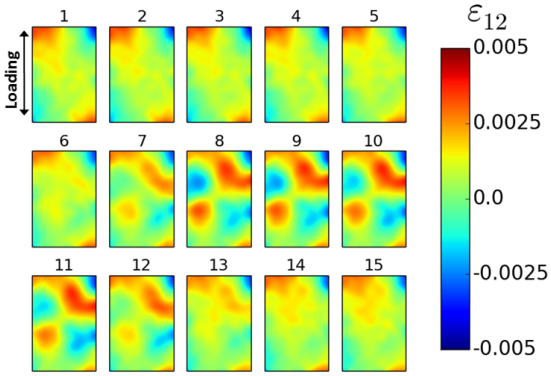

(d) Engineering shear strain ($\gamma_{12} = 2\varepsilon_{12}$).

Figure 2.17: Full-field temperature and strain measurements for the plate specimen.

The strain measurements shown in Figure 2.17 are the strains with respect to the material at zero load and 160 °C. However, the original data was obtained by two separate measurements: the first measurement was a DIC measurement from zero load at 160 °C to 200 MPa at 160 °C. The second measurements were from 200 MPa at 160 °C to the state at the time of each respective IR measurement. Because there were two separate measurements made, the results of the first measurement had to be added to the second measurement. The point-wise strain data of the first measurement was added to the second measurement using a bilinear interpolation algorithm, as follows:

$$\begin{aligned} R_1 &= \frac{x_2 - x}{x_2 - x_1} Q_{11} + \frac{x - x_1}{x_2 - x_1} Q_{21} \\ R_2 &= \frac{x_2 - x}{x_2 - x_1} Q_{12} + \frac{x - x_1}{x_2 - x_1} Q_{22} \\ P &= \frac{y_2 - y}{y_2 - y_1} R_1 + \frac{y - y_1}{y_2 - y_1} R_2, \end{aligned} \tag{2.2}$$

where P represents the value at the destination of the interpolation, and Q_{11}, Q_{12}, Q_{21}, and Q_{22} are the values of the interpolated data surrounding the destination point. This algorithm is illustrated in Figure 2.18.

As in the previous section, the results of this experiment can be more quantitatively represented by ε_{11} vs temperature plots at chosen locations throughout the specimen. The various points that were analyzed are shown in Figure 2.19a (color-contour plot at the 8^{th} time step, P=5.3 W). The points which were analyzed are as indicated, and the numbered plots (1-4) are based on distance from the right edge of the specimen; the colors are based on the axial position of the analysis point.

Clearly the richest data set is that associated with Column 1 and shown in Figure 2.19b. Here the red line associated with the mid-span of the specimen represents the most complete transformation undergone by any point on the specimen. Recall that,

given the specimen initialization procedure, the state of the specimen prior to heating is homogeneously martensite, (oriented in the axial y-direction, $\varepsilon_{11} = 0.055$ and T = 40°C). Upon heating, all points that reach $\sim$ 100°C begin reverse transformation to austenite, as evident by the recovery of inelastic transformation strains. According to Figure 2.19b, the red point in the center of the left side is heated the most, reaching a temperature of 160°C at which time it was still observed to be transforming. The decrease in power and resulting reduction in temperature abruptly ended reverse transformation for all points; forward transformation into martensite began at $\sim$ 100°C as well, and seems to have completed by T= 70°C.

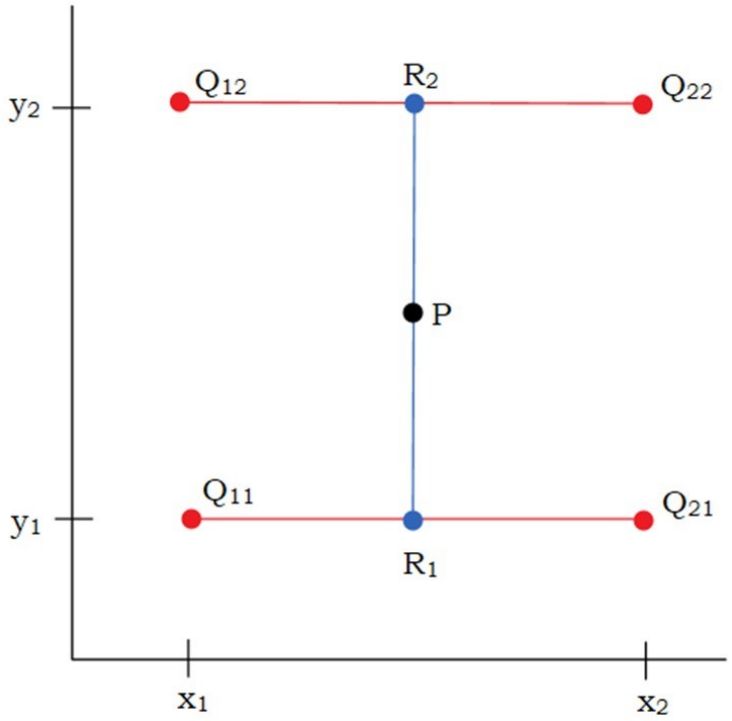

Figure 2.18: Illustration of the bilinear interpolation method, Equation 2.2.

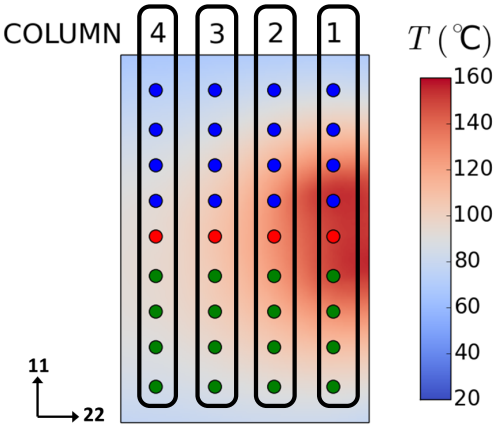

(a) Analysis points, organized in four different columns (vertically oriented).

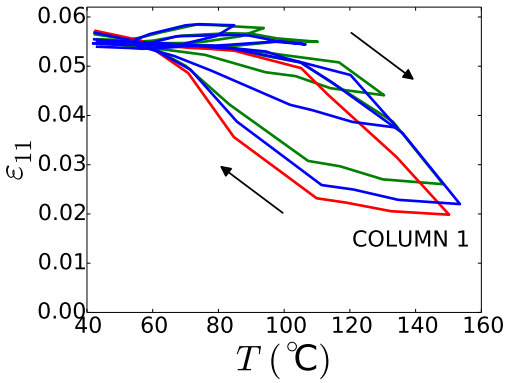

(b) Column 1: the *most thermal inhomogeneity* (from the top to bottom) is observed in this column.

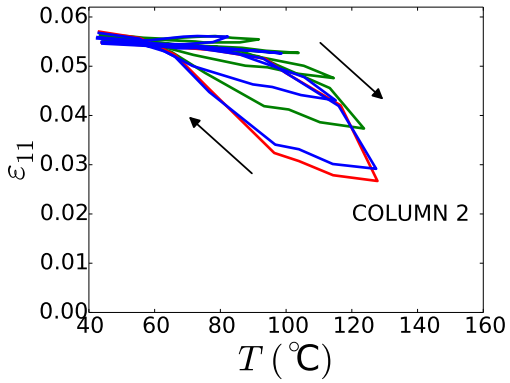

(c) Column 2.

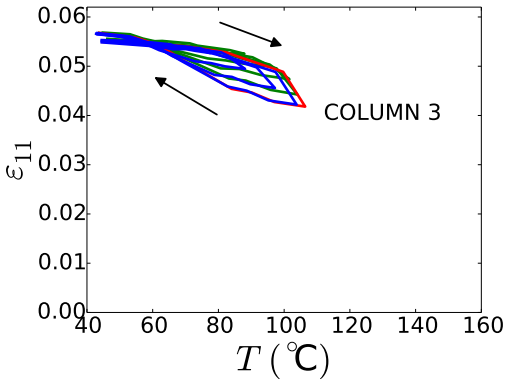

(d) Column 3.

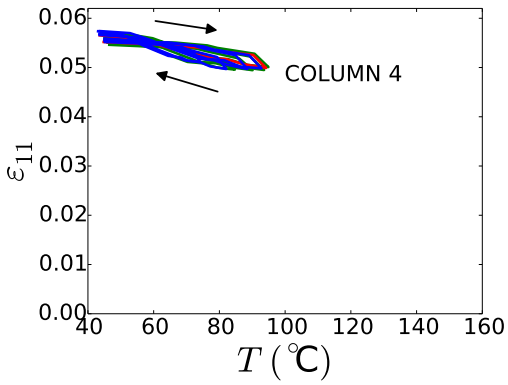

(e) Column 4: the *least thermal inhomogeneity* (from the top to bottom) is observed in this column.

Figure 2.19: ε_{11} vs temperature response of identified analysis points. Each of the four ε_{11} vs temperature figures (b)-(d) demonstrate the results at each of the four respective columns of analysis points shown in (a).

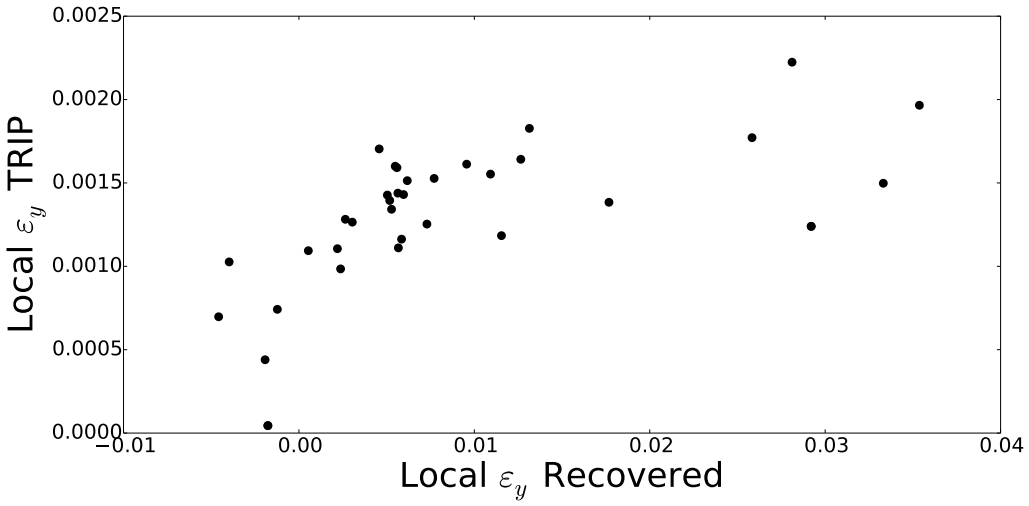

Figure 2.20: A comparison between the amount of TRIP for ε_{11} and the recovered ε_{11} for each analysis point indicated in Figure 2.19a.

Once again the effects of TRIP can be observed in points across the sample, though the consequences are relatively minor in relation to the recoverable strain. The red point of Column 1 completed the transformation cycle with a net positive tensile strain generation of 0.2%. Investigation of the data indicates that, from point to point, the amount of TRIP locally observed was directly proportional to the amount of transformation strain recovered during heating. This is visualized in Figure 2.20, which shows the amount of TRIP at each analysis point compared to the amount of ε_{11} recovered. This further demonstrates the utility of this thermo-mechanical full-field approach as a path toward the better understanding of TRIP behaviors in SMAs.

2.2.6 Comparison with ambient heating/cooling

One of the key motivations underlying these experiments is the desire to gain a richer data set of stress-strain-temperature responses than can be obtained from traditional gage section-based approaches. Thus, we compare directly data obtained

from each. Figure 2.21 shows the ambient heating/cooling cycle at 100 and 200 MPa (c.f. Figure 2.5b) overlayed with the localized heating strain-temperature results taken from the location indicated for the plate specimen. It appears that the material point from which the localized heating data was taken did not experience full reverse transformation upon heating. Thus, the axial transformation strain measured by the localized heating/cooling curve does not match the transformation strain indicated by the ambient heating curve. [1]

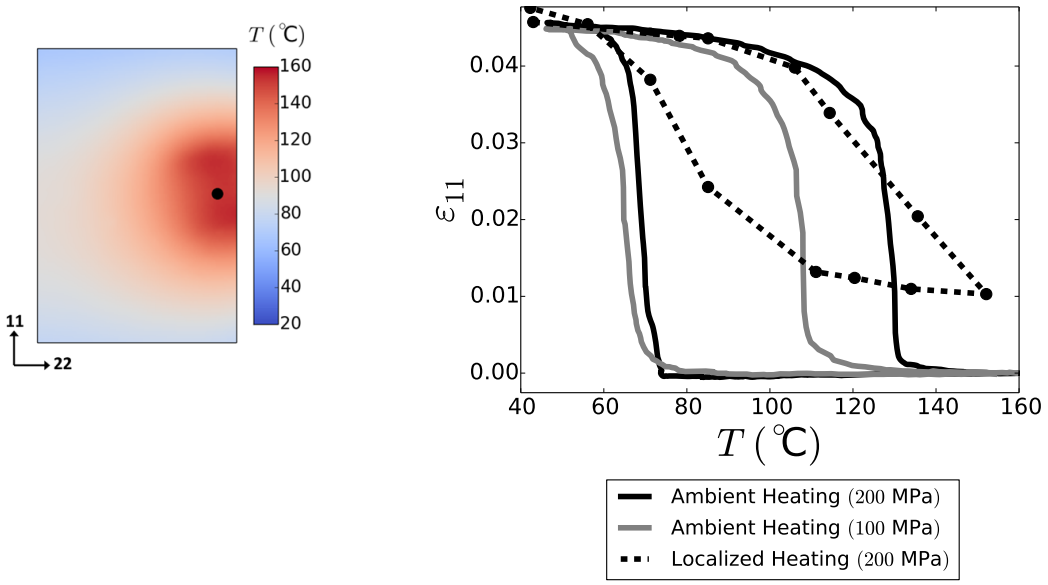

(a) Plate specimen with analysis point as indicated.

(b) ε_{11} vs temperature plot for localized heating at analysis point, compared with ambient heating/cooling results. (Local heating results adjusted)

Figure 2.21: A direct comparison between localized heating and ambient heating/cooling cycles for the plate specimen. The localized heating experiment did not complete reverse transformation.

[1]Note that the localized heating curve in Figure 2.21 was resolved such that the strain at the beginning of the test is the same as the maximum transformation strain achieved in the ambient cycle at 200 MPa. This was done to provide an easy comparison between the results. Actual strain levels for the localized heating experiment are shown in Figure 2.19b.

There are two major differences between the experimental conditions applied during localized heating as compared to ambient cooling/heating. Change in temperature for the ambient cycle occured in a quasistatic manner (2.0°C per minute) for the whole specimen homogeneously so that the stresses in the specimen away from the grips could be assumed constant. In comparison, the stress field for the localized heating experiment cannot be uniform throughout the specimen during localized heating due to resulting localized strain recovery. Although evenly stressed at a nominal level of $F/A_0 = 200$ MPa during ambient heating/cooling, stress gradients developed when heat was applied to the material in a localized region. Specifically, as the material points near the heater reached the austenite start temperature, they began to contract axially while the rest of the speicmen remained at a temperature below A_s. Thus, the region where the heat was applied experienced an increased level of stress due to the lack of transformation occurring in the material surrounding it. The increased stress in this region caused the temperature for reverse transformation to increase significantly as per Figure 2.7b. Notice in Figure 2.21 that the A_s temperature for the localized heating result is similar to the A_s temperature for the ambient cycle at 200 MPa. As the temperature at the heating location continued to increase, the stress there also increased, thus driving the temperature for reverse transformation at that point higher and higher and suppressing reverse transformation. Though the load applied to the boundaries of the specimen remained the same, stress was redistributed throughout the specimen due to spatial variation in thermally induced transformation (and thus deformation); the strongest stress gradient was generated in the direction transverse to the loading direction such that the area at which heat was applied (right-side boundary) experienced a much gfreater stress level than the points on the unheated side (left-side boundary). Finally, at 160 °C, which was above the austenite finish temperature for the ambient cycles, the material at the right-side

boundary had not yet achieved A_f. Upon cooling, the stress in the material began to homogenize decrease after the beginning of forward transformation (above M_s) until a uniform 200 MPa was once again prevalent in the material at the end of cooling (40°C).

Figure 2.22 also shows a comparison between the localized heating experiment and an ambient cooling/heating experiment performed for the thin strip specimen. Notice that full reverse transformation did occur for the thin strip at the indicated analysis point, whereas it did not for the plate specimen (c.f. Figure 2.21).

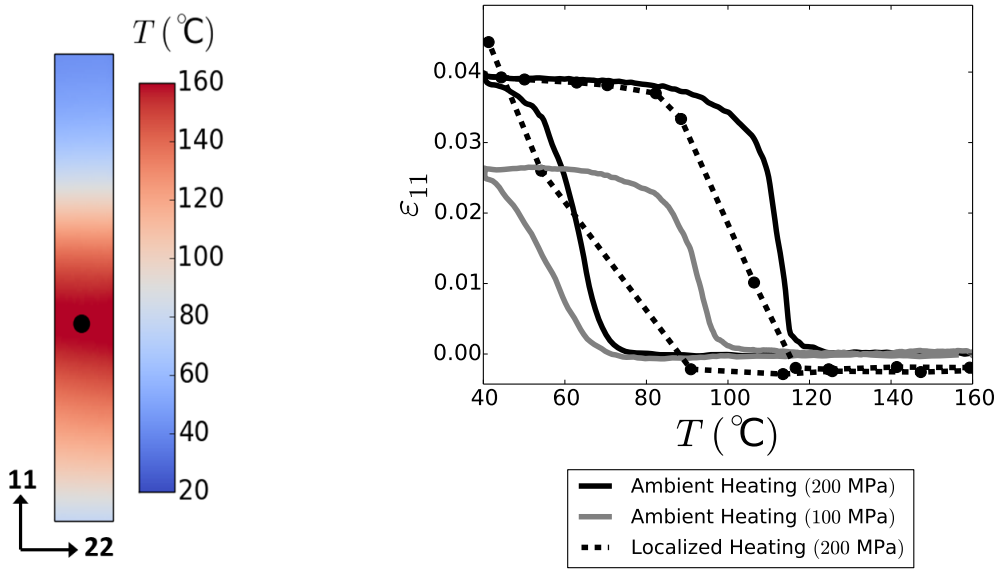

(a) Thin strip specimen with analysis point as indicated.

(b) ε_{11} vs temperature plot for localized heating at analysis point, compared with ambient heating/cooling results (Local heating results adjusted).

Figure 2.22: A direct comparison between localized heating and ambient heating/cooling cycles for the thin strip specimen. The localized heating curve and amibient heating/cooling curve show similar phase transformation properties for this specimen.

2.2.7 Focused assessment of strain components

In addition to the utility of measuring and assessing the three in-plane strain components in a spatially continuous manner, the methods employed herein also allow for the direct and local assessment of strain ratios for the purposes of both constitutive model motivation and calibration. An analysis of the strain ratios for the thin strip and plate localized heating experiments are demonstrated in Figure 2.23. This data was taken from the axial (ε_{11}) and transverse (ε_{22}) strain results at the locations indicated in Figures 2.21a and 2.22a for the plate and thin strip specimens, respectively, during the localized heating experiments. With regard to the elastic response, the Poisson's ratio for both the austenite and martensite elastic phases are often reported to be $\nu = 0.33$ (Jani et al., 2014) (Churchill et al., 2010). Most constitutive models, on the other hand (Boyd & Lagoudas, 1996) (Auricchio et al., 1997) assume that forward (and by extension, reverse) phase transformation occur in an isochoric manner (D. Lagoudas, 2008), for which the ratio of transverse to axial strain is -0.5 by definition.

The nominal values of $\varepsilon_{22}/\varepsilon_{11} = -0.33$ for elastic deformation and $\varepsilon_{22}/\varepsilon_{11} = -0.5$ for transformation are demonstrated in Figure 2.23. These figures demonstrate that the material tends to follow the $\varepsilon_{22}/\varepsilon_{11} = -0.33$ prediction during elastic deformation. Then, as transformation progresses a transition occurs such that the ratio evolves towards $\varepsilon_{22}/\varepsilon_{11} = -0.5$, which is as predicted. As outlined previously, the localized heating experiments began in the martensite phase ($T < M_f^\sigma$, $\varepsilon_{11} \approx 0.05$) and transitioned to the austenite phase ($T > A_f^\sigma$, $\varepsilon_{11} \approx 0.00$). For the plate specimen the austenite finish (A_f^σ) temperature was not achieved, thus the data did not reach $\varepsilon_{11} \approx 0.00$ as seen in Figure 2.23a; however, at the beginning of cooling the plate specimen at this point experienced a reversion to elastic deformation before forward

transformation occured which can be seen in Figure 2.23a.

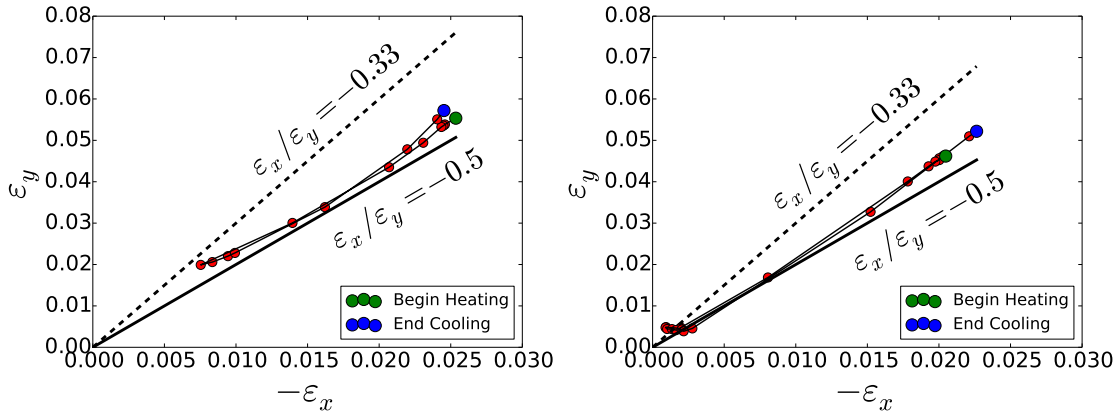

(a) Plate specimen, localized heating.

(b) Thin strip specimen, localized heating.

Figure 2.23: Axial strain (ε_{11}) vs transverse strain (ε_{22}) for the plate and thin strip specimens during localized heating. The green point indicates the beginning of the localized heating experiment, and the blue point shows the end of cooling. The lines connecting the points indicate the evolution of the experiment.

2.3 Summary and conclusions

Experimental characterization of SMA materials is critical for their use as actuators. This is a key step in actuator design optimization, used for calibrating the SMA material model.

Two SMA specimens were tests using localized heating. These experiments demonstrate a reduction in the number of experiments necessary for material model calibration. Heat was applied to the specimens under load in a non-uniform manner such that various degrees of phase transformation were achieved at different locations on the specimen. Different locations on the material specimen demonstrated a different level of maturity in the strain recovery hysteresis loop for the material;

likewise, the stress field in the specimen was redistributed due to highly localized deformation. The varied response of the material due to the localized heating was measured by 2D-DIC and IR thermography. The highly coupled, yet accurately and precisely measured material response to localized heating provide an excellent method for SMA material calibration.

3. EXPERIMENTATION PART II: CHARACTERIZATION OF MACROSCOPIC PSEUDOELASTIC SHAPE MEMORY ALLOYS USING MEUWISSEN GEOMETRY

3.1 Introduction

A phenomenal method for characterization of pseudoelastic SMA materials is presented in this section. This method features a characterization technique which reduces the number of experiments necessary to obtain high fidelity data and accurately demonstrates material behavioral response to a wide range of load states.

The experiments and analysis shown here serve as a continuation of the recently published work, Meraghni et al. (2013). In a progressive effort to describe the response of pseudoelastic shape memory alloy (SMA) materials to a variety of loading paths, Meraghni et al. (2013) describes testing performed on homogeneous "dog-bone" shaped specimens for uniaxial testing in tension; the experiments shown in this section continue that work by demonstrating non-uniformly shaped specimens also with applied load in tension; future work in this effort will also consider biaxial testing.

Progressively more complex loading schemes are necessary to demonstrate material response to irregular loading, and may range from uniaxial testing of SMA wire to biaxial loading of SMA cruxiform specimens. Pseudoelastic uniaxial tensile testing of SMA wire is widely accepted and published (J. A. Shaw & Kyriakides, 1995). Furthermore, Meraghni et al. (2013) demonstrated tension testing of non-wire dogbone shaped specimens. The work presented in this section shows uniaxial loading of a specimen with non-uniform geometry. These various loading schemes provide an increasing amount of information concerning the anisotropic behavior of

the material.

An additional consideration of performing this type of experiment is to improve the accuracy of numerical simulations to match appropriate experimental results. Standard characterization methods for quantifying the descriptive parameters of the material used in a numerical simulation (ASTM Standard F2004, 2010) (ASTM Standard F2005, 2005) (ASTM Standard F2082, 2006) consider a limited range of material behavior especially geared toward the medical industry, and more information about the material is required for numerical simulation performed for SMA structures (Meraghni et al., 2013). According to Avril et al. (2008), increasing the complexity of experimentation allows for identification of additional material parameters which may describe anisotropic material behavior, or phenomena occurring due to inhomogeneity in the material specimen. Furthermore, more complex experiments such as with non-uniform specime geometry allow for more information to be gathered from a fewer number of tests, and with increased reliability. Meraghni et al. (2013) demonstrated that in addition to uniaxial deformation properties, an increased complexity from wire to dogbone geometry also allows identification of transverse deformation properties.

3.1.1 A review of the previous work

As a precursor to the current experimental study, a detailed review of Meraghni et al. (2013) is presented at this point. Tests were performed on three different dogbone specimens which were loaded in tension, and the strain fields were measured using 2D-DIC (see Section 1 for a review of the DIC method). The goal of these experiments was to demonstrate the axial and transverse material response to loading in pure uniaxial tension. It should be noted that a key feature of DIC is that full-field strain measurement may be obtained for both axial and transverse

deformation, and one-to-one comparison of axial-to-transverse strain data may be obtained at many (hundreds, thousands) of points across the specimen. According to the problem outlined for this series of studies, one experiment was necessary to show the axial/transverse strain behavior of the material for characterization, and two experiments were necessary to perform the desired material model parameter calibration. Specifically, definition of a phase diagram is desired, as well as a quantification of the elastic response of the material. Construction of the phase diagram requires knowledge of the temperature-stress dependence of the material response, therefore two isothermal experiments were required. A third experiment was also performed for validation of the calibration procedure.

The focus of the work was to calibrate a constitutive model by direct comparison of the displacement fields obtained by FEA simulation and DIC experimental measurement. This comparison is carried out by minimization of a cost function, as (Meraghni et al., 2013)

$$C\left(p\right)=\frac{1}{2}\left(\boldsymbol{\varepsilon}\left(\mathbf{p}\right)^{num}-\boldsymbol{\varepsilon}^{exp}\right)^{T}\mathbf{W}\left(\boldsymbol{\varepsilon}\left(\mathbf{p}\right)^{num}-\boldsymbol{\varepsilon}^{exp}\right), \tag{3.1}$$

where $\boldsymbol{\varepsilon}^{num}$ and $\boldsymbol{\varepsilon}^{exp}$ are the planar strain components for the experiment ($\boldsymbol{\varepsilon}^{exp}$) and FEA numerical simulation ($\boldsymbol{\varepsilon}\left(\mathbf{p}\right)^{num}$) and $\mathbf{W}$ is a weighting factor matrix. The material model parameters include the elastic modulus, E, Poisson's ratio, ν, transformation hardening parameter, H_f, transformation strain magnitude in the direction of transformation, ε_{SAT}^{T}, transformation surface slope for forward and reverse transformation, b_f and b_r, martensite start temperature at zero stress, M_s, and austenite finish temperature at zero stress, A_f. Thus $\mathbf{p}$ is written as (Meraghni et al., 2013)

$$\mathbf{p}=\left\{E,\nu,H_f,\varepsilon_{SAT}^{T},b_f,b_r,M_s,A_f\right\}. \tag{3.2}$$

These values were updated in the optimization in a standard Gauss-Newton sense by calculation of the Jacobian matrix, or sensitivity matrix, for an updating algorithm. In this unique problem, the most interesting result is that for the SMA material, both axial as well as transverse transformation behavior were both measured in the experiment. Meraghni et al. (2013) provides both an FEA prediction as well as a calibrated FEA result of the axial/transverse strain response of the uniaxially loaded specimen together with the experimental result. Good agreement is shown between the FEA and DIC results.

The specimens tested were dogbone shaped specimens cut from NiTi (50.6 at.% Ni) by waterjet hyperbaric machining; the sample was fully annealed (water quenched after 30 minutes at 673 K). The specimens which were used had a 30 mm gage section with a cross-section of 2.5x10.0 mm. The specimens were tested at two different temperatures (323 K, 343 K); an additional test at 333 K was performed for experimental validation of the identification procedure.

3.1.2 Review of characterization process

An experimental process was devised by researchers at Arts et Métiers ParisTech to obtain a full description of the anisotropic mechanical behavior of equiatomic NiTi material under various loads. Experiments have been performed in increasing complexity in order to demonstrate material response to various loading schemes. This plan may be represented by the schematic shown in Figure 3.1 which shows an example yield/transformation surface in the $\sigma_{11} - \sigma_{22}$ stress space for an anisotropic material.

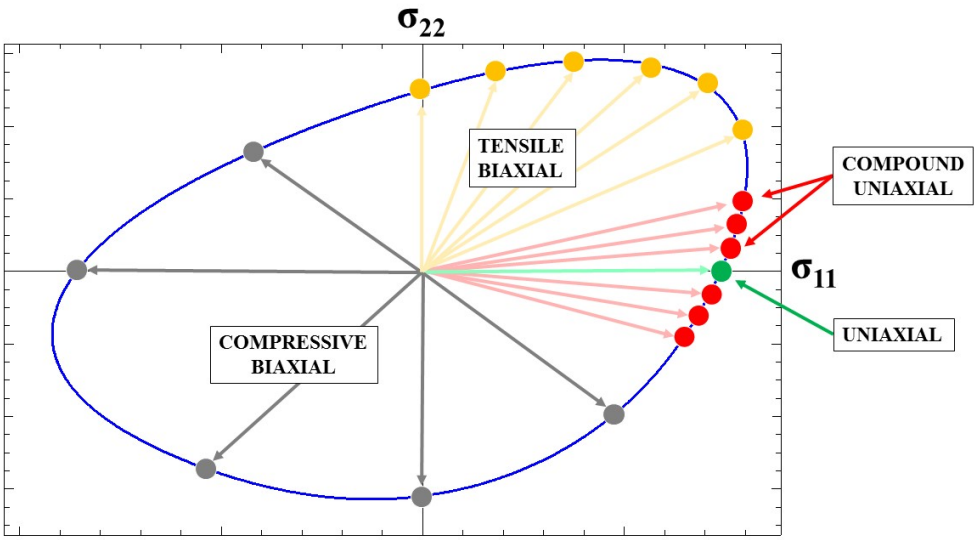

Figure 3.1: Example yield/transformation surface of SMA material, demonstrating the need for multi-axial loading schemes (Chimisky et al., 2013).

In the first set of experiments in this experimental process, uniaxial loading was considered via testing of dogbone specimens, which was the work performed by Meraghni et al. (2013). These experiments demonstrated the material response to uniaxial loading in tension, or along the "σ_{11}" axis in Figure 3.1. Note that the surface of Figure 3.1 may represent material yielding when fully martensite or fully austenite, or may also represent any of the four transformation surfaces of the material (c.f. D. Lagoudas (2008), Section 3). The tests referred to here serve to primarily demonstrate the material response to a multi-axial stress state, and not to necessarily define the yield/transformation surfaces. After testing of dogbone specimens, further experiments (described in this section) use specimens with a non-uniform shape in order to introduce multi-dimensionality in the loading scheme of the material. Specifically, in addition to uniaxial stresses, shear stresses have also been introduced

by this experiment. With reference again to Figure 3.1, the distribution of stress in this experiment occurs differently at different regions in the specimen and may behave both along the "σ_{11}'' axis as well along the "σ_{12}'' axis and "σ_{22}'' axis. (the "σ_{12}'' axis is not shown in Figure 3.1). In the third and final step of this series, cruxiform specimens will be used to demonstrate the material response to biaxial loading, which considers simultaneous loads along both the "σ_{11}'' and "σ_{22}'' axes in Figure 3.1. The remainder of the σ_{11}-σ_{22} space may be considered by performing compression testing (uniaxial and biaxial) of the material.

At this point it is necessary to show the importance of appropriate experimental measurement techniques which give the most possible data from the experiments. In order to obtain reliable information from the second and third experimental techniques mentioned in the previous paragraph, full-field strain measurement is vitally necessary. In fact, digital image correlation (DIC) was utilized not only for these two experiments, but also for the first. In addition to measuring response of the material for inhomogeneous loading, the use of DIC boasts another advantage. Calibration of material model parameters may be performed by careful inverse analysis of the experiment by FEA modeling of the experiment.

The experimental studies here are performed with an additional goal of improving the numerical model used to simulate the SMA material. The narrative which follows explains the experimental approach taken, and gives an analysis of the experimental methods used. Furthermore, a detailed analysis of the experimental results will be included.

3.2 Experimentatal characterization of SMAs using non-uniform specimen geometry

The work of Meraghni et al. (2013) is complimented by the experiments demonstrated in this section. The loading scheme was expanded from simple uniaxial to so called "compound uniaxial'' loading, that is, uniaxial loading in which the stresses within the specimen are more than uniaxial due to the unique configuration of the specimen. The heterogenous specimen shape was derived from Meuwissen, Oomens, Baaijens, Petterson, and Janssen (1998) and hence the specimen shape has adopted the name of Meuwissen. The exact specimen geometry is shown in Figure 3.2.

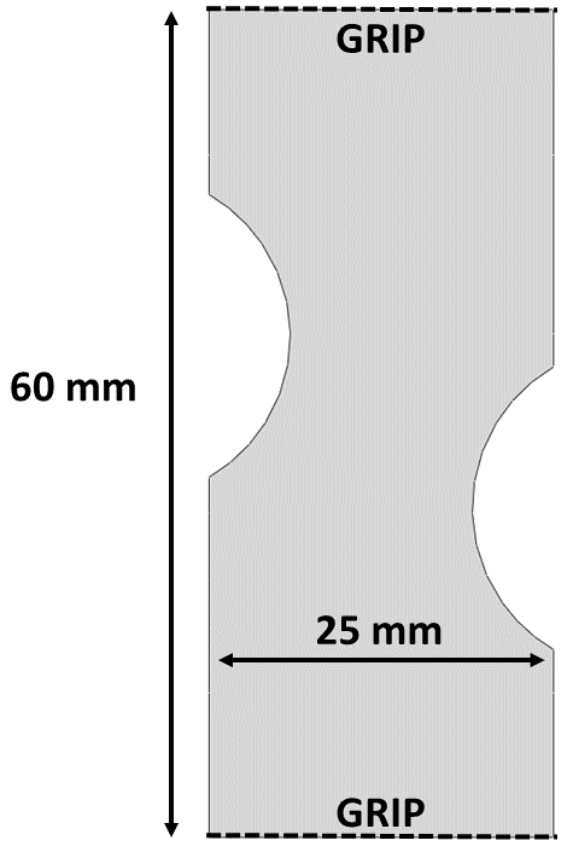

Figure 3.2: Meuwissen shaped specimen geometry (Chimisky et al., 2013).

In addition to demontstrating the transverse behavior of the SMA material during tensile testing of the material (Meraghni et al., 2013), using a non-uniform geometry specimen may also provide information regarding the anisotropic response of SMA material. Studies in the past have shown that anisotropies exist in the material with respect to loading direction (Orgéas & Favier, 1998),(Gall et al., 2001), (Frick, Ortega, Tyber, Gall, & Maier, 2004). Frick et al. (2004) particularly demonstrated that the anisotropy in material behavior is due to martensitic deformation mechanisms present in tension versus compression, especially when the material is near the transformation temperatures. Therefore, it is beneficial to to be able to calibrate numerical simulation models using data obtained by loading of the material along multiple axes simultaneously, and such a loading scheme would predict structural implementation of the SMA material more accurately.

The experiments were performed at three different isothermal temperatures. More than one experiment were performed for validation of the calibration procedure, but were not necessary for the calibration. In fact, the complete characterization attainable from the Meuwissen specimen may be reached by testing only one specimen. As outlined by the previous section, the parameters being calibrated include E and ν as the elastic properties, b_f, b_r, A_f and M_s as the phase diagram parameters and H_f and ε_{SAT}^{T} as the transformation behavioral parameters. For uniaxial loading of the specimen as was done previously by Meraghni et al. (2013), all of these parameters with the exception of two may be quantified by only a single uniaxial experiment. In that work, a second experiment is necessary only for quantifying the relationship between stress and temperature in the phase diagram that is the b_f and b_r terms. The third test was performed for experimental validation. For the Meuwissen experiments, however, the second experiment is not necessary. Due to the heterogeneity of the specimen geometry, different regions experienced different stress states, therefore

the stress - temperature relationship of the phase diagram may be identified by a single experiment. The second and third experiments at different temperatures serve as experimental validation of the results.

3.2.1 Specimen preparation

Experiments were performed on SMA specimens with composition NiTi (50.6 at. % Ni). The material was annealed at 673 K for 30 minutes and water quenched. Six specimens were cut by Nimesis Technology into the Meuwissen shape (Meuwissen et al., 1998), which was utilized in order to capture the most diverse displacement field possible for a tension test with a thin specimen.

A picture of the specimens is shown in Figure 3.3 (Post-testing). Each specimen was prepared for digital image correlation by painting a black speckle pattern on a white background. A flat white spray paint was applied to the specimens, followed by a layer of black acrylic paint applied by airbrushing.

3.2.2 Testing procedure

The experimental process included a total of six experiments. Two experiments were performed at three different temperatures: 323 K, 333 K, and 343 K. The first experiment at each temperature preceded the second as a prediction of the material response to applied load, which was necessary due to the unknown distribution of stresses in the specimens. For the second experiment at each temperature, both loading and unloading were desired to obtain reverse transformation data. However, yielding was undesirable for these experiments. In order to achieve most possible data from these experiments, it was necessary to determine the exact load at which yielding occurred at any point in the specimen for each of the three temperatures. Through DIC measurement, the axial, transverse, and shear strain at every location on the specimen may be determined. Through analysis at the DIC data (an algorithm

was written to determine the location and the corresponding load for the maximum value of the axial strain) the applied load at which the onset of yielding occurred could be determined. It was assumed based on previous experiments for the material that yielding due to a uniaxial load will occur when the strain in the specimen in the direction of the uniaxial load (axial strain) achieved a value of 6% axial strain. Hence at each temperature, the first specimen was loaded until catastrophic failure, and in post analysis the load at which the maximum axial strain achieved was 6% axial strain was determined. The second specimen at each temperature was loaded up to that determined critical applied load, and unloaded. Table 3.1 shows the test matrix for this experimental process. The specimens after each experiment were photographed and are shown in Figure 3.3. For each of the six experiments, the temperature chamber was heated by PID control until the temperature of the grips at the location of the specimen grip interface achieved stability and the desired temperature, and the ambient temperature of the air inside the chamber was at the same temperature. These temperatures were measured by a thermocouple attached to the grip near the specimen and a thermocouple hanging freely inside the chamber. The tests were performed with a hydraulic test stand. Also for each test, stroke control was utilized due to the non-linear behavior of the material during transformation.

Test Number	Temperature (K)	Load
1'	323	Failure
1	323	22.6 kN
2'	333	Failure
2	333	24.7 kN
3'	343	Failure
3	343	26.7 kN

Table 3.1: Testing matrix for the characterization experiments.

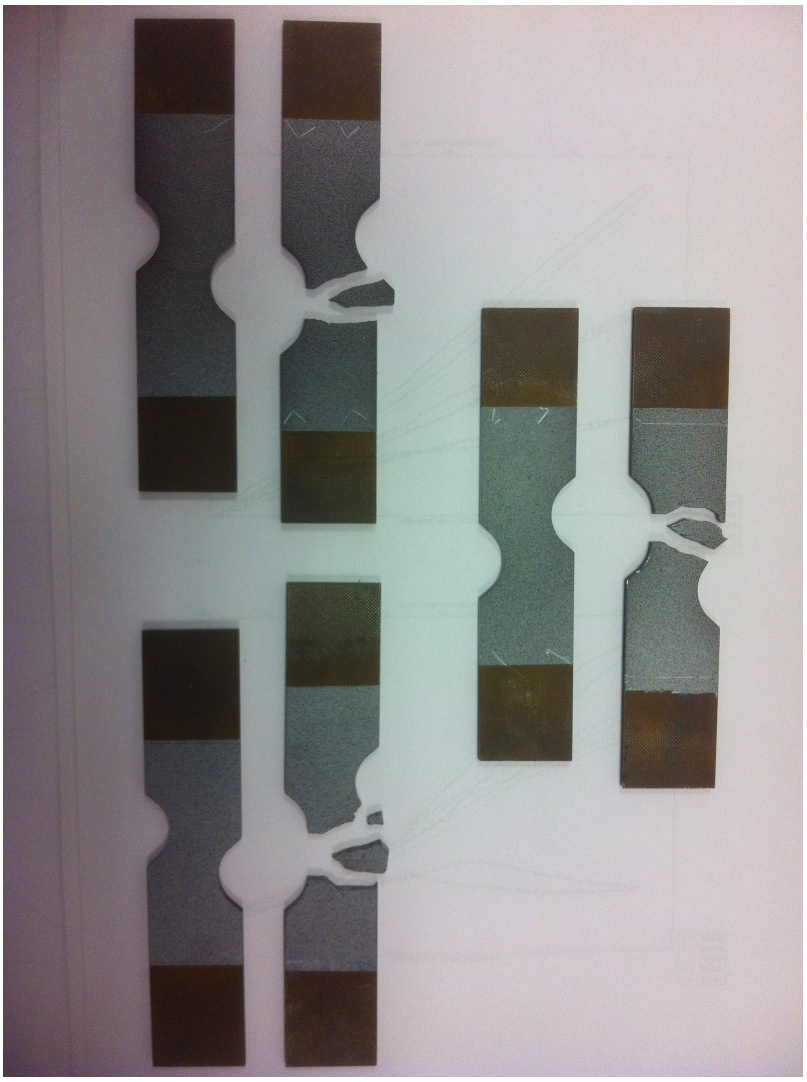

Figure 3.3: Specimens used for experimental characterization using the Meuwissen geometry.

2D-DIC (c.f. Section 1) measurements was performed through the window of the temperature chamber. Several considerations were necessary for this particular application of 2D - DIC. First, performing DIC measurement through the window of a temperature chamber introduces several possibilities of experimental error which must be either attended or to quantified, or both. Lighting becomes an issue; if the

light source is placed outside of the chamber, there may be problems due to reflections of the light on the surface of the window. Ideally, the light source should be places inside the temperature chamber, but this is many times not feasible due to limited space, or a temperature that is too high and may damage the light source. For these experiments, the light source was able to be placed inside the chamber thus mitigating this particular issue. However other reflections may be present from outside sources of light. For DIC measurements through a window, therefore a dark room is preferred such that reflections become and issue because they introduce changes in the gray value distributions of the subsets which would not otherwise be present, which may be interpreted by the optimization algorithm as either inaccurate displacement or in extreme cases as a region with no solution. This is the same reasoning that is used for the requirements for and opaque specimen surface in specimen processing. See Section 1 for more details. Yet another factor of the temperature chamber window is that the requirement for perpendicularity between the specimen and the camera line of the sight becomes amplified because of the introduction of the second and the third medium which are the window at the temperature chamber and the changed environment (temperature, humidity, pressure) inside the temperature chamber. In fact, it is key that the specimen be parallel to the chamber window, and the camera line of the sight mutually perpendicular to the chamber window and the specimen. Any variation from this perpendicularity will cause inaccurate deformation measurements by distortions caused by the reflection of the light when passing through the three medium. For the Meuwissen specimen experiments, the temperature chamber was oriented to the test stand such that the window was parallel to the orientation of the stand; the grips were attached similarly paying close attention to the orientation to the test stand. The CCD camera was placed on a tripod at a low height. The tripod was adjusted such that the CCD camera was level (with respect

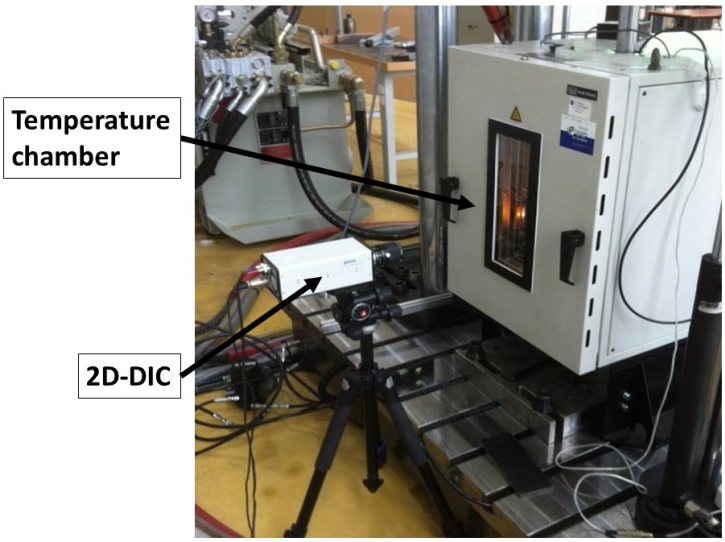

Figure 3.4: Test setup, showing the hydraulic test stand, CCD camera for DIC, and temperature chamber.

to gravity) and perpendicular to the window of the temperature chamber. Other issues with performing 2D-DIC through the chamber window include both noise and resolution, which are both factors of placing the CCD further from the specimen surface them would otherwise be necessary. The camera should be placed as close to the specimen as possible in order to mitigate these particular issues. Figure 3.4 shows a photograph of the setup for this experiment.

Figure 3.5 shows the loading path taken for each of the three specimens at the various temperatures. The load is plotted for each specimen against a time element represented by the tens of DIC images captured, denoted here as "interval number''. Specimen 1 was tested at 323 K and loaded up to 23 kN, which was the load at which the maximum axial strain achieved was 6 %. For the same critical load criterion, Specimen 2 was tested at 333 K and achieved a maximum load of 25 kN. Similarly, Specimen 3 tested at 343 K achieved a maximum load of 26.5 kN.

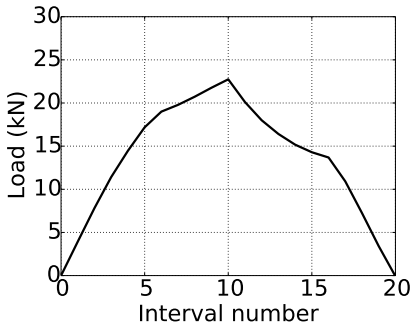

(a) Load cycle for specimen tested at 323 K.

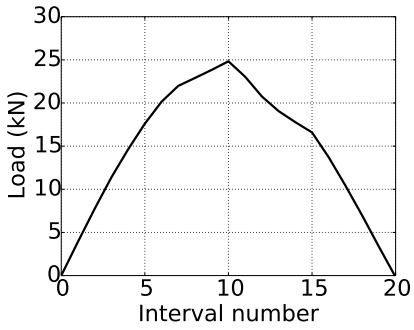

(b) Load cycle for specimen tested at 333 K.

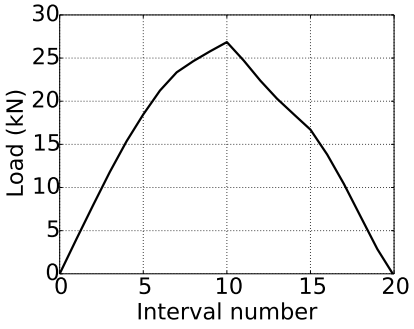

(c) Load cycle for specimen tested at 343 K.

Figure 3.5: Loading history for specimens 1-3. The interval number is in terms of tens of images taken in the sense of a constant interval image capture rate of 0.25 Hz.

3.3 Constitutive model calibration

It should be noted again at this point that the maximum load achieved does not reflect the stress state in the specimen which is highly variable. Hence a stress-strain analysis cannot be drawn from these data, and careful calibration is necessary by inversely comparing the experimental displacement field result to the FEA simulation with approximated material model parameter values, and updating the parameter values based on the correlation between these results.

3.3.1 Review of the constitutive model parameter calibration algorithm

In a manner similar as outlined by Equation (3.1) a cost function based analysis is used here to update approximated "guessed'' values of the material model parameters shown in Equation (3.2). As motivation for this process, it is noted here that upon successful calibration of the descriptive material parameters, the behavior of the material due to the heterogeneous stress field that is characteristic of the Meuwissen shape may be assessed, and in particular data points may be obtained for the anisotropic variations along the σ_{11}-σ_{22} transformation surfaces (c.f. Figure 3.1). Equation (3.2)is reproduced here. The material parameters vector is represented by: (Meraghni et al., 2013)

$$p = \left\{ E, \nu, H_f, \varepsilon_{SAT}^T, b_f, b_r, M_s, A_f \right\}. \tag{3.3}$$

The experimental results are represented by the constant temperature state, T, and the two-dimensional form of the strain tensor, i.e., total strain denoted as

$$\boldsymbol{\varepsilon} = \begin{bmatrix} \varepsilon_{11} \\ \varepsilon_{22} \\ \varepsilon_{12} \end{bmatrix}; \tag{3.4}$$

these data are obtained at every location on the surface of the specimen at many (hundreds, thousands) of points. For SMAs, the total strain (same as what is measured by DIC) is commonly additively decomposed as (D. Lagoudas et al., 2012)

$$\boldsymbol{\varepsilon} = \boldsymbol{\varepsilon}^{el} + \boldsymbol{\varepsilon}^{th} + \boldsymbol{\varepsilon}^{T} \tag{3.5}$$

where $\boldsymbol{\varepsilon}^{el}$ is the elastic component, $\boldsymbol{\varepsilon}^{th}$ is the thermal component, and $\boldsymbol{\varepsilon}^{T}$ represents

the highly inelastic strains present due to phase transformation characteristic of SMAs. Rewriting each term of Equation (3.5) in terms of its respective contributing factors gives the equation

$$\boldsymbol{\varepsilon} = \mathbf{S} : \boldsymbol{\sigma} + \boldsymbol{\alpha}(T - T_{ref}) + f\bar{\boldsymbol{\varepsilon}}^T. \tag{3.6}$$

The elastic strain has been written as the widely accepted constitutive relation. The thermal component has been written according to the coefficient of thermal expansion material property, and for the isothermal experiment, has no contribution. $\boldsymbol{\varepsilon}^T = \varepsilon^T_{SAT}$ (in a 1-D sense) is the transformation strain achieved when the material is fully martensite, hence the contribution of the inelastic transformation strain may be represented in a linear sense as the maximum achievable transformation strain, ε^T_{SAT}, multiplied by a factor of zero to unity representing the current transformation state of the martensite volume fraction of the material, and is unity at martensite.

The forces which drive the transformation phenomenon to occur may be modeled from several standpoints (c.f. Section 1). For the model considered here, as well as that reviewed in Section 1, the driving forces are derived from a Gibbs free energy. The derivation included in Meraghni et al. (2013) is not shown here, but results in the identification of the several transformation parameters which were set forth by Equation (3.3). Concerning these parameters in particular, notice: M_s and A_f are transformation criterion at no load, which are determined experimentally. Commonly, differential scanning calorimetry (DSC) is used to determine these parameters. Alternatively, they are characteristic of the phase diagram and are deduced together with the transformation slopes, b_f and b_r. The transformation hardening parameter is written as

$$H_f = \varepsilon_{SAT}^T b_f \left(M_s - M_f\right) = \varepsilon_{SAT}^T b_r \left(A_f - A_s\right) \tag{3.7}$$

for which the choice of form to be used depends on the transformation direction.

At this point our focus will shift for the definition of the material constitutive model to a review of the genetic algorithm used for updating the identifying parameters. A cost function is defined in the squared difference sense as

$$\begin{aligned} C(p) = & \frac{1}{2} \frac{\sum_{t=t_1}^{t^R} \sum_{j=1}^{n} \left(\varepsilon_{11}\left(\mathbf{p}, \mathbf{t}, \mathbf{x}_j\right)^{num} - \varepsilon_{11}\left(\mathbf{t}, \mathbf{x}_j\right)^{exp}\right)^2}{\sum_{t=t_1}^{t^R} \sum_{j=1}^{n} \left(\varepsilon_{11}\left(\mathbf{t}, \mathbf{x}_j\right)^{exp}\right)^2} + \\ & + \frac{1}{2} \frac{\sum_{t=t_1}^{t^R} \sum_{j=1}^{n} \left(\varepsilon_{22}\left(\mathbf{p}, \mathbf{t}, \mathbf{x}_j\right)^{num} - \varepsilon_{22}\left(\mathbf{t}, \mathbf{x}_j\right)^{exp}\right)^2}{\sum_{t=t_1}^{t^R} \sum_{j=1}^{n} \left(\varepsilon_{22}\left(\mathbf{t}, \mathbf{x}_j\right)^{exp}\right)^2} + \\ & + \frac{\sum_{t=t_1}^{t^R} \sum_{j=1}^{n} \left(\varepsilon_{12}\left(\mathbf{p}, \mathbf{t}, \mathbf{x}_j\right)^{num} - \varepsilon_{12}\left(\mathbf{t}, \mathbf{x}_j\right)^{exp}\right)^2}{\sum_{t=t_1}^{t^R} \sum_{j=1}^{n} \left(\varepsilon_{12}\left(\mathbf{t}, \mathbf{x}_j\right)^{exp}\right)^2} + \\ & + \frac{1}{2} \frac{\sum_{t=t_1}^{t^R} \left(F\left(\mathbf{p}, \mathbf{t}\right)^{num} - F\left(\mathbf{t}\right)^{exp}\right)^2}{\sum_{t=t_1}^{t^R} \left(F\left(\mathbf{t}\right)^{exp}\right)^2} \end{aligned} \tag{3.8}$$

whose evolution is minimized to converge on the solution for the optimal parameteric values. In that equation, t^R denotes the number of DIC images captured (note that each image was taken on a constant time interval), n represents the number of data points being analyzed, x_j is the position on the specimen of the point being analyzed, and F is the applied force at the specimen boundary. ε^{num} and ε^{exp} are the FEA and DIC strain values, respectively. This cost function receives the DIC measurements as

well as the updated subroutine approximated parameter values. It is then determined whether this cost function satisfies a convergence criterion, and if not, a sensitivity analysis is performed by calculation of the Jacobian as (Meraghni et al., 2013)

$$\boldsymbol{S} = \frac{\partial \boldsymbol{\varepsilon}(\mathbf{p})^{num}}{\partial \mathbf{p}} \tag{3.9}$$

which creates an update Δp. The current vales are updated as (Meraghni et al., 2013)

$$\mathbf{p}^{i+1} = \mathbf{p}^{i} + \boldsymbol{\Delta}\mathbf{p}. \tag{3.10}$$

This version of the Levenburg-Marquardt algorithm boasts a unique sensitivity analysis which is detailed in Meraghni et al. (2013), and has a high convergence rate and speed.

3.3.2 Review of experimental data interpolation and grid shifting

In order to perform optimization of the parameter values, there must be one-to-one correspondence between the experimental and numberical strain results. Such correspondence requires the location of the analysis point to be at exactly the same relative location on the specimen surface as the experimental data. Ideally, the experimental results would not shift or be interpolated, however, this was chosen for interpolation over the simulation points, because the simulation points are being updated to match the experimental data; also, the simulation points locations are stationary between the experimental studies while the DIC grid changes between each experiment. Hence it is better to interpolate the experimental data. Furthermore, the DIC results grid was scaled, shifted, and rotated such that it overlaid to match the dimensions of the simulation grid. The center point of the elements on a surface

of the specimen were chosen as the points of interest for the FEA simulation.

3.4 Results

3.4.1 Experimental strain results

The DIC strain measurement results are presented in Figures 3.6, 3.7, and 3.8 for Specimens 1, 2, and 3 respectively. For each specimen, the axial (ε_y), transverse (ε_x), and shear (ε_{xy}) strain are plotted in each respective subfigure. The seven frames in each subfigure represent the time steps in the progression of the experiment. In each subfigure, the fourth frame represents the time step of highest load, and loading/unloading occurs on either side of that step.

The resolution of the DIC measurement performed for Specimen 1 was 0.0758 mm per pixel; however, the results reported in Figure 3.6 have a resolution of 0.758 mm per reported data point. Similarly, the resolution for Specimens 2 and 3 are 0.0694 mm per pixel. The resolution of the reported results in Figures 3.7 and 3.8 are 0.694 mm per reported data point.

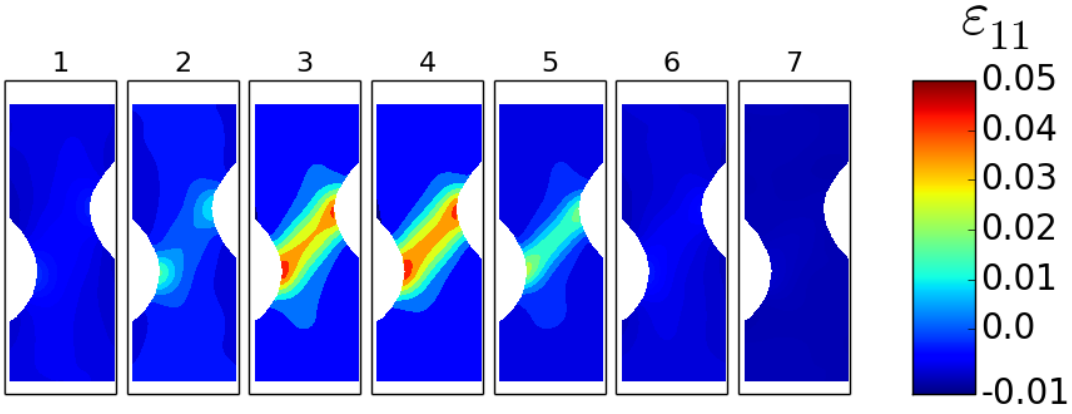

(a) Axial strain, ε_{11}

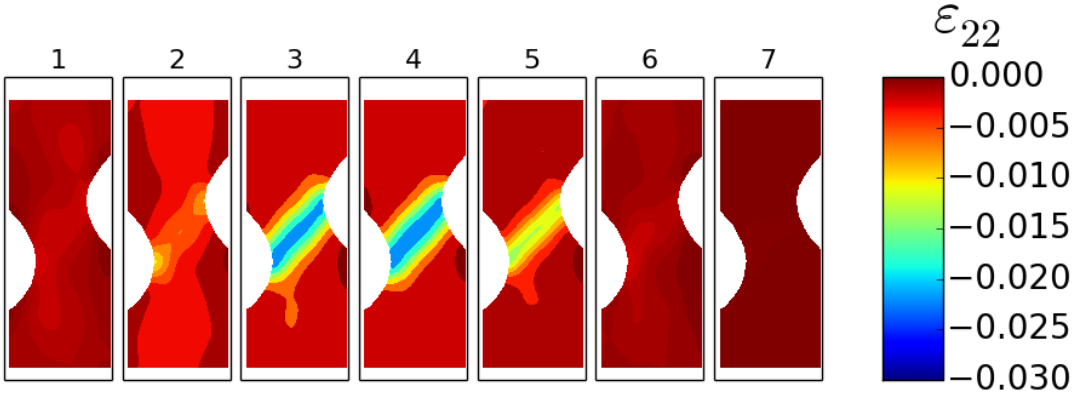

(b) Transverse strain, ε_{22}

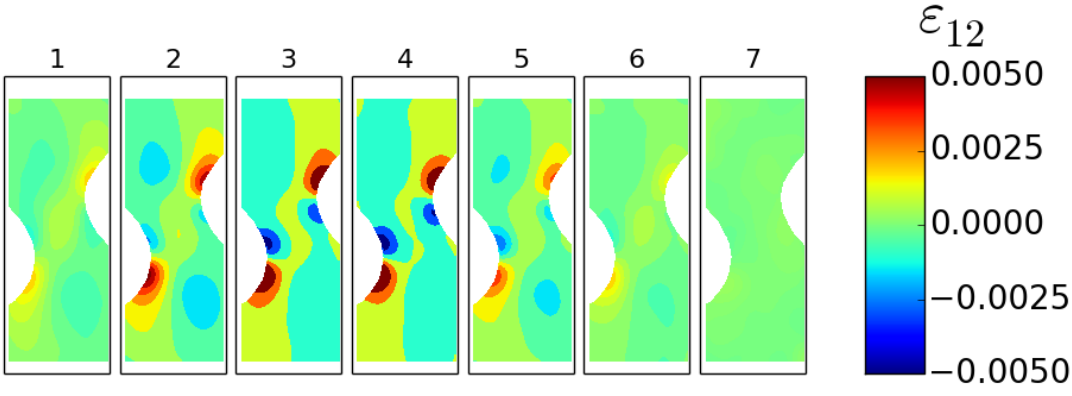

(c) Shear strain, $2 \cdot \varepsilon_{12} = \gamma_{12}$

Figure 3.6: Axial, transverse and shear strain fields for Meuwissen specimen tested at 50 °C.

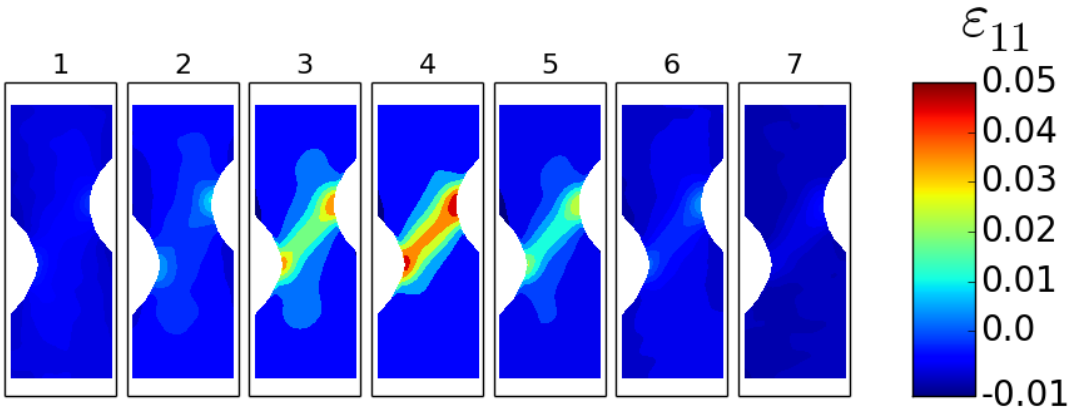

(a) Axial strain, ε_{11}

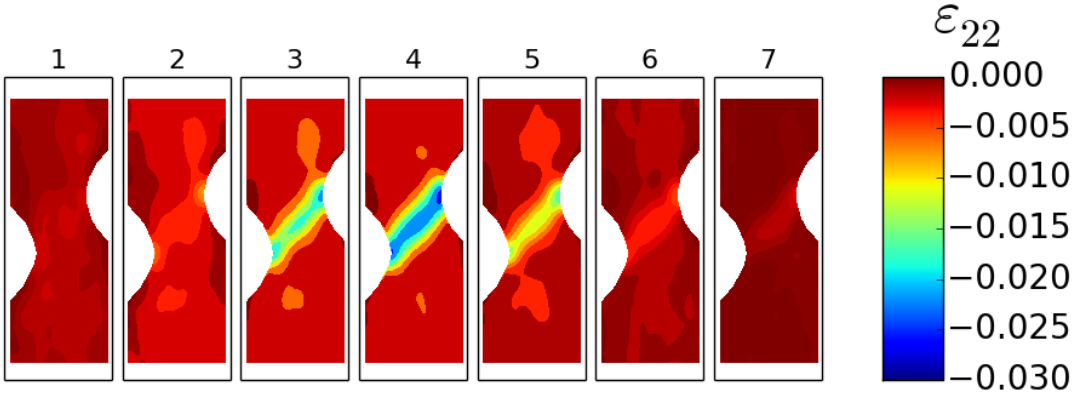

(b) Transverse strain, ε_{22}

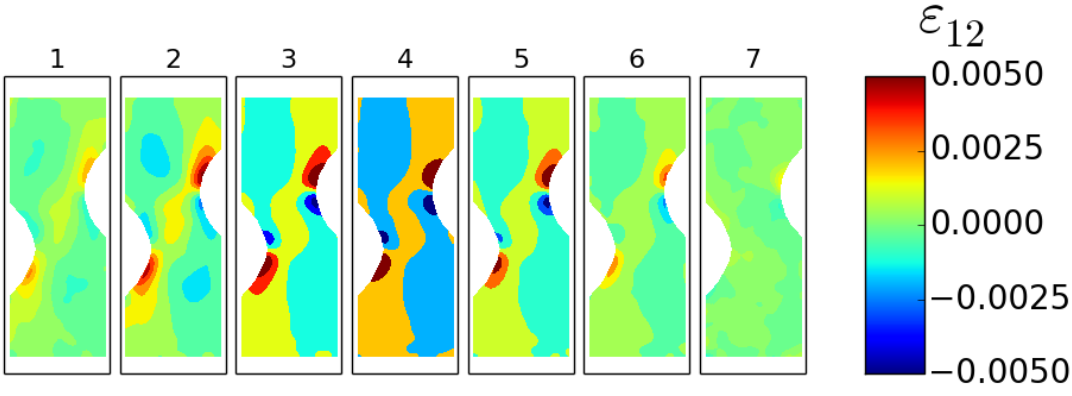

(c) Shear strain, $2 \cdot \varepsilon_{12} = \gamma_{12}$

Figure 3.7: Axial, transverse and shear strain fields for Meuwissen specimen tested at 60 °C.

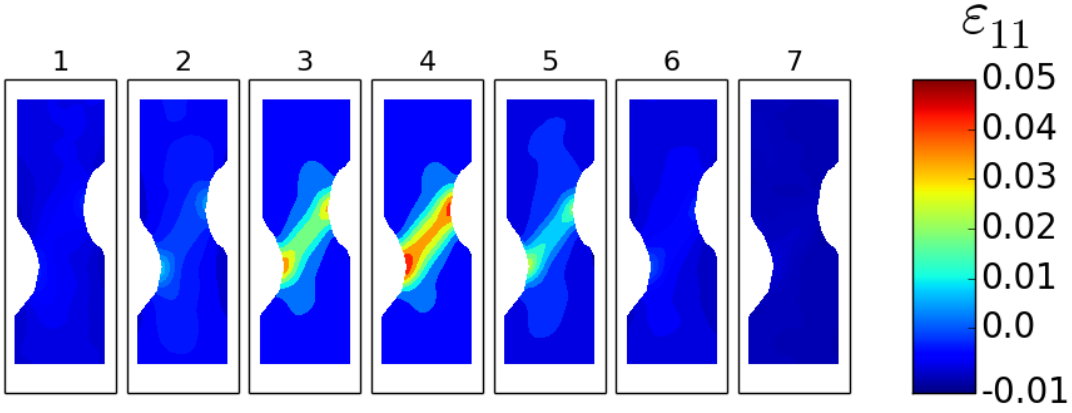

(a) Axial strain, ε_{11}

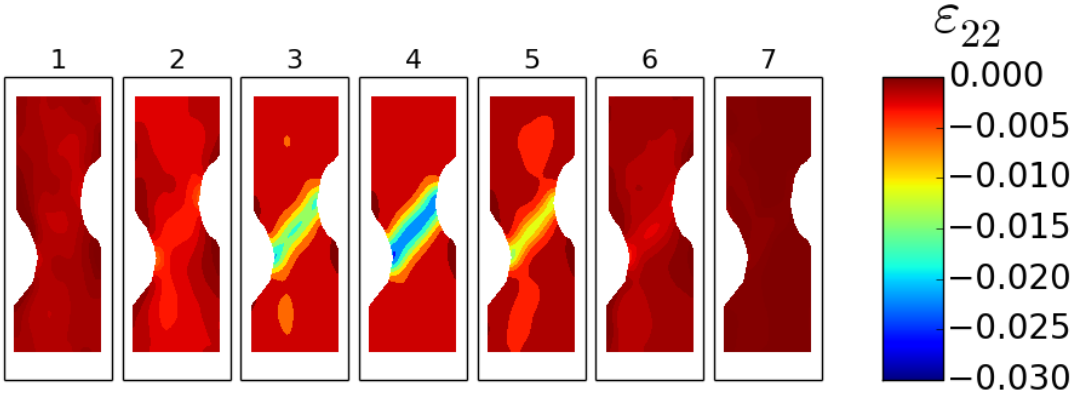

(b) Transverse strain, ε_{22}

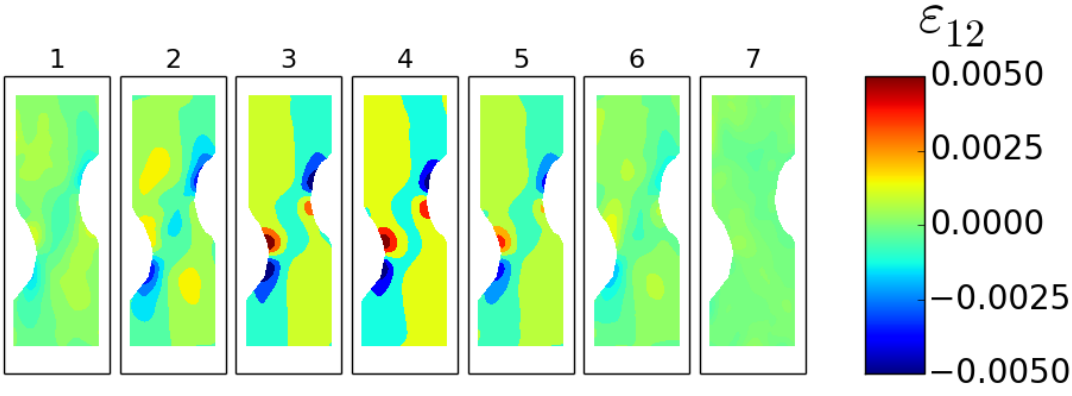

(c) Shear strain, $2 \cdot \varepsilon_{12} = \gamma_{12}$

Figure 3.8: Axial, transverse and shear strain fields for Meuwissen specimen tested at 70 °C.

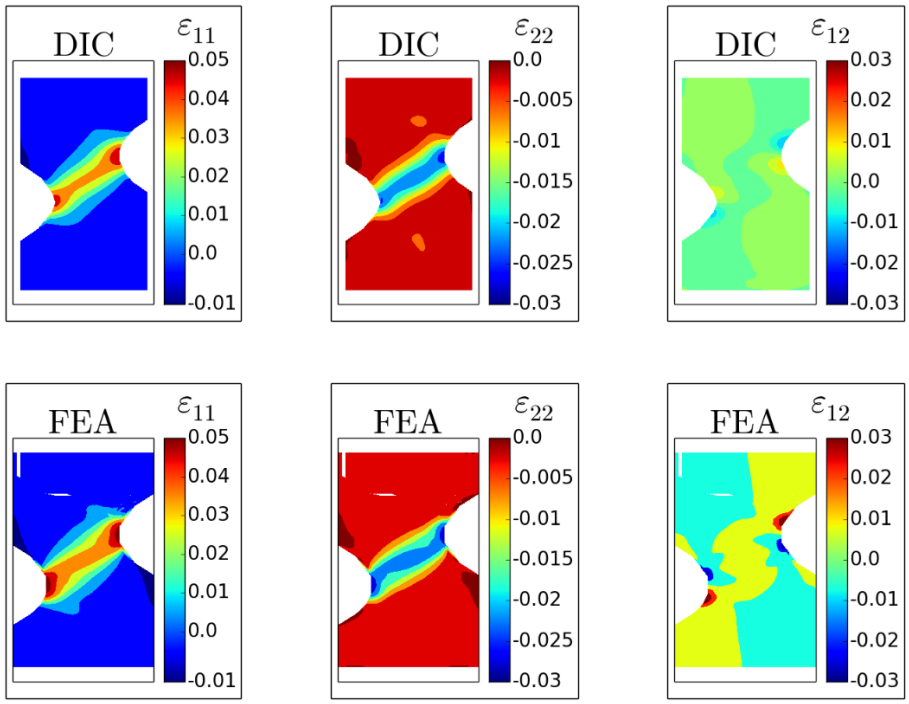

Figure 3.9: A comparison of the strain fields calculated via FEA after calibration of the constitutive model parameters and the experimental results for Specimen 2 tested at T=333 K.

3.4.2 Model calibration results

It should be re-emphasized at this point that characteriation of the material for its behavior under multi-axial loading requires the knowledge of the stress state occurring within the specimen. Hence, the material constitutive model utilized by the FEA simulation was calibrated to match the experimental results. The results of the material model parameter optimization are best seen in Figures 3.9, and 3.10 which show the DIC and FEA strain results for the specimens tested at 60 °C and 70 °C, respectively.

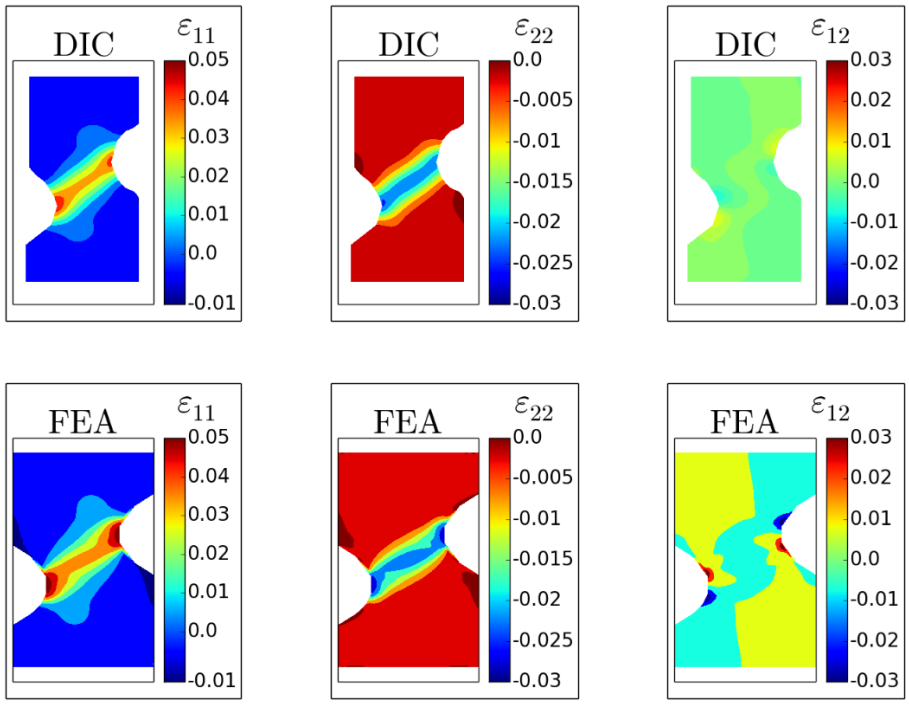

Figure 3.10: A comparison of the strain fields calculated via FEA after calibration of the constitutive model parameters and the experimental results for Specimen 3 tested at T=343 K.

From this figure, it may be seen that there is very good agreement between the FEA simulation with optimized material model parameters and the DIC strain measurements. Recall that the other two experiments were performed especially for experimental validation. The calibrated parameters are shown in Table 3.2.

Parameter	*Value*
E (MPa)	67,538
ν	0.349
H_f (MPa)	1.85
ε^T_{SAT} (%)	4.18
b_f (MPa/K)	8.54
b_r (MPa/K)	10.68
M_s (K)	257
A_f (K)	283.1

Table 3.2: Calibrated material model parameters (Chimisky et al., 2013).

3.4.3 Characterization results

The behavior of the material due to uniaxial loading was outlined previously by Meraghni et al. (2013). In that work, the behavior of axial and transverse strain in the material with an increase in uniaxial stress was shown. The behavior of NiTi is expected to be anisotropic, thus the stress states along different axes are of different magnitudes. The Meuwissen shape introduces shear loading and transverse loading to the specimen at certain locations on the specimen. Therefore, the benefit of the Meuwissen specimen is two-fold: first that calibration of the model parameters may be performed by only one experiment, and secondly that anisotropic behavior of the material is demonstrated. (c.f. Figure 3.1). The complex planar stress field made possible by the Meuwissen specimen shape is represented by the 2D stress tensor as

$$\boldsymbol{\sigma}_{MW} = \begin{bmatrix} \sigma_{11} & \sigma 12 & 0 \\ \sigma 12 & \sigma 22 & 0 \\ 0 & 0 & 0 \end{bmatrix}. \tag{3.11}$$

This tensor represents all possible non-zero stress terms anywhere in the specimen. In comparison, the simple uniaxial loading scheme may be represented as

$$\boldsymbol{\sigma}_{U} = \begin{bmatrix} \sigma_{11} & 0 & 0 \\ 0 & 0 & 0 \\ 0 & 0 & 0 \end{bmatrix}, \tag{3.12}$$

because it is assumed that only σ_{11} is present anywhere in the gage section of the specimen at any time. Similarly, the idealized biaxial loading stress state is

$$\boldsymbol{\sigma}_B = \begin{bmatrix} \sigma_{11} & 0 & 0 \\ 0 & \sigma_{22} & 0 \\ 0 & 0 & 0 \end{bmatrix}. \tag{3.13}$$

In comparison of Equation (3.11) and Equation (3.13), the benefit of the Meuwissen specimen over the biaxial specimen is that not only are both σ_{11} and σ_{22} loads present, but also σ_{12} loads, so that representation of some subset of the $\sigma_{11} - \sigma_{22} - \sigma_{12}$stress space is possible, whereas biaxial loading only considers the $\sigma_{11} - \sigma_{22}$ space. Biaxial loading may consider many variations of σ_{11} vs σ_{22} (i.e., $\sigma_{11} > \sigma_{22}$, $\sigma_{11} < \sigma_{22}$, $\sigma_{11} = \sigma_{22}$, as well as compression variations), while the Meuwissen specimen can only consider the case of $\sigma_{11} \gg \sigma_{22}$. However, the many measurable regions on the Meuwissen specimen represent different variations of $\sigma_{11} - \sigma_{22}$ stress states (as well as σ_{12}) from a single experiment, while creating different variations of load paths for biaxial testing requires design of new experiments with new loading ratios. Furthermore, the Meuwissen test has a much smaller overall cost than the biaxial test, because for the Meuwissen specimen force may be applied using a common uniaxial load frame, while biaxial specimens require specialized and expensive testing hardware, as well as careful specimen design. Figure 3.11 shows the σ_{11}, σ_{22}, σ_{12}, and effective (in the mises sense) stress fields at the greatest applied load for the specimen tested at 343 K. Note that these stress fields were taken from the post-opitimization FEA simulation of the experiment.

Due to the uniaxial tension loading applied at the boundary for the Meuwissen specimen, the variation of loads between σ_{11}, σ_{22}, and σ_{12} for the Meuwissen specimen is highly disproportional. It is expected that the stress tensor of Equation (3.11) will be dominated by the axial stress term at every point on the specimen (with the exception of certain sharp convex locations near the cutouts where $\boldsymbol{\sigma}_{MW} \approx \mathbf{0}$:

see Figure 3.11). Referring to Figure 3.1, the data we expect to achieve in the $\sigma_{11} - \sigma_{22}$ stress space using the Meuwissen specimen are represented by the red loading directions. Different areas may provide either positive or negative shear stress, or positive or negative transverse loads in addition to positive uniaxial loads.

Figure 3.1 shows that to fully characterize the anisotropic material behavior in the plane, multiple loading schemes must be applied via tensile as well as compressive biaxial testing. However, some multi-dimensional loading may be represented by the

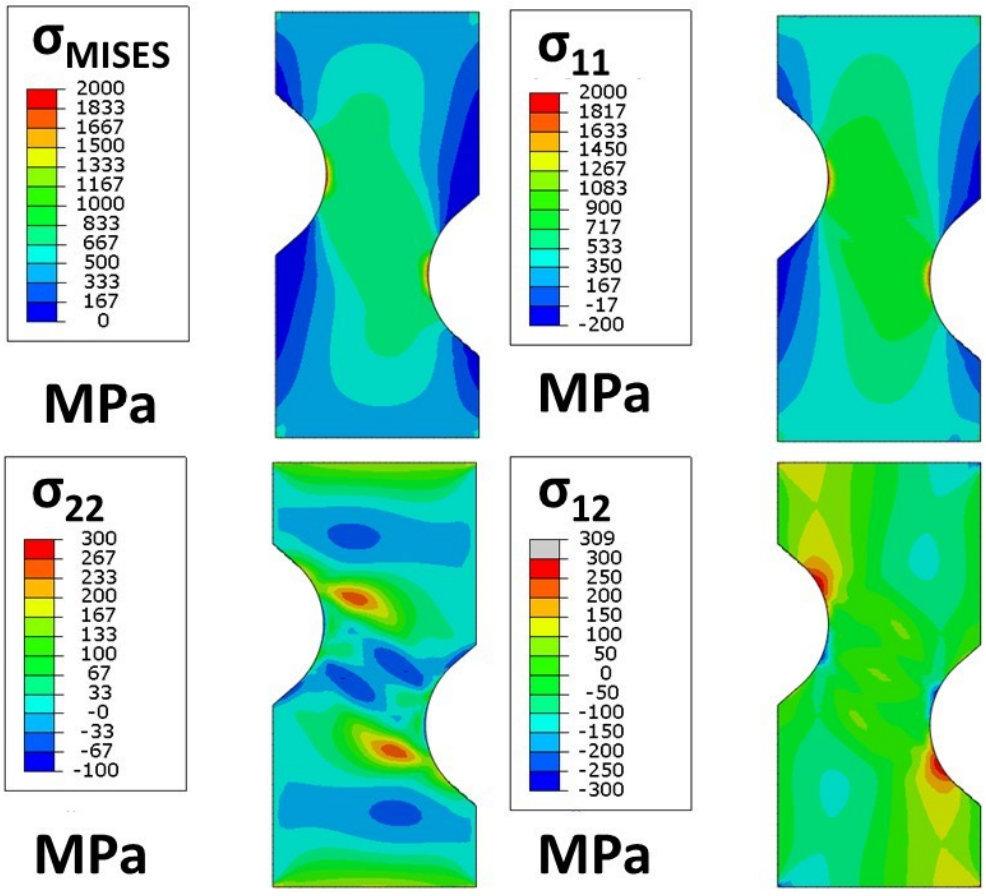

Figure 3.11: σ_{11}, σ_{22}, σ_{12}, and effective (Mises) stress fields at the greatest applied load for the specimen tested at 343 K. Note that these stress fields were taken from the iteratively calibrated FEA simulation of the experiment.

Meuwissen specimen tensile test. Figure 3.12 shows the stress state at many different locations on the specimen, at an example time step during the experiment at the beginning of the test. This time step was chosen because for elastic deformation (especially initial), the stress state in the specimen is scalable for each individual point, that is, the same figure with different load values represents the exact state of a future (but not inelastic) time step during the test. The results shown are dominated by the σ_{11} axial loads; however, significant transverse loads are also present.

The evolution of the load distribution in the specimen throughout the test for the $\sigma_{11} - \sigma_{12}$ space is represented in Figure 3.13. This figure shows the load evolution for the test, and the distribution of loads at many different points across the face of the specimen during each indicated time step. The numerical labels have been removed to show that the distribution of the load state is independent of scale, which is demonstrated by comparing the first frame, then the second frame which is at a higher applied load. Notice that during elastic loading/unloading, the load distribution remains constant. After phase transformation starts, the distribution changes, which is caused by the redistribution of loads after phase transformation begins. Note that the two axes are equal in value on each frame, but the values of one frame are not the same as the next. These figures are intended to show the distribution of the loads in the $\sigma_{11} - \sigma_{12}$ load space rather than the values of loads themselves.

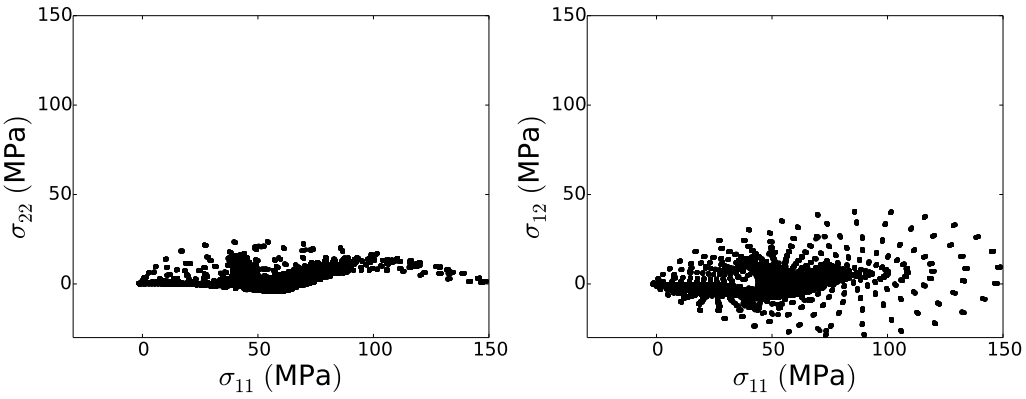

(a) $\sigma_{11} - \sigma_{22}$.

(b) $\sigma_{11} - \sigma_{12}$.

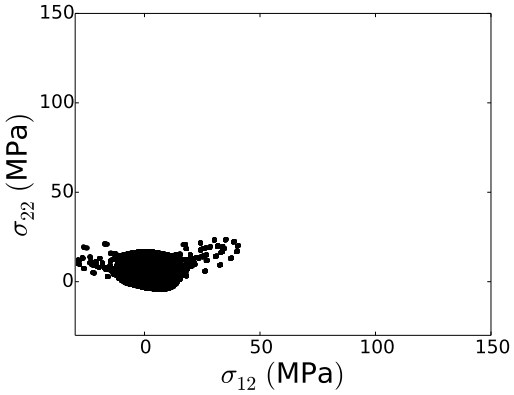

(c) $\sigma_{12} - \sigma_{22}$.

Figure 3.12: The multi-axial stress state distributions of various points (nodes) from FEA performed on the Meuwissen specimen at a time step during elastic deformation at the beginning of loading. The applied load is 8 kN.

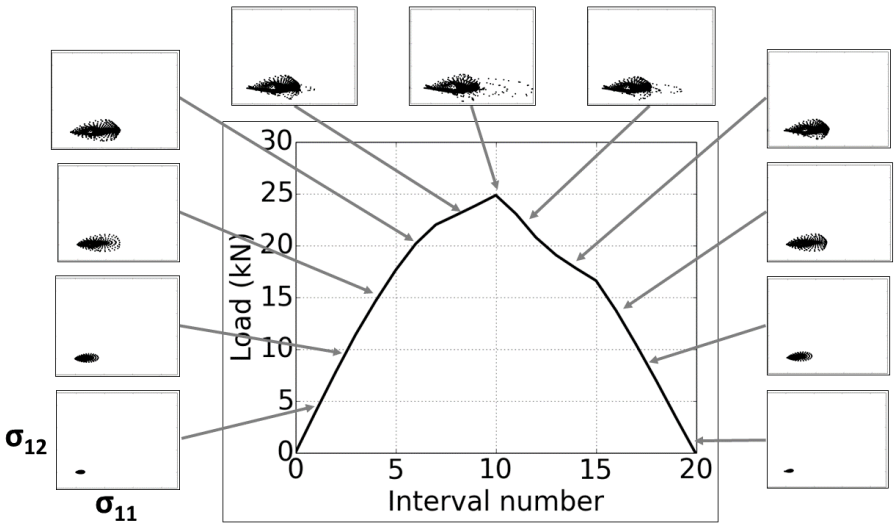

Figure 3.13: Evolution of the load distributions in the specimen throughout the test between σ_{11} and σ_{12}. The load applied at the boundary of the specimen is shown, and each frame indicates the load state of each individual point on the specimen at that time step.

3.5 Summary and conclusions

Two notable accomplishments have been made in this particular pseudoelastic loading of SMAs study. First, it has been demonstrated that highly accurate and reliable SMA material constitutive model parameter calibration may be achieved by performing just a single pseudoelastic loading test on one specimen by using a non-uniform specimen geometry such as the Meuwissen shape. Any additional experiments performed may be used exclusively for experimental validation of the calibration result. The second accomplishment is seen as the furtherance of the characterization of this particular material. The loading scheme introduced by the Meuwissen shape allows for characterization of the material response to more than uniaxial loads to be performed. This is a special contribution as a unique and phenomenal way to demonstrate the anisotropic phase transformation behavior for this

material. In fact, this was achieved by variation of only the specimen geometry. Future work in this topic may explore use of this method in other materials, material systems, or to also study the martensite/austenite yield surfaces in addition to transformation surfaces.

4. EXPERIMENTATION PART III: MICROSCOPIC CHARACTERIZATION OF SHAPE MEMORY ALLOY PARTICLES*

4.1 Introduction

Knowledge of fatigue cracks in aerospace materials is a major concern in the long-term use of aircraft. Currently, aircraft undergo routine overhauls at specified intervals during the lifetime of the vehicle in which major dismantling occurs, followed by detailed part-by-part inspection for fatigue cracking (c.f. Nechval, Nechval, Purgailis, and Strelchonok (2011)). Using methods for sensing compositional changes in embedded active-material particles, sensory particles, as a method for non-destructive evaluation (NDE) is proposed for giving real-time sensing of fatigue crack growth in key structural members of an aircraft which are susceptible to fatigue. This NDE method is intended to alleviate the need for frequent dismantling of aircraft, as well as to provide a live status update on the presence of fatigue cracks in the aircraft components.

Figure 4.1 provides an illustration of the sensory particle concept. A sensory particle located near the crack tip has a response (mechanical, acoustic, magnetic, resistive) to the intensified stress field which can be detected using existing NDE methods. Various material systems may be used as sensory particles, allowing various NDE sensing methods to be incorporated. Some possible NDE methods include acoustic sensing of phase transformation in shape memory alloys (SMAs, e.g., NiTi) (Bogdanoff & Fultz, 2001), magnetic sensing of reorientation of martensitic variants

*Reprinted with permission from Development and Characterization of Embedded Sensory Particles Using Multi-Scale 3D Digital Image Correlation by Cornell, S. R., Leser, W. P., Hochhalter, J. D., Newman, J. A., and Hartl, D. J., 2014, *ASME 2014 Conference on Smart Materials, Adaptive Structures and Intelligent Systems*, (p. V002T02A010), Copyright 2014, American Society of Mechanical Engineers.

in magnetic shape memory alloys (MSMAs, e.g., NiMnGa) (Karaca et al., 2006), or detection of changes in resistance of piezoelectric materials (e.g.,$BaTiO_3$) (Hiruma et al., 2004). In the present work, the NiTi shape memory alloy (SMA) was used as the sensory particle material, which emits an acoustic signal upon the onset of stress-induced martensitic phase transformation.

Development of the sensory particle concept relies on the use of advanced material modeling methods. Calibration of the constitutive model parameters must be performed through iterative comparison between experimental full-field measurement results and simulation. The strain measurements performed in this work are intended to provide detailed information for calibration. Mode-I loading of fatigue pre-cracked single-edge notch (SEN) specimens was used to generate data for calibration, and provide a first-step analysis of the behavior of the sensory particle and matrix material in the presence of a fatigue crack.

3D digital image correlation (3D-DIC) was used in these experiments to measure the full-field strain distribution on the surface of the specimens. This technique utilizes optical discontinuities to track the displacements, both in and out of plane, at many different points on the specimen surface during a test. For DIC, the surface of a specimen must have a random distribution of visual discontinuity, or speckle pattern. If the material being tested does not have a naturally occurring speckle pattern, one must be applied using one of many possible speckling techniques (M. A. Sutton et al., 2009).

Speckle patterning can be performed in many different ways for different applications. For this work, a speckle pattern was applied at both the micro- and macro- scales. Creating a speckle pattern at the microscale is especially challenging; Kammers and Daly (2011) reviewed several techniques for speckle patterning at a microscale. Some techniques include nanoparticle surface deposition (this method was

used with an optical stereo-microscope) (Berfield et al., 2007), chemical vapor deposition (Scrivens et al., 2007), and e-beam lithography (Li, Guo, & Sutton, 2011). For macroscale patterning of metallic materials, spray paint speckle-patterning is commonly used (M. A. Sutton et al., 2009).

4.2 Experimental method

Specimens were fabricated using aluminum alloy 7050 with embedded NiTi (50.9 atomic % Ni) shape memory alloy (SMA) particles. Aluminum alloy 7050 is a common aerospace structural material which was identified as being of particular interest for the sensory particle concept. Figure 4.2 is a diagram that shows the fabrication technique for creating the material specimens with embedded NiTi particles. 100 µm-diameter gas atomized NiTi particle spheres were scattered onto an aluminum alloy

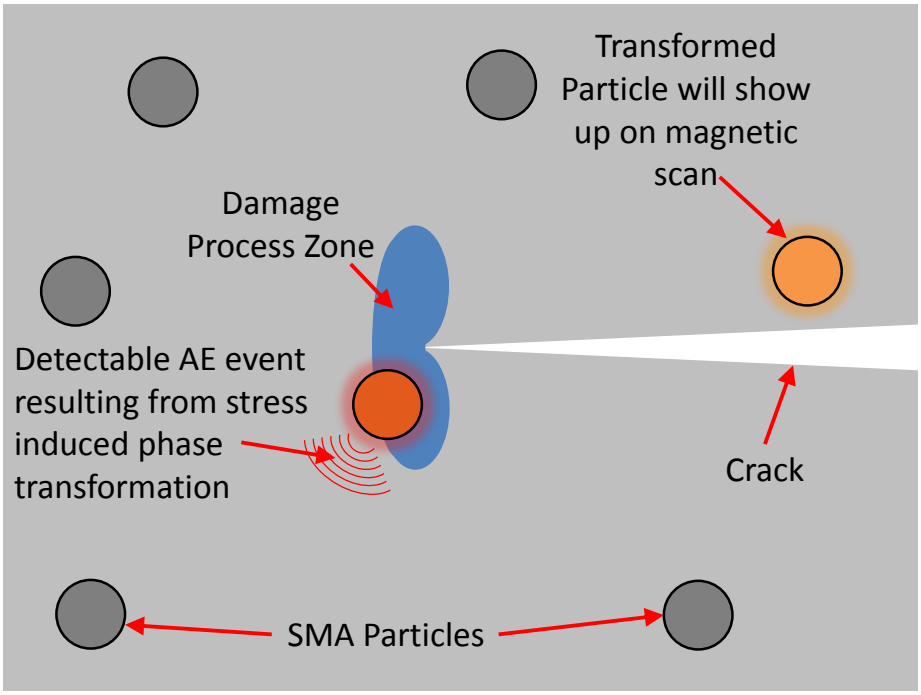

Figure 4.1: A schematic of the sensory particle concept. Various types of sensory particles may be used, including SMAs, MSMAs, or piezoelectrics.

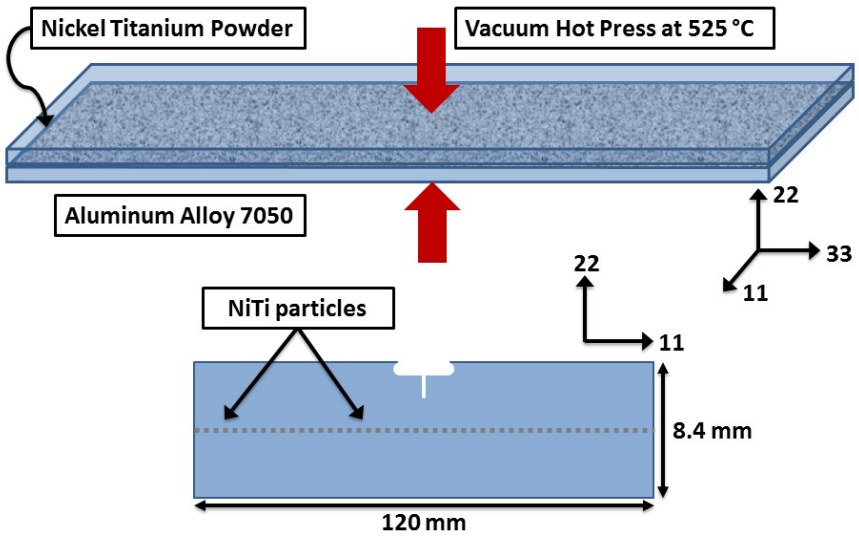

Figure 4.2: Schematic of hot-pressing and machining of test specimens.

7050 plate. A second aluminum plate was placed on top of the particle bed, and the plates were vacuum hot-pressed at 525 ^{o}C and 35 MPa for 1 hour to create the bulk panel. The panel was solutionized at 490 ^{o}C for 6 hours and peak aged at 121 ^{o}C for 24 hours in vacuum. The mechanical properties of the aluminum matrix material were measured to be $E = 80$ GPa and $\sigma_{11} = 425$ MPa. Figure 4.2 illustrates the SEN specimens that were cut from the cross-section of the hot-pressed panel by electrical discharge machining (EDM). Consequently, the sensory particles were aligned along the center-line of the specimen.

The experiments presented in this section mimic application of sensory particles to provide proof of concept. Before testing the specimen with 3D-DIC at multiple scales, the specimen was pre-cracked up to 200 µm from the interface of NiTi particles. This was accomplished by fatigue cycling at a stress intensity factor of $K_{max} = 7.25$

$\text{MPa}\sqrt{\text{m}}$, load ratio $R = 0.1$, and frequency of 20 Hz. The resulting crack length was 4.0 mm.

The fatigue pre-cracked SEN specimen was prepared for DIC using two different speckle pattern techniques. E-beam lithography was applied to the specimen such that the pattern covered one or more NiTi particles (Gupta, Willard, Hochhalter, & Smith, 2014). This pattern was applied over a 2 mm^2 area with 2 µm diameter speckles. Figure 4.3 shows the microscale speckle pattern applied for this work. Next, a macroscopic speckle pattern was applied to the entire specimen by first masking the microscale speckle pattern using tape then applying a spray paint macroscale speckle pattern. For the macroscale DIC measurements, the entire specimen surface was prepared by first spray painting a white background on the specimen with sufficient thickness to circumvent reflection of light from the metallic specimen surface. Subsequently, a random pattern of black spray paint speckles was applied to the specimen surface. It should be noted that the lighting should be optimized for speckle pattern contrast.

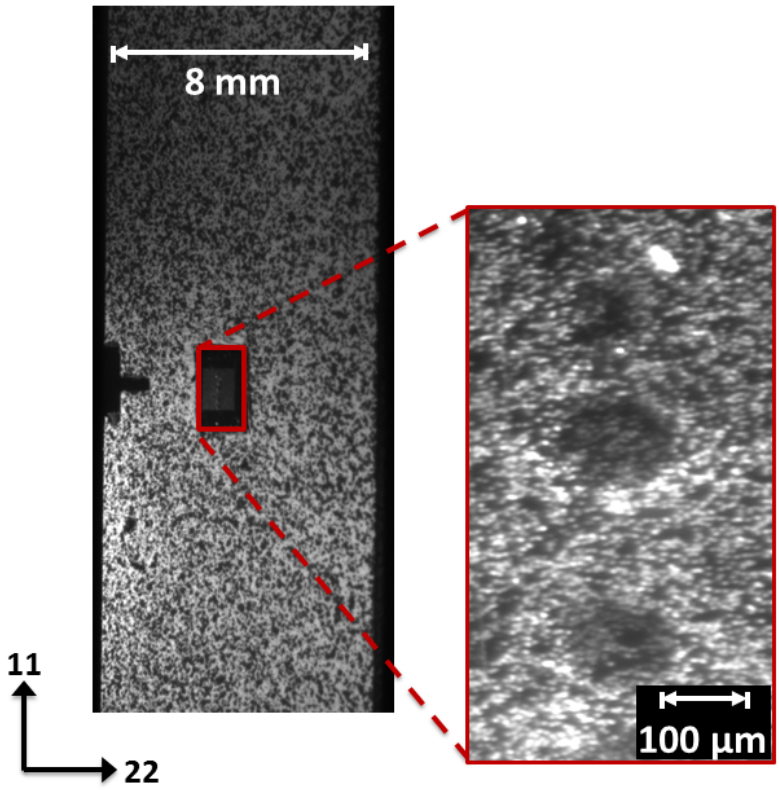

Figure 4.3: Speckle patterns applied to the specimen. The spherical NiTi particles can be seen inside the aluminum alloy 7050 matrix in the microscale image (right image).

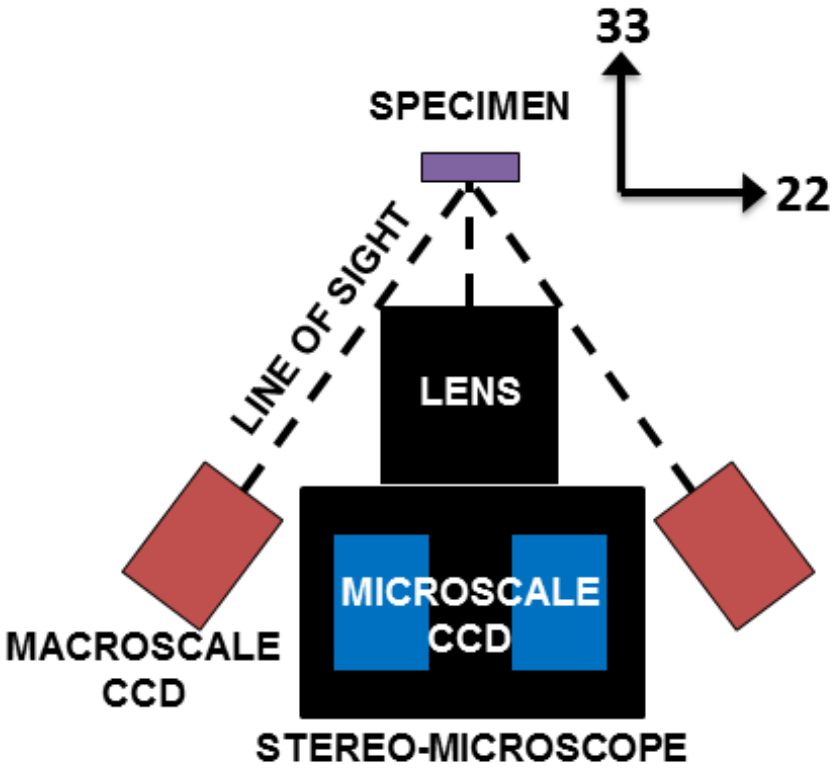

Figure 4.4: Orientation of multi-scale 3D-DIC system (4 cameras total).

Figure 4.4 shows the configuration of the stereo-microscope and macroscale charge-coupled device (CCD) cameras with respect to the specimen. This configuration provides simultaneous 3D-DIC measurement of the macroscopic and microscopic deformations at the specimen level and within the sensory particles, respectively. For fatigue crack growth experiments, it is necessary to understand the deformation response of the material at the macroscale and near the specimen boundary conditions as the crack propagates through the material but also be able to analyze the behavior very near the crack tip and at a scale comparable to the size of the sensory particles ($\sim 100\,\mu m$). The macroscale measurements also provide boundary conditions for subsequent modeling efforts. Therefore, performing analysis at two different scales

simultaneously is an important capability for this study.

Microscale measurements were performed using the VIC-3D Micro^{TM} system by Correlated Solutions, Inc. (2014). The 3D-DIC macroscale measurements were performed using two 5-megapixel CCD cameras with 23 mm lenses. The macroscale cameras were attached on either side of the stereo-microscope in a plane parallel to the isolation optical table. The stereo-microscope has a fixed focal length; therefore, with the specimen placed in the test stand grips, the image for the stereo-microscope was focused after which the image for the macroscale cameras was focused. The maximum magnification that can be achieved using the stereo-microscope is $11.8x$ magnification with a field of view (FOV) of 1 mm^2, which was the magnification used in the experiments described herein.

A 15 kN load cell was used with wedge grips for the crack growth specimen load-to-failure test. The table-top test stand and DIC setup was placed on an optical isolation table to minimize vibrations in the DIC measurements. The test was performed under stroke control at 0.05 mm/s. A single over-load cycle was applied to the fatigue pre-cracked SEN specimen such that $K_{max} = 39.1$ MPa$\sqrt{\text{m}}$ and unloaded, over a period of 600 seconds. Images were obtained during the over-load cycle at 1 Hz, and captured using a software-trigger in VIC-Snap^{TM} (Correlated Solutions, Inc., 2014) such that all four cameras captured images simultaneously.

4.3 Results

4.3.1 Macroscale 3D-DIC results

Figure 4.5 illustrates strain fields measured at six different times during the over-load cycle. The spatial resolution of the macroscale DIC measurement is 0.022 mm. Figure 4.5a shows the times when the images were selected and Figure 4.5b shows the axial strain contours (ε_{11}) in the specimen. The images in Figure 4.5b correspond

to the numbered points in Figure 4.5a. Crack propagation occurred between images 2 and 3. The effect of the propagation can be seen in these images. Displacements can be extracted along the lines that form the boundary of the images and applied as constraints to a corresponding FE model.

4.3.2 Microscale 3D-DIC results

The microscale 3D-DIC axial strain measurements within the sensory particles of interest, near the crack tip, are shown in Figure 4.6. The spatial resolution of the microscale DIC measurement is 0.25 m, as compared to 0.022 mm spatial resolution for the macro-scale DIC measurement. The strain resolution was calculated to be the spatial resolution devided by the specimen length. Hence, the strain resolution at the micro-scale is 7.52 microstrain, and at the macro-scale is 670 microstrain. Hence, the difference in strain resolution is 1/90 between the microscale and macroscale measurements. Figure 4.6 shows the contour fields of axial strain (ε_{11}) in the specimen close to the crack tip corresponding to the time points shown in Figure 4.5a. The area of interest (AOI) for the DIC analysis was chosen just below the crack tip, and included two sensory particles and the surrounding matrix material. Additionally, DIC results could only be obtained for the bottom portion of the sensory particle closest to the crack tip because of poor DIC correlation. Future experiments will explore methods for improving DIC correlation on a particle and increasing DIC resolution. A second particle farther from the crack tip was also included in this AOI. The AOI was selected below the crack tip because of poor correlation in the area closer to the crack tip.

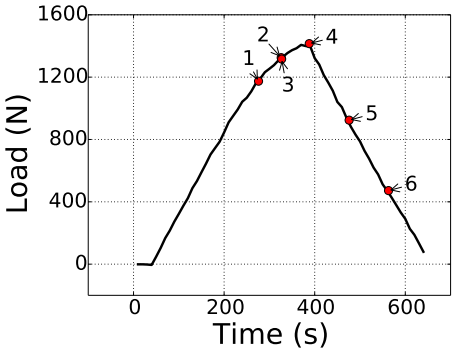

(a)

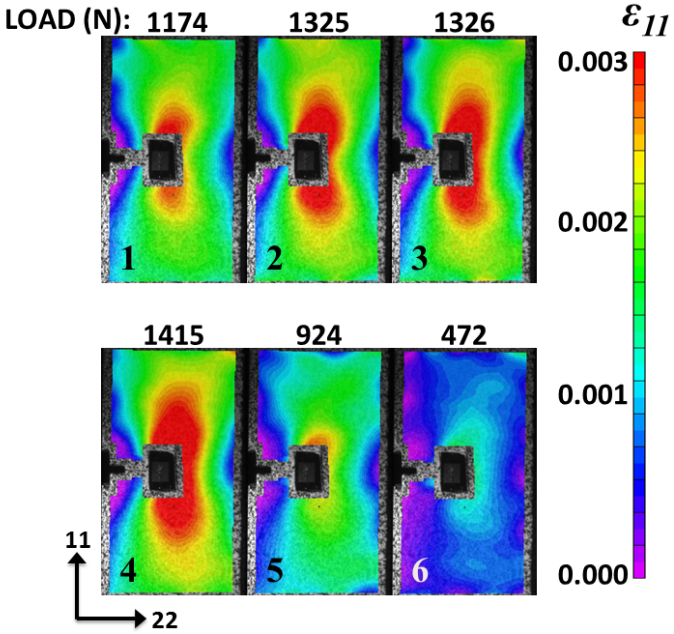

(b)

Figure 4.5: (a) Externally applied load vs time plot showing the times when the DIC images were selected, and (b) 3D-DIC full-field axial strain (ε_{11}) macroscale results.

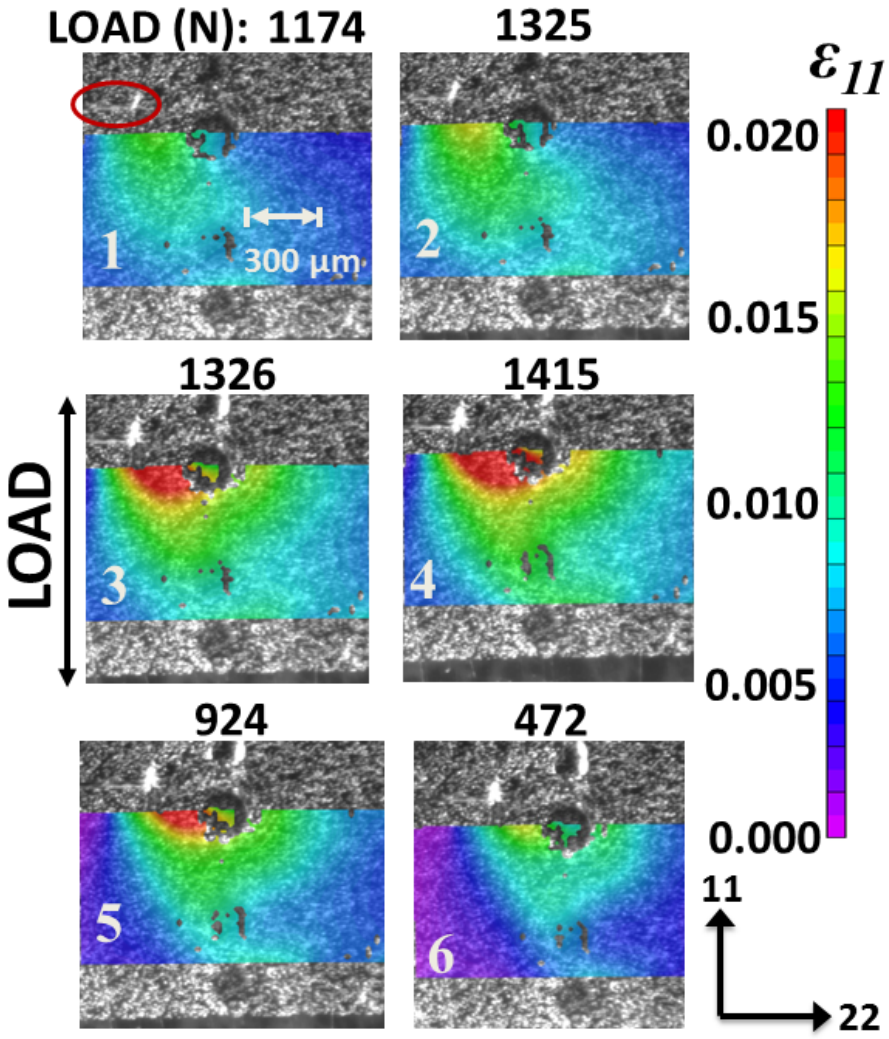

Figure 4.6: Microscale 3D-DIC axial strain (ε_{11}) results surrounding the crack at time points shown in Figure 4.5a. The crack location is indicated by the red circle.

Image 1 in Figure 4.6 shows the axial strain (ε_{11}) field before the peak load. Image 2 followed by image 3 demonstrates the effect of crack propagation on the measured strain field. Image 4 shows the ε_{11} contours at the peak applied load during the experiment, which was 1415 N. Images 5 and 6 show the ε_{11} contours during unloading.

Figure 4.7 demonstrates the strain behavior at two particles near the crack tip. As

seen in Figure 4.7a, Particle 1 is very close to the crack tip (indicated by the red line), while Particle 2 is farther from the crack tip. The blue and red dots are the points at which local strain measurements were extracted in Figure 4.7b. It can be seen from Figure 4.6 that between images 2 and 3 a sharp change in strain occurred, which is associated with the crack propagation event mentioned previously. At the same load in Figure 4.7, it is seen that a corresponding sharp increase in strain occurred in Particle 1 (blue line in Figure 4.7). This sharp change in particle behavior indicates martensitic phase transformation. Phase transformation did not occur in Particle 2.

This brief analysis of the sensory particle transformation in the presence of a crack demonstrates the importance of modeling to fully understand the observed behavior. To calibrate the constitutive model parameters of the sensory particles, comparison of a simulation to the experimental strain results is still needed. It is expected that by reproducing this experiment in a simulation, the fundamental behavior of the sensory particles can be understood.

4.4 Summary and conclusions

The key features of this work may be summarized in the following points:

1. A novel method for deformation measurement at multiple scales has been explored, which utilizes the 3D-DIC full-field measurement technique. Microscopic 3D-DIC was performed through a stereo-microscope simultaneously with a standard macroscopic 3D-DIC setup.

2. The sensory particle concept was explored further by single-cycle tensile loading of a fatigue crack growth sensory particle specimen. The material specimen consisted of gas atomized NiTi (50.9 atomic % Ni) as the sensory material surrounded by aluminum alloy 7050 matrix. Using the 3D-DIC setup, sensory particle transformation was detected near the growing fatigue crack.

This work has introduced crack growth experimentation for the sensory particle concept. The purpose of performing these experiments is primarily to provide a proof of concept and to improve the fidelity of future modeling. High fidelity models of sensory particle crack growth specimens are currently being obtained from x-ray

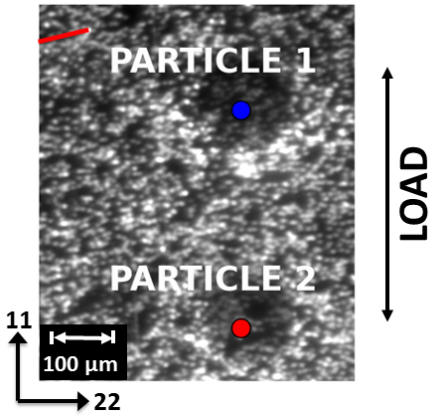

(a)

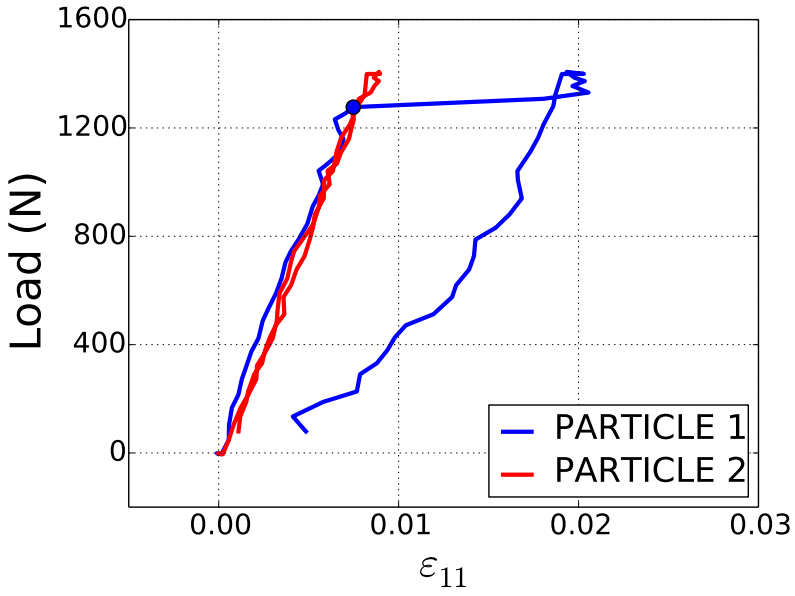

(b)

Figure 4.7: (a) Analysis point chosen in Particle 1 and location of the crack (red line), and (b) axial strain (ε_{11}) response at that analysis point.

computed tomography (CT) and should be used in an attempt to replicate measured results. In addition to being able to calibrate the material parameters for the model, these studies will be able to provide a more rigorous analysis of the sensory particle concept. Future experiments will explore the effect of high-cycle fatigue. Additionally, studies should be performed to explore alternative sensory particle materials and NDE methods.

5. STRESS ANALYSIS OF THE LOCALIZED HEATING PROBLEM

This section is an analytical evaluation of the results obtained in Section 2. In this section, an estimation of the stress field is made analytically (i.e., without the use of FEA solver tools) from the full-field strain and full-field temperature data obtained from the experiment. The nature of the experiment performed on the plate specimen inherently creates a case of prominent stress redistribution due to the microstructural changes occurring locally in different regions of the specimen. This analysis was performed for both the thin strip and plate specimens. Figure 5.1 shows a photograph of the two specimens.

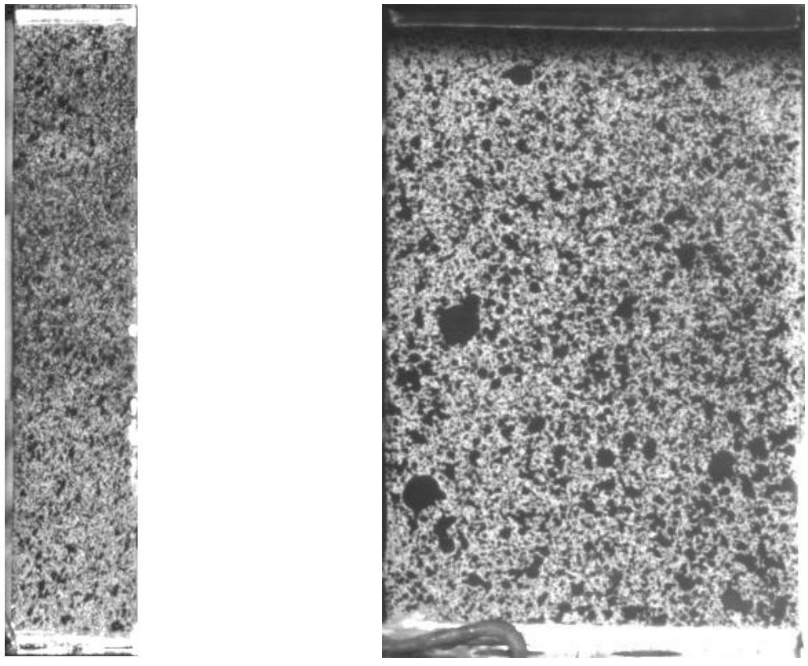

(a) SMA thin strip specimen. (b) SMA plate specimen.

Figure 5.1: SMA thin strip and plate specimens.

Heat was introduced to a local area using a heating pad. The specimen which was initially at martensite experienced phase transformation locally, causing a drastic redistribution of stress to occur between the regions of high and low temperature (i.e., regions of high and low reverse transformation, respectively), especially for the plate specimen.

The SMA constitutive model used here will be reviewed and the 2-D reduction of these equations will be demonstrated. Then, the optimization algorithm used to obtain the multi-dimensional stress state inside the specimen will be described, and the results will be shown.

5.1 Phase diagram construction

Results from experiments performed on the same specimen before the localized heating have been used to construct a phase diagram. Two isobaric (constant stress) experiments were performed on the specimen as described in detail in Section 2. These two experiments first at 200 MPa then at 100 MPa were performed before localized heating. Figure 5.2 shows the results of these experiments; note that the results in Figure 5.2 were modified data which do not show the transformation induced plasticity (TRIP) effects from the experiments (c.f. Section 2). The phase diagram was constructed via the tangent line method (D. Lagoudas, 2008) from these results.

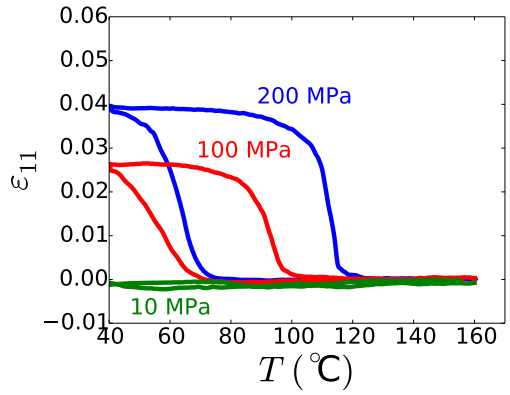

(a) Thin strip specimen.

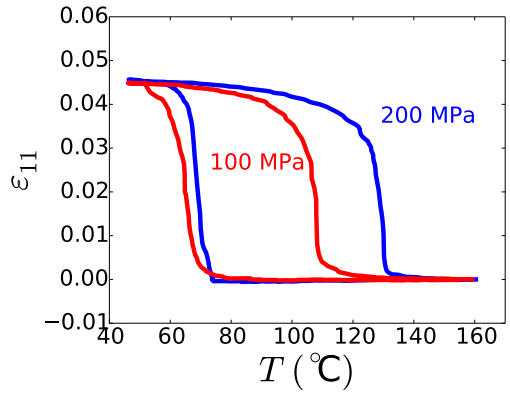

(b) Plate specimen.

Figure 5.2: ε_y vs temperature showing the ambient heating/cooling for the plate specimen. This figure has been modified to exclude the effects of TRIP.

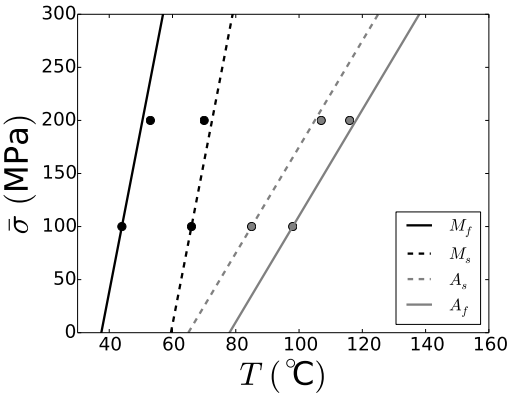

(a) Thin strip specimen material phase diagram.

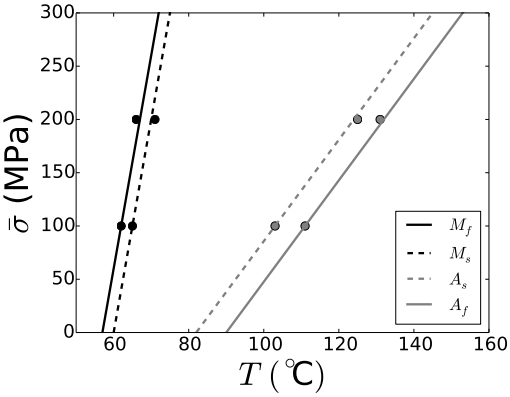

(b) Plate specimen material phase diagram.

Figure 5.3: Stress vs temperature phase diagram estimated by data from Figure 5.2. $\bar{\sigma}$ represents the effective applied stress.

Figure 5.3 shows the phase diagram for the thin strip and plate specimens. In the stress (F/A_0) vs temperature space, when the material state is to the left of the M_f line, the material is in martensite ($\xi = 1$). When the material state is to the right of the A_f line, the material is in the austenite phase. The points indicated are data obtained from Figure 5.2 by the tangent line method (D. Lagoudas (2008), Section 2). The slope of the M_f and M_s lines (C_M) as well as the slope of the A_s and A_f lines (C_A) were determined by the equation

$$C_\gamma = 1 \,/\, \left(\frac{1}{C_{\gamma_s}} + \frac{1}{C_{\gamma_f}} \right) \tag{5.1}$$

where $\gamma = M,\ A$; C_{γ_s} and C_{γ_f} are the slopes of the γ_s and γ_f lines (i.e., the lines passing through the data points). For the current experimental results, the critical transformation temperatures (A_f, A_s, M_f, M_s) in the phase diagram were assumed to have a linear realationship with applied load (Wu et al., 2003).

5.2 Full-field strain measurements

5.2.1 Thin strip specimen full-field strain measurements

The results of localized heating for the plate specimen are graphically summarized in Figure 5.5, where the temperature, axial strain, transverse strain, and shear strain fields at different consecutive time steps are all shown.

The measurements demonstrated in Figure 5.5, are in the calculation of the stress estimate shown later in this section. The images shown here are organized according to individual time steps for which power was applied consecutively in a quasistatic manner. For each frame, an additional amount of power was applied to the specimen. Each frame shows the strain/temperature full-field measurement results for the same specimen at the various power inputs, and these are included for the axial strain (ε_{11}), transverse strain (ε_{22}), shear strain (ε_{12}), and temperature (°C). Figure 5.4 shows the

input of power to the heater with time, and the analysis time steps which correspond with the number of Figure 5.5.

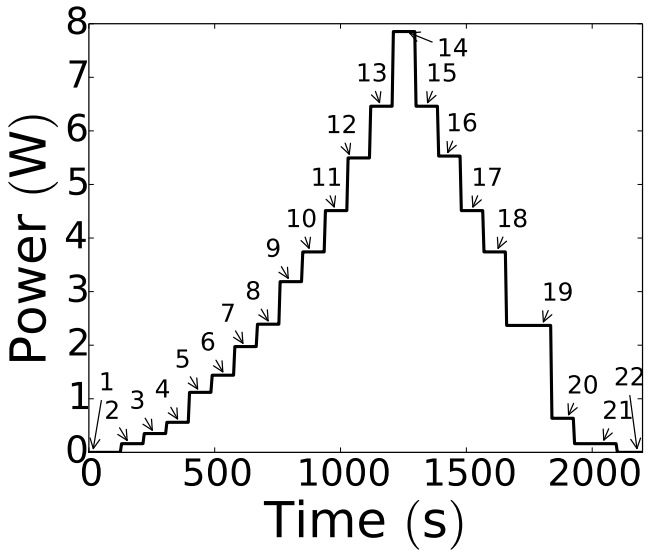

Figure 5.4: Power applied over time to the specimen heater.

5.2.2 Plate specimen full-field strain measurements

The results of localized heating for the plate specimen are graphically summarized in Figure 5.6, where the temperature, axial strain, transverse strain, and shear strain fields at different consecutive time steps are all shown.

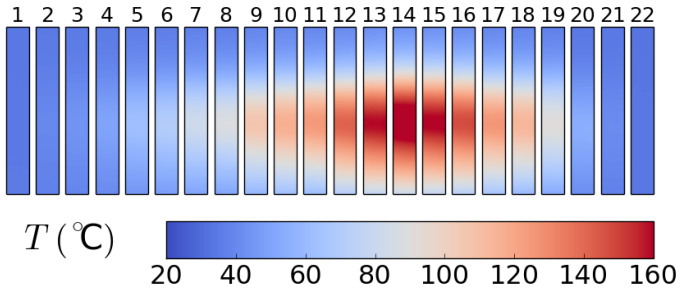

(a) Temperature measured with IR camera.

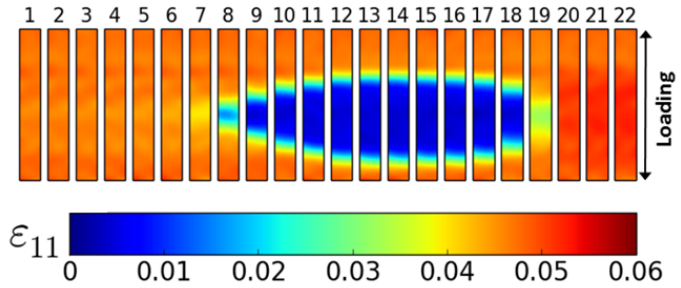

(b) Axial strain (ε_y) in the loading direction.

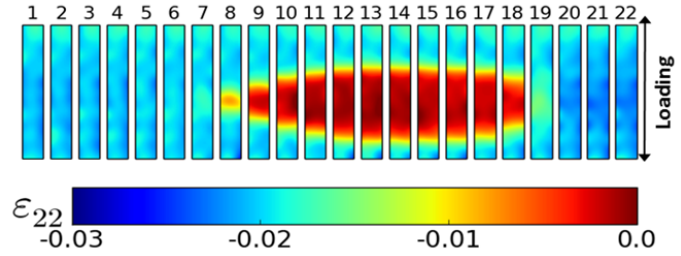

(c) Transverse strain (ε_x).

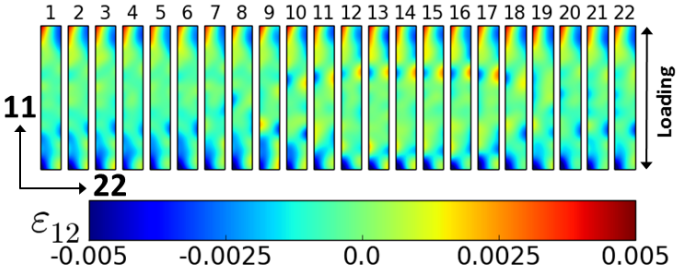

(d) Engineering shear strain ($\gamma_{xy} = 2\varepsilon_{xy}$).

Figure 5.5: Full-field temperature and strain measurements for the thin strip specimen.

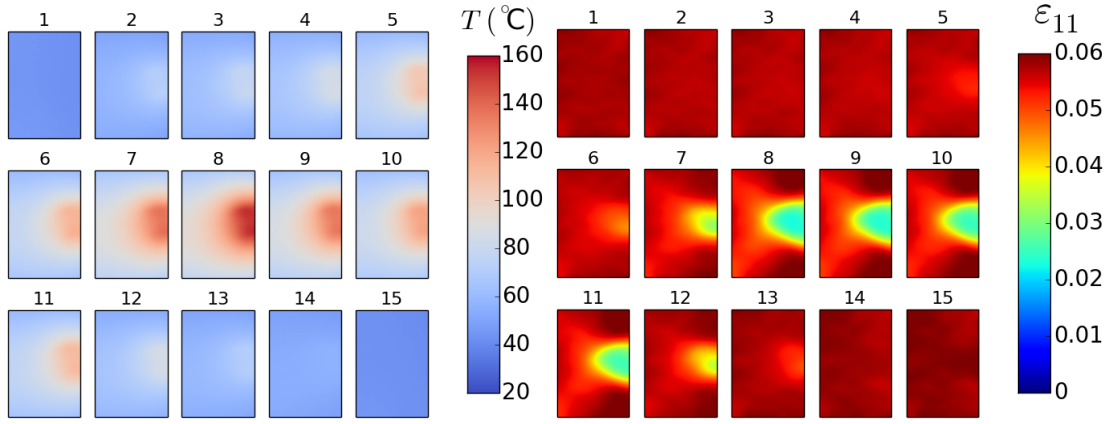

(a) Temperature measured by IR camera. (b) Axial strain (ε_y) in the loading direction.

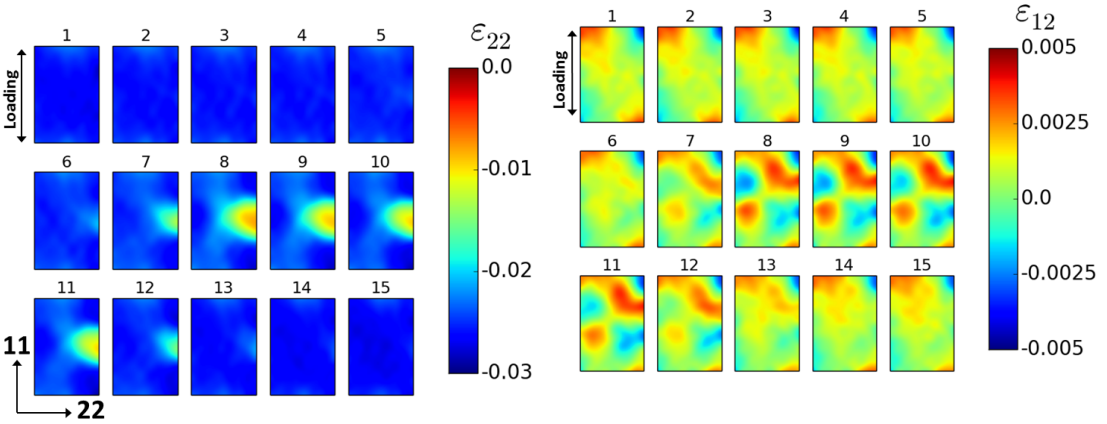

(c) Transverse strain (ε_x). (d) Engineering shear strain ($\gamma_{xy} = 2\varepsilon_{xy}$).

Figure 5.6: Full-field temperature and strain measurements for the plate specimen.

The time steps correspond with the steps in quasistatic power input to the heater. (see Figure 5.1). Figure 5.7 shows the input of power to the heater with time, and the analysis time steps which correspond with the number of Figure 5.6.

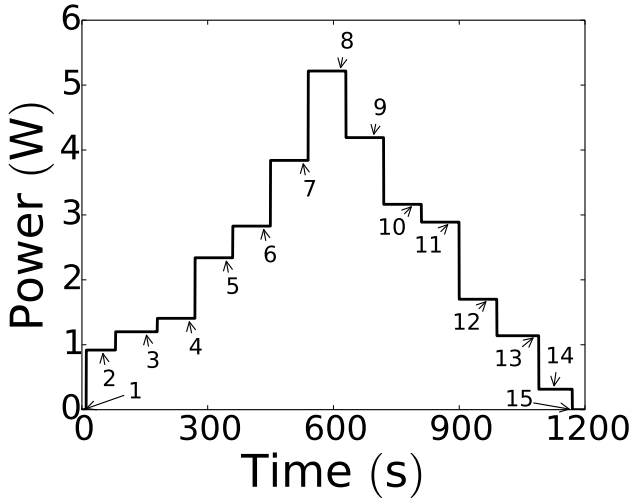

Figure 5.7: Power applied over time to the specimen heater.

In Figures 5.6b and 5.6c the strong transformation-induced strain gradients arising from the temperature variation in the specimen are observed. We can make a few qualitative observations from these results. First, we observe the expected 2-D distributions of strain which change in the presence of phase transformation. These large strain gradients in particular will lead to sharp stress gradients across the specimen width given the coordinated application of force and deformation to the gripped (i.e., top and bottom) boundaries. Secondly, we notice a shear symmetry in the thermal and axial to transverse strain results, and an associated anti-symmetry in the shear strains. The minor deviation from perfect symmetry is thought to be a result of non-ideal heater installation. Finally, we notice the more pronounced interaction between boundary (grip) effects and thermal non-homogeneity resulting from the low aspect ratio of the specimen.

5.3 Estimating local stress from localized heating

The internal stress state in a material may be determined from the experimental results and constitutive relation for the material. Calculation of the stress in a material from experimental results has been performed before, especially for estimating the stress field surrounding a crack tip: Dally and Sanford (1987) has peformed estimation of the mode I stress intensity factor from strain gage readings. Furthermore, Machida and Yamada (2004) have developed a method for estimating the crack tip stress field from 2-D DIC data, which also utilizes the hybrid method for highlighting and eliminating experimental deformation measurement errors (Nishioka, Kurio, & Nakabayashi, 2000). Silva and Ravichandran (2009) also performed stress analysis of a damaged composite from thermal imaging and DIC data; the temperature changes slightly in the presence of stress concentrations, which are predicted with high fidelity combining the relationship between the temperature and the stress as well as the elastic constitutive relation of the material, utilizing the deformation data. Similar research has also been performed for analyzing the residual stresses in a material due to damage in processing and other effects (Lord, Penn, & Whitehead, 2008) (Schajer, 2010) (Sebastiani, Eberl, Bemporad, & Pharr, 2011).

From the localized heating experiments, full-field strain and temperature data has been obtained which may be utilized to obtain the stress field in the material through inverse optimization of the SMA constitutive model. In the following sections, the stress estimation is based from the standpoint of the material phase diagram (c.f. Figure 5.3. Subsequently, the SMA constitutive model used here is reviewed, and 2-D plane stress reduction is performed.

5.3.1 Stress estimation from the phase diagram

The local stress in a material due to localized heating may be estimated by examination of the material phase diagram, which is reproduced in Figure 5.8, which shows only the austenite start and finish transformation surfaces. This figure provides an illustration of the process of stress estimation in material which is undergoing phase transformation. At the analysis point in the material of greatest temperature gradient (see Figure 5.2), the material achieved 65% strain recovery at 155°C. Note that during reverse transformation, $\xi = 1$ when 0% strain recovery has occurred; similarly, $\xi = 0$ when 100% strain recovery has occurred. The variation of ξ with temperature is assumed linear, thus the stress at the identified temperature and strain recovery values may be estimated. At 155°C and 65% strain recovery, the corresponding stress on the phase diagram is 302 MPa, as shown in Figure 5.8.

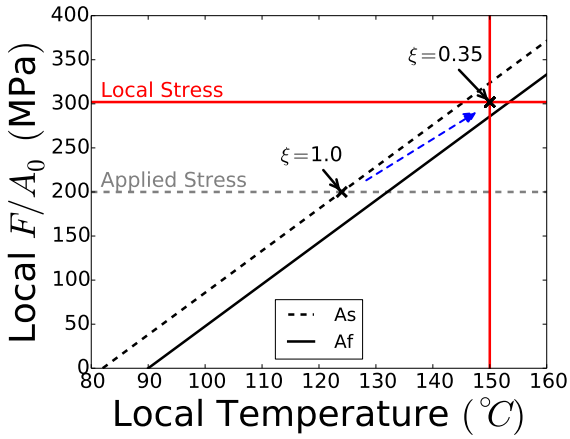

Figure 5.8: Phase diagram with temperature value and approximated stress value indicated, based on the maximum strain recovery indicated in Figure 5.2. The blue arrow indicates the evolution of the material states at the indicated analysis point from $F/A_0 = 200$ MPa ($\xi = 1.0$) to $F/A_0 = 302$ MPa ($\xi = 0.35$). However, this path cannot be assumed as linear, because the relationship between local temperature variation and local strain recovery cannot be assumed as linear.

Using this technique, the achieved stress at various locations across the width of the specimen may be estimated. The stress may be calculated by the equation

$$\xi_L = \frac{\left(A_f^0 + \frac{\bar{\sigma_L}}{C^A}\right) - T_L}{A_f^0 - A_s^0}, \tag{5.2}$$

where ξ_L is the local martensitic volume fraction, A_f^0 and A_s^0 are the austenite finish and start temperatures when no load is applied, $C^A = \frac{\partial \sigma}{\partial T}$ is the slope of the austenite start and finish transformation surfaces, $\bar{\sigma}_L$ is the local effective stress, and T_L is the local temperature. Thus, stress may be found by rearranging the above:

$$\bar{\sigma}_L = \left(\xi + \frac{T_L - A_f^0}{A_f^0 - A_s^0}\right)\left(C_A\left(A_f^0 - A_s^0\right)\right). \tag{5.3}$$

5.3.2 2-D reduction

The constitutive model is reduced to a 2-D form through which the stress field may be estimated given full-field ε_y, ε_x, ε_{xy}, and temperature data on the specimen surface. The reduction is possible via a plane stress assumption which is a good approximation for the plate specimen (thickness/width ratio of 1/90). Note that index notation will be used from now on for which cartesian unit vectors are denoted by the numbers $1-2-3$ instead of $x-y-z$. 1 and 2 denote the x and y directions, respectively, in this notation. The plane stress assumption states that

$$\sigma_{33} = \sigma_{13} = \sigma_{23} = 0. \tag{5.4}$$

Beginning from Equation (1.49),

$$\boldsymbol{\varepsilon} = -\rho\frac{\partial G}{\partial \boldsymbol{\sigma}} = \mathbf{S}\boldsymbol{\sigma} + \boldsymbol{\alpha}\left(T - T_0\right) + \boldsymbol{\varepsilon^t}, \tag{5.5}$$

where the compliance tensor ($\mathbf{S}$) is dependent on the material state during phase transformation, for which a linear relation is assumed. Note that non-linear relations may be used in more complex models than what is presented here. The linear relation is given by (D. Lagoudas (2008), chapter 3)

$$\mathbf{S} = \mathbf{S^A} + \xi(\mathbf{S^M} - \mathbf{S^A}). \tag{5.6}$$

For an isotropic material under the plane stress assumption, $\mathbf{S}$ reduces to (Christensen (1979), chapter 5)

$$\mathbf{S}^\gamma = \begin{bmatrix} \frac{1}{E^\gamma} & -\frac{\nu}{E^\gamma} & 0 \\ -\frac{\nu}{E^\gamma} & \frac{1}{E^\gamma} & 0 \\ 0 & 0 & \frac{(\nu+1)}{E^\gamma} \end{bmatrix}. \tag{5.7}$$

where $\gamma = A,\ M$ indicates the austenite or martensite phase. Substituting (5.7) to Equation (5.6) gives

$$\mathbf{S} = \begin{bmatrix} \left(\frac{1-\xi}{E^A} + \frac{\xi}{E^M}\right) & \nu\left(\frac{\xi-1}{E^A} - \frac{\xi}{E^M}\right) & 0 \\ \nu\left(\frac{\xi-1}{E^A} - \frac{\xi}{E^M}\right) & \left(\frac{1-\xi}{E^A} + \frac{\xi}{E^M}\right) & 0 \\ 0 & 0 & (1+\nu)\left(\frac{1-\xi}{E^A} + \frac{\xi}{E^M}\right) \end{bmatrix}. \tag{5.8}$$

Furthermore, the coefficient of thermal expansion (CTE, or α) tensor is written here as for an isotropic body, thus $\boldsymbol{\alpha}$ may be written as (Boley and Weiner (1960), chapter 8)

$$\boldsymbol{\alpha} = \begin{bmatrix} \alpha & 0 & 0 \\ 0 & \alpha & 0 \\ 0 & 0 & \alpha \end{bmatrix}. \tag{5.9}$$

Integration of Equation (1.54) gives

$$\boldsymbol{\varepsilon^t} = \xi \boldsymbol{\Lambda^t}. \tag{5.10}$$

For forward transformation, $\boldsymbol{\Lambda^t_{fwd}}$ is dependent on the stress state as (D. Lagoudas et al., 2012)

$$\boldsymbol{\Lambda^t_{fwd}} = \frac{3}{2} H^{cur}\left(\bar{\sigma}\right) \frac{\boldsymbol{\sigma'}}{\bar{\sigma}}, \tag{5.11}$$

where $\boldsymbol{\sigma'}$ is the deviatoric part of the stress tensor, and $\bar{\sigma}$ has the Mises-based definition (D. Lagoudas et al., 2012)

$$\bar{\sigma} = \sqrt{\frac{3}{2}\boldsymbol{\sigma'} : \boldsymbol{\sigma'}}, \tag{5.12}$$

which after the plane stress assumption becomes

$$\bar{\sigma} = \sqrt{\left(\sigma_{11} - \sigma_{22}\right)^2 + 3\sigma_{12}^2}. \tag{5.13}$$

In 2-D, $\boldsymbol{\Lambda^t_{fwd}}$ may be written as

$$\boldsymbol{\Lambda^t_{fwd}} = \begin{bmatrix} \Lambda^{t\ 11}_{fwd} \\ \Lambda^{t\ 22}_{fwd} \\ \Lambda^{t\ 12}_{fwd} \end{bmatrix} = \begin{bmatrix} \frac{1}{2} H^{cur}\left(\bar{\sigma}\right) \frac{2\sigma_{11} - \sigma_{22}}{\sqrt{\left(\sigma_{11} - \sigma_{22}\right)^2 + 3\sigma_{12}^2}} \\ \frac{1}{2} H^{cur}\left(\bar{\sigma}\right) \frac{2\sigma_{22} - \sigma_{11}}{\sqrt{\left(\sigma_{11} - \sigma_{22}\right)^2 + 3\sigma_{12}^2}} \\ \frac{3}{2} H^{cur}\left(\bar{\sigma}\right) \frac{\sigma_{12}}{\sqrt{\left(\sigma_{11} - \sigma_{22}\right)^2 + 3\sigma_{12}^2}} \end{bmatrix}. \tag{5.14}$$

Therefore, for forward transformation

$$\varepsilon_{11} = \alpha\left(T - T_0\right) + \left(\frac{1-\xi}{E^A} + \frac{\xi}{E^M}\right)\sigma_{11} + \nu\left(\frac{\xi-1}{E^A} - \frac{\xi}{E^M}\right)\sigma_{22} + \\ + \frac{1}{2}\xi H^{cur}\left(\bar{\sigma}\right)\frac{2\sigma_{11} - \sigma_{22}}{\sqrt{\left(\sigma_{11} - \sigma_{22}\right)^2 + 3\sigma_{12}^2}}, \tag{5.15}$$

$$\varepsilon_{22} = \alpha\left(T - T_0\right) + \nu\left(\frac{\xi-1}{E^A} - \frac{\xi}{E^M}\right)\sigma_{11} + \left(\frac{1-\xi}{E^A} + \frac{\xi}{E^M}\right)\sigma_{22} + \\ + \frac{1}{2}\xi H^{cur}\left(\bar{\sigma}\right)\frac{2\sigma_{22} - \sigma_{11}}{\sqrt{\left(\sigma_{11} - \sigma_{22}\right)^2 + 3\sigma_{12}^2}}, \tag{5.16}$$

$$\varepsilon_{12} = \left(1+\nu\right)\left(\frac{1-\xi}{E^A} + \frac{\xi}{E^M}\right)\sigma_{12} + \frac{3}{2}\xi H^{cur}\left(\bar{\sigma}\right)\frac{\sigma_{12}}{\sqrt{\left(\sigma_{11} - \sigma_{22}\right)^2 + 3\sigma_{12}^2}}. \tag{5.17}$$

For reverse transformation, $\boldsymbol{\Lambda^t_{rev}}$ is dependent only on the transformation strain and total martensitic volume fraction at the beginning of reverse transformation, ε^{t-r} and ξ^r (see Equation (1.55)). It is assumed that at the beginning of localized heating the material is at the fully saturated martensite phase, thus $\xi^r = 1$; ε^{t-r} is known from the experiment. For 2-D and for $\xi^r = 1$, $\boldsymbol{\Lambda^t_{rev}}$ is written as

$$\boldsymbol{\Lambda^t_{rev}} = \begin{bmatrix} \Lambda^{t\ 11}_{rev} \\ \Lambda^{t\ 22}_{rev} \\ \Lambda^{t\ 12}_{rev} \end{bmatrix} = \begin{bmatrix} \varepsilon^{t-r}_{11} \\ \varepsilon^{t-r}_{22} \\ \varepsilon^{t-r}_{12} \end{bmatrix}. \tag{5.18}$$

Therefore, for reverse transformation transformation

$$\varepsilon_{11} = \alpha\left(T - T_0\right) + \left(\frac{1-\xi}{E^A} + \frac{\xi}{E^M}\right)\sigma_{11} + \nu\left(\frac{\xi-1}{E^A} - \frac{\xi}{E^M}\right)\sigma_{22} + \xi\varepsilon^{t-r}_{11}, \tag{5.19}$$

$$\varepsilon_{22} = \alpha\left(T - T_0\right) + \nu\left(\frac{\xi - 1}{E^A} - \frac{\xi}{E^M}\right)\sigma_{11} + \left(\frac{1-\xi}{E^A} + \frac{\xi}{E^M}\right)\sigma_{22} + \xi\varepsilon_{22}^{t-r}, \tag{5.20}$$

$$\varepsilon_{12} = (1+\nu)\left(\frac{1-\xi}{E^A} + \frac{\xi}{E^M}\right)\sigma_{12} + \xi\varepsilon_{12}^{t-r}. \tag{5.21}$$

The final step in the 2-D reduction of the constitutive model is to reduce Equations (1.61) to the 2-D form. Substituting Equation (1.53) to the expression for π^t (see Equation (1.59)) and assuming that $\boldsymbol{\Delta\alpha}$ and Δc are negligible (a common engineering assumption, c.f. D. Lagoudas et al. (2012)) gives

$$\pi^t = \boldsymbol{\sigma} : \boldsymbol{\Lambda^t} + \frac{1}{2}\boldsymbol{\sigma} : \mathbf{\Delta S}\boldsymbol{\sigma} + \rho\Delta s_0 T - \rho\Delta u_0 - f^t. \tag{5.22}$$

By definition, $\mathbf{\Delta S} = \mathbf{S^M} - \mathbf{S^A}$, which for plane stress is written as (see Equation (5.7))

$$\mathbf{\Delta S} = \begin{bmatrix} \frac{1}{E^M} - \frac{1}{E^A} & \frac{\nu}{E^A} - \frac{\nu}{E^M} & 0 \\ \frac{\nu}{E^A} - \frac{\nu}{E^M} & \frac{1}{E^M} - \frac{1}{E^A} & 0 \\ 0 & 0 & \frac{(1+\nu)}{E^M} - \frac{(1+\nu)}{E^A} \end{bmatrix}. \tag{5.23}$$

During forward phase transformation, Equation (5.22) becomes

$$\begin{aligned}\pi^t_{fwd} = &\frac{1}{2}\sigma_{11}H^{cur}\left(\bar{\sigma}\right)\frac{2\sigma_{11}-\sigma_{22}}{\sqrt{\left(\sigma_{11}-\sigma_{22}\right)^2+3\sigma_{12}^2}}+\\ &+\frac{1}{2}\sigma_{22}H^{cur}\left(\bar{\sigma}\right)\frac{2\sigma_{22}-\sigma_{11}}{\sqrt{\left(\sigma_{11}-\sigma_{22}\right)^2+3\sigma_{12}^2}}+\\ &+\frac{3}{2}H^{cur}\left(\bar{\sigma}\right)\frac{\sigma_{12}^2}{\sqrt{\left(\sigma_{11}-\sigma_{22}\right)^2+3\sigma_{12}^2}}+\\ &+\frac{1}{2}\left(\frac{1}{E^M}-\frac{1}{E^A}\right)\left(\sigma_{11}^2+\sigma_{22}^2-2\nu\sigma_{11}\sigma_{22}+\left(1+\nu\right)\sigma_{12}^2\right)+\\ &+\rho\Delta s_0\left(T+\xi\left(M_s-M_f\right)-\frac{M_s+A_f}{2}+\frac{M_f-M_s-A_f+A_s}{4}\right),\end{aligned} \tag{5.24}$$

and the transformation function during forward transformation for plane stress becomes

$$\begin{aligned}\Phi^t_{fwd} = 0 = &\sigma_{11}\frac{\left(1-D\right)}{2}H^{cur}\left(\bar{\sigma}\right)\frac{2\sigma_{11}-\sigma_{22}}{\sqrt{\left(\sigma_{11}-\sigma_{22}\right)^2+3\sigma_{12}^2}}+\\ &+\sigma_{22}\frac{\left(1-D\right)}{2}H^{cur}\left(\bar{\sigma}\right)\frac{2\sigma_{22}-\sigma_{11}}{\sqrt{\left(\sigma_{11}-\sigma_{22}\right)^2+3\sigma_{12}^2}}+\\ &+\frac{3}{2}\frac{\sigma_{12}^2\left(1-D\right)H^{cur}\left(\bar{\sigma}\right)}{\sqrt{\left(\sigma_{11}-\sigma_{22}\right)^2+3\sigma_{12}^2}}+\\ &+\frac{1}{2}\left(\frac{1}{E^M}-\frac{1}{E^A}\right)\left(\sigma_{11}^2+\sigma_{22}^2-2\nu\sigma_{11}\sigma_{22}+\left(1+\nu\right)\sigma_{12}^2\right)+\\ &+\rho\Delta s_0\left(T+\xi\left(M_s-M_f\right)-M_s\right).\end{aligned} \tag{5.25}$$

Similarly, during reverse transformation the thermodynamic driving force is

$$\pi_{rev}^{t} = \sigma_{11}\varepsilon_{11}^{t-r} + \sigma_{22}\varepsilon_{22}^{t-r} + \sigma_{12}\varepsilon_{12}^{t-r} + \frac{1}{2}\left(\frac{1}{E^M} - \frac{1}{E^A}\right)\sigma_{11}^2 + \\ + \frac{1}{2}\left(\frac{1}{E^M} - \frac{1}{E^A}\right)\sigma_{22}^2 + \left(\frac{\nu}{E^A} - \frac{\nu}{E^M}\right)\sigma_{11}\sigma_{22} + \frac{(1+\nu)}{2}\left(\frac{1}{E^M} - \frac{1}{E^A}\right)\sigma_{12}^2 + \\ + \rho\Delta s_0\left[T + \xi\left(A_f - A_s\right) - \frac{M_s + A_f}{2} + \frac{M_s - M_f - A_f + A_s}{4}\right], \tag{5.26}$$

and the transformation function during reverse transformation for plane stress is written as

$$\Phi_{rev}^{t} = 0 = -\sigma_{11}\varepsilon_{11}^{t-r} - \sigma_{22}\varepsilon_{22}^{t-r} - \sigma_{12}\varepsilon_{12}^{t-r} + \frac{1}{2}(1+D)\left(\frac{1}{E^A} - \frac{1}{E^M}\right)\sigma_{11}^2 + \\ + \frac{1}{2}(1+D)\left(\frac{1}{E^A} - \frac{1}{E^M}\right)\sigma_{22}^2 + (1+D)\left(\frac{\nu}{E^M} - \frac{\nu}{E^A}\right)\sigma_{11}\sigma_{22} + \\ + (1+D)\frac{(1+\nu)}{2}\left(\frac{1}{E^A} - \frac{1}{E^M}\right)\sigma_{12}^2 + \rho\Delta s_0\left[A_f - T + \xi\left(A_s - A_f\right)\right]. \tag{5.27}$$

5.3.3 Model parameters calibration

Several terms have been introduced in the constitutive model which must be calibrated, including $H^{cur}(\bar{\sigma})$, $\rho\Delta s_0$, and D. These parameters are calibrated using the results from uniaxial loading, and therefore the constitutive model is reduced to the uniaxial loading case, i.e., $\sigma_{11} \neq 0$, all other $\sigma_{ij} = 0$. Calibration is largely based on the phase diagram (see Figure 5.3) obtained from uniaxial ambient heating/cooling experiment results. While the phase diagram was obtained by uniaxial experiments (i.e., $\bar{\sigma} = \sigma_{11}$), it is extended to represent the transformation surfaces based on the level of effective applied stress ($\bar{\sigma}$).

The maximum achievable transformation strain, $H^{cur}(\bar{\sigma})$, for a material at a given value of effective stress $\bar{\sigma}$ may be modeled as (D. Lagoudas et al., 2012)

$$H^{cur}\left(\bar{\sigma}\right) = H_{min} + \left(H_{sat} - H_{min}\right)\left(1 - e^{-k(\bar{\sigma}-\bar{\sigma}_{crit})}\right), \tag{5.28}$$

where H_{min} and H_{sat} are constant values which represent the absolute minimum and maximum transformation strain for the material. $\bar{\sigma}_{crit}$ is the minimum stress level at which non-zero transformation may occur.

For the thin strip and plate experiments, the parameters of $H^{cur}(\bar{\sigma})$ were determined based on the data obtained by uniaxial isobaric ambient heating/cooling of the plate specimen (see Figure 2.6). Two data points for $H^{cur}(\bar{\sigma})$ were obtained by these experiments, and are shown in Table 5.1. H_{min} is not known from the experiment, but is assumed as zero which is a common result for untrained equiatomic NiTi (Bo & Lagoudas, 1999) (Miller & Lagoudas, 2001). Furthermore, $\bar{\sigma}_{crit}$ must be between zero and the minimum stress level used to obtain the data (see Table 5.1). Figure 5.9 shows $H^{cur}(\bar{\sigma})$ for different possible values of $\bar{\sigma}_{crit}$ for the thin strip specimen; Figure 5.10 shows the same plot for the plate specimen. In Figure 5.9, a reasonable result is seen by the $\bar{\sigma}_{crit}$ range (0, 60) MPa, and any value in this range may be used; for this work, the value $\bar{\sigma}_{crit} = 40$ MPa was used. For the plate specimen, similarly, the value $\bar{\sigma}_{crit} = 40$ MPa was used which is similar to a value reported previously for untrained equiatomic NiTi (Bo & Lagoudas, 1999). Finally, k and H_{sat} were calculated to be 0.0148 and 0.044, respectively for the thin strip specimen, and 0.042 and 0.046, respectively, for the plate specimen.

$\bar{\sigma}$ (MPa)	$H^{cur}(\bar{\sigma})$
100 (Test 16)	0.026
200 (Test 16)	0.040
100 (Test 17)	0.045
200 (Test 17)	0.046

Table 5.1: $H^{cur}(\bar{\sigma})$ data obtained by ambient heating/cooling of the specimens.

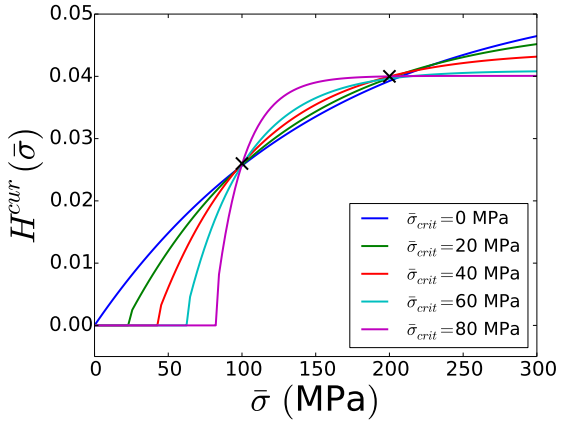

Figure 5.9: The dependence of maximum transformation on the applied stress for the thin strip specimen. $H^{cur}(\bar{\sigma})$ is shown with several different possible values of $\bar{\sigma}_{crit}$. The experimental data points are indicated on the figure (see Table 5.1).

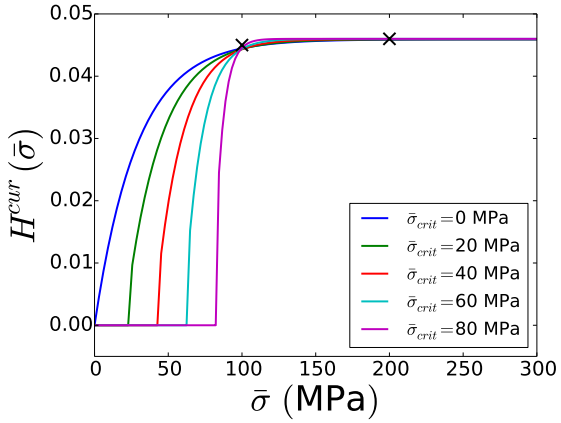

Figure 5.10: The dependence of maximum transformation on the applied stress. $H^{cur}(\bar{\sigma})$ is shown with several different possible values of $\bar{\sigma}_{crit}$. The experimental data points are indicated on the figure (see Table 5.1).

The transformation surfaces from the phase diagram represent the stress-temperature derivatives, derived in D. Lagoudas et al. (2012) after the uniaxial assumption as

$$\left.\frac{d\sigma}{dT}\right|_{\sigma=\sigma^*,\,\dot{\xi}>0} = \left.\frac{-\rho\Delta s_0}{\Lambda^t + \sigma\frac{\partial\Lambda^t_{fwd}}{\partial\sigma} + \sigma\left(\frac{1}{E^M}-\frac{1}{E^A}\right) + \frac{\partial Y^t_{fwd}}{\partial\sigma}}\right|_{\sigma=\sigma^*}, \tag{5.29}$$

$$\left.\frac{d\sigma}{dT}\right|_{\sigma=\sigma^*,\,\dot{\xi}<0} = \left.\frac{-\rho\Delta s_0}{\Lambda^t + \sigma\frac{\partial\Lambda^t_{rev}}{\partial\sigma} + \sigma\left(\frac{1}{E^M}-\frac{1}{E^A}\right) + \frac{\partial Y^t_{rev}}{\partial\sigma}}\right|_{\sigma=\sigma^*}, \tag{5.30}$$

where σ^* may be any reference stress for identification of the slope of the transformation surfaces from the phase diagram, $C^{A,\,M}$. The ambient heating/cooling experiments were performed under the assumption that full transformation had occurred in either direction, thus $\Lambda^t_{fwd} = \Lambda^t_{rev}$. Therefore, Equation (1.63) may be written as (D. Lagoudas et al., 2012)

$$Y^t_{fwd} = Y^t_{rev} = Y^t_0 + D\sigma^* H^{cur}\left(\sigma^*\right). \tag{5.31}$$

Equations (5.29) and (5.30) can now be rewritten as

$$C^M = \left.\frac{-\rho\Delta s_0}{(1-D)\left(\Lambda^t + \sigma\frac{\partial\Lambda^t}{\partial\sigma}\right) + \sigma\left(\frac{1}{E^M}-\frac{1}{E^A}\right)}\right|_{\sigma=\sigma^*}, \tag{5.32}$$

$$C^M = \left.\frac{-\rho\Delta s_0}{(1+D)\left(\Lambda^t + \sigma\frac{\partial\Lambda^t}{\partial\sigma}\right) + \sigma\left(\frac{1}{E^M}-\frac{1}{E^A}\right)}\right|_{\sigma=\sigma^*}, \tag{5.33}$$

where $C^{A,\,M}$ are known from the experiment. These equations may be solved to give the calibrated values of $\rho\Delta s_0$ and D:

$$\rho\Delta s_0 = \left.\frac{-2\left(C^M C^A\right)\left[H^{cur}(\sigma) + \sigma\frac{\partial H^{cur}(\sigma)}{\partial\sigma} + \sigma\left(\frac{1}{E^M} - \frac{1}{E^A}\right)\right]}{C^M + C^A}\right|_{\sigma=\sigma^*},$$
$$D = \left.\frac{\left(C^M - C^A\right)\left[H^{cur}(\sigma) + \sigma\frac{\partial H^{cur}(\sigma)}{\partial\sigma} + \sigma\left(\frac{1}{E^M} - \frac{1}{E^A}\right)\right]}{\left(C^M + C^A\right)\left[H^{cur}(\sigma) + \sigma\frac{\partial H^{cur}(\sigma)}{\partial\sigma}\right]}\right|_{\sigma=\sigma^*}. \tag{5.34}$$

5.3.4 Results

The results of the thin strip specimen stress estimation is shown in Figure 5.11, which demonstrates the stress field at each time step during the localized heating experiment for the thin strip specimen. During the progression of localized heating the stress field started from a homogeneous 200 MPa, and was redistributed due to effects of thermal expansion. Note that the resolution of the stress estimation fields reported in Figure 5.11 is 0.360 mm per analysis point.

Figure 5.12 also demonstrates the variation in martensitic volume fraction after each time step.

The results demonstrate a reasonable first approximation stress estimation. The σ_{11} stress field was expected to maintain a constant 200 MPa during the experiment. Figure 5.11b shows that this is true with the exception of some errors of calculation. The σ_{22} stress field was expected to remain at approximately 0 MPa except the areas close to the grips (the areas close to the grips are outside the region shown in the analysis); Figure 5.11a shows that the σ_{11} field remains at approximately 0 MPa. Note that this is a first iteration of the stress estimation calculation, and demonstrates that this calculation may provide a good approximation of the stress field. The accuracy of the isotropic model has not been assessed relative to the expected anisotropy of the rolled sheet, due to phase transformation.

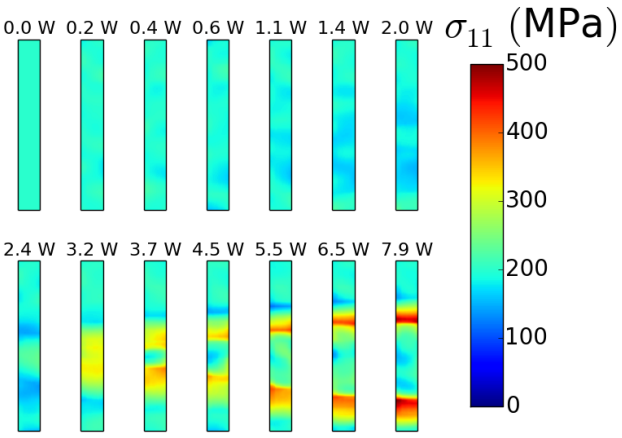

(a) Axial stress, σ_{11}.

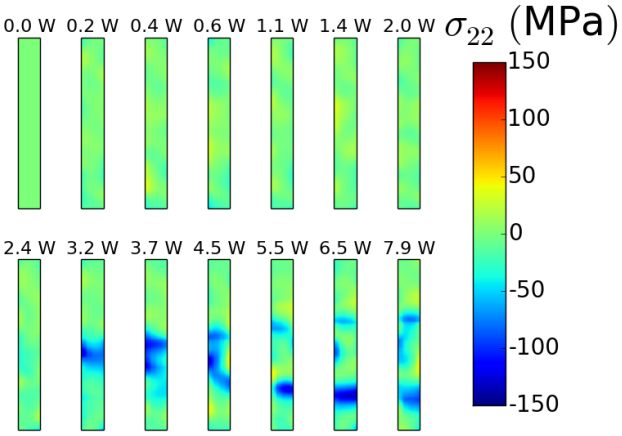

(b) Transverse stress, σ_{22}.

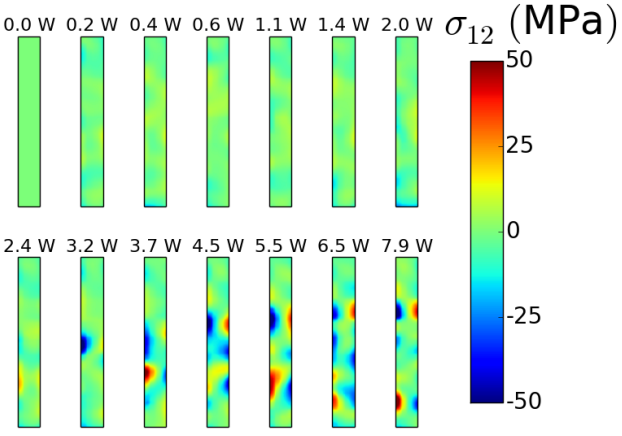

(c) Shear stress, σ_{12}.

Figure 5.11: An estimation of the stress field at each time step for the thin strip specimen during the reverse transformation stage of the localized heating experiment.

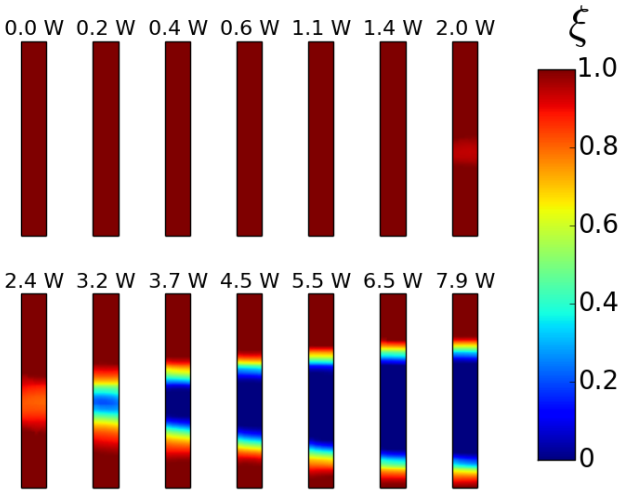

Figure 5.12: The martensitic volume fraction distribution for the thin strip specimen is shown for each time step according to the constitutive model calibration based on strain and temperature data.

For the plate specimen, the results of the stress estimation is shown in Figure 5.13. Again, during the progression of localized heating the stress field started from a homogeneous 200 MPa, and was redistributed due to effects of thermal expansion. For this test, unlike the thin strip specimen, for the plate specimen at the onset of phase transformation, a significant stress increase occurred in the region surrounding the transformed material. Note that the resolution of the stress estimation fields reported in Figure 5.13 is 0.360 mm per analysis point.

Figure 5.14 also demonstrates the variation in martensitic volume fraction after each time step, for the plate specimen.

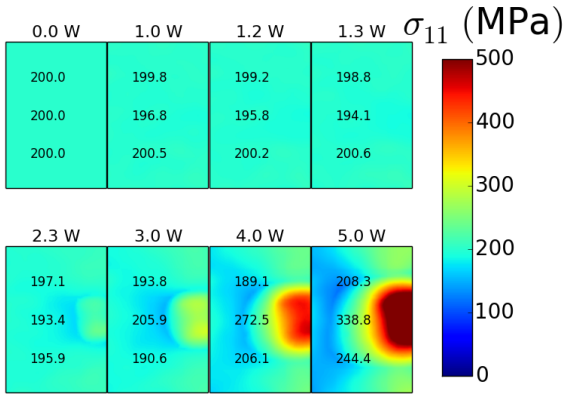

(a) Axial stress, σ_{11}. The average stress across the width of the specimen is shown at three points for each time step (frame). Note that ideally, the average stress across the width is $\bar{\sigma_{11}}$ =200 MPa.

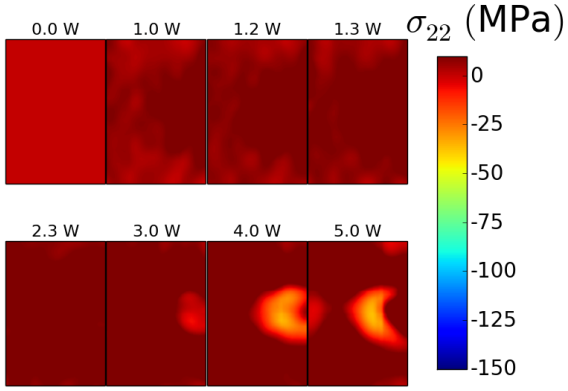

(b) Transverse stress, σ_{22}

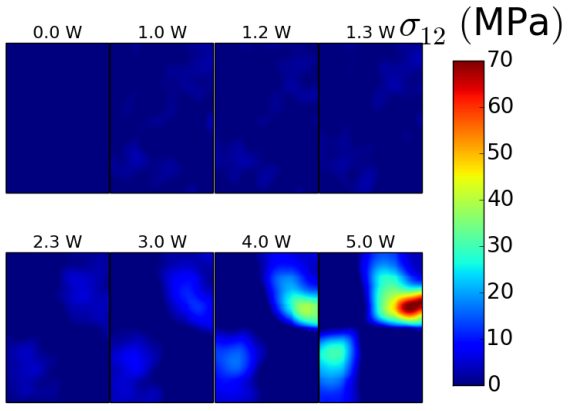

(c) Shear stress, σ_{12}

Figure 5.13: An estimation of the stress field at each time step for the plate specimen during the reverse transformation stage of the localized heating experiment.

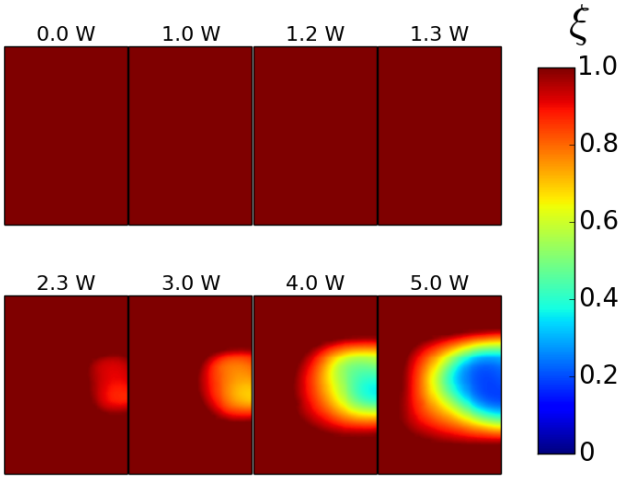

Figure 5.14: The martensitic volume fraction distribution for the plate specimen is shown for each time step according to the constitutive model calibration based on strain and temperature data.

The constitutive model formulation uses the assumption that the SMA is isotropic. The accuracy of the isotropic model has not been assessed relative to the expected anisotropy of the rolled sheet, due to phase transformation. Therefore, the average stress written across the width of the specimen in Figure 5.13a is not consistently 200 MPa on average.

Stress at the beginning of localized heating was approximated as being $\sigma_y = 200$ MPa, $\sigma_x = 0$ MPa, and $\sigma_{xy} = 0$ MPa which assumptions are consistent with the results of calculating the stress distribution in the specimen based on strain data at the end of elastic loading at austenite from 10 MPa to 200 MPa. Figure 5.15 shows the stress distribution for σ_y, σ_x, and σ_{xy} at the end of elastic loading, which are consistent with the assumption.

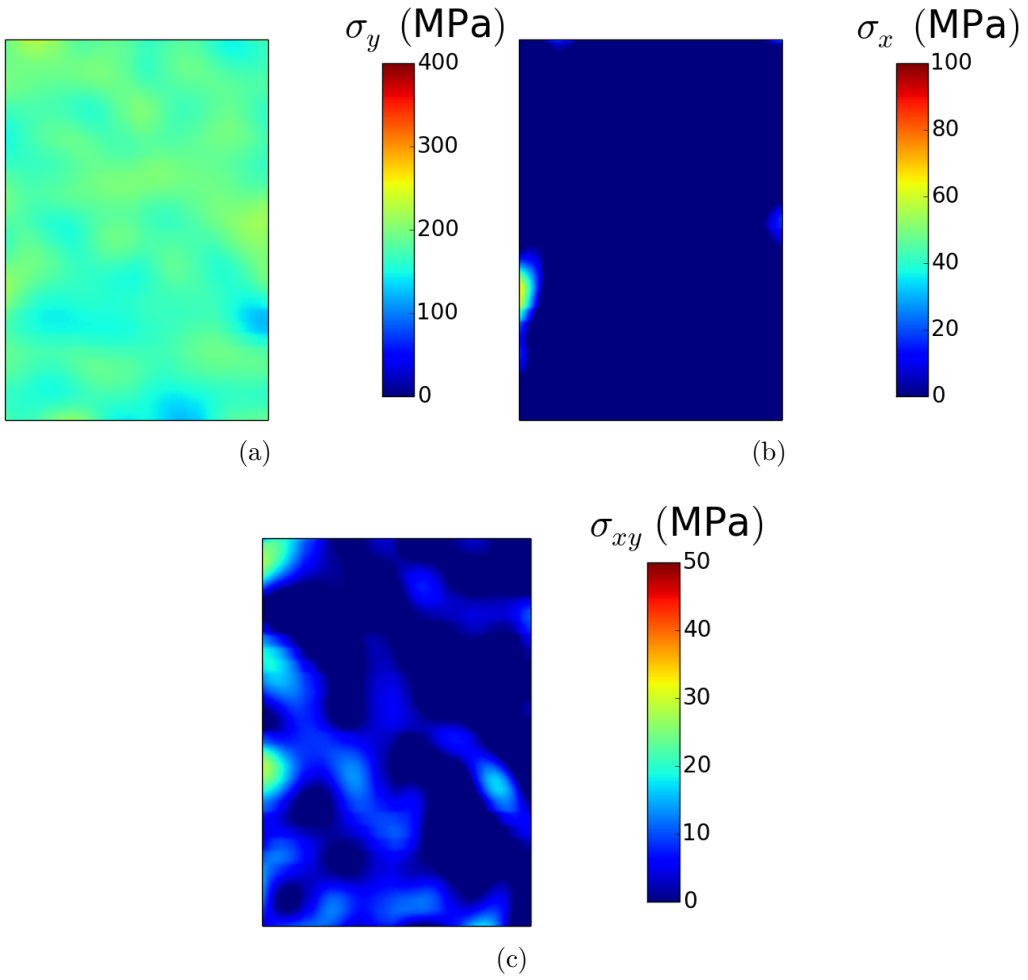

Figure 5.15: Stress distribution in the specimen after elastic loading in the austenite state.

5.4 Summary and conclusions

A reduction of the 3D SMA constitutive model of D. Lagoudas et al. (2012) has been reviewed, and a reduction has been made to the 2D form. The stress state in the specimen has been calculated from the full-field strain and temperature response in the specimen.

This method for estimating the stress field is a special contribution to experimental methods using full-field measurements. A similar algorithm may be used in the future for estimating the stress field in specimens with heterogeneous loads by post processing of full-field strain measurements.

6. CONCLUSION

6.1 Summary

A short summary of this thesis is presented here. Section 1 provides the motivation for this experimental work, presents an introduction to SMAs, and reviews existing methods for characterization of SMAs. In Section 2, a series of experiments were performed and analyzed that characterize the localized behavior of actuator SMAs by localized heating. Section 3 demonstrates the wealth of information that may be obtained by performing DIC analysis of a uniaxial experiment on an SMA with non-standard geometry. In Section 4, a method of characterizing microscopic SMAs for a particular application is presented. Finally, in Section 5 a stress estimation is performed for the experiments described in Section 2, based on the full-field strain and temperature data provided.

6.2 Synthesis

In this thesis, novel methods for characterizing SMA materials are described which utilize modern experimental measurement techniques, in particular, DIC and infra-red thermography. Each experiment designed and its particular application for measurement of SMA phenomenological behavior is of great value to the SMA community. These streamlined methods demonstrate particular methods for obtaining a plethora of information from limited numbers of experiments for SMAs. This thesis has attempted to demonstrate this style of characterization in three different common applications of SMAs. First, SMAs are commonly used as actuators, in which an SMA device is perturbed by a change in temperature, resulting in the desired actuation. Commonly, the heat is applied in a localized manner. Int is quite useful therefore to perform characterization of SMA actuators by localized application

of heat, in addition to the diversity of information obtainable by localized heating. Furthermore, pseudoelastic SMAs are commonly utilized for spring-damping systems or for sensory applications. It is desirable to provide an efficient and accurate method for characterizing pseudoelastic SMAs in applications where the devices undergo loading along multiple stress axes. Section 3 shows such a characterization method in a highly detailed manner. Furthermore, microscopic SMA particles may be utilized, especially in sensory applications. Hence, Section 4 presents an introduction to characterization of microscopic SMA particles via DIC, with preliminary results. This shows the synthesis of the various experiments performed, and the specific contribution of the work to the SMA experimental community as a whole.

Furthermore, the power of the techniques used in this work is demonstrated by the analyses performed in Section 5; previously stress estimation of non-uniformly loaded material specimens was not possible. However, with the current methods for deformation measurement, specimens no longer need to have uniform stress through the regions of interest, and all of the information including errors in measurement may be mitigated by the high fidelity and great volume of local and global measurements alike demonstrated by the techniques used here.

6.3 Future work

The experiments described ere provide excellent motivation for future work in this specific area of research. The methods described here may be utilized for a wide range of SMA studies. Furthermore, a detailed analysis of the cooperative use of different measurement techniques has not been done here; specifically, a more detailed analysis of errors which arise due to combined measurements and/or experimental techniques would be particularly beneficial.

Some particular areas which may be improved upon are described here. First,

the characterization experiments performed for SMA actuator materials (Section 2) were performed using limited resources. The samples available for the experimental process were limited, and only the two mentioned tests (thin strip and plate specimen) were performed in part because no alternative materials were available. In general, these materials are sufficient to present the intricacies of this characterization method, but to demonstrate the power of the method, multiple materials should be utilized. Second, only a limited analysis of the material (e.g., ambient heating/cooling experiments) were performed for this study. In future studies of this particular method, and especially concerning error analysis for the method, special attention should be given to experiments which serve to describe the material and/or validate the localized heating method, and would thus demonstrate the reliability of the localized heating method. Third, digital image correlation (DIC) measurement was performed using 2D-DIC, which in itself has several limiting factors (see Section 3 for the errors which may arise due to 2D-DIC measurements). The 3D-DIC method would be preferred in any future application of this work. Similarly, IR thermography images were captured at different intervals during the experiment, and a finite number of images were captured. It would be preferable to obtain a larger number (100's) of IR images to reduce the time step between each analysis. This would increase the knowledge of the material behavior to the localized heating. As a similar point, localized power input to the specimen should be performed continuously instead of in a quasistatic manner to better simulate actuator performance and increase the accuracy of the material characterization (e.g., thermal conductivity).

Future experiments are planned for the multi-axial loading of pseudoelastic SMAs. In particular, biaxial loading of cruxiform specimens is planned for the future so that more information may be obtained regarding the anisotropic transformation behavior of the material. Furthermore, biaxial loading should be performed in tension-tension,

tension-compression, as well as compression-compression to obtain the highest level of understanding of the anisotropic material behavior. Also, tests should be performed which are an analysis of the yielding and fracture behavior of the material, which are also predicted as anisotropic. In the past, experiments have been performed using 2D-DIC, however, it would be ideal for such experiments to be performed using 3D-DIC. These tests are an introduction to testing of SMA's using heterogeneous geometries and has been done for NiTi; this concept should also be implemented in the future for a wider variety of SMA materials.

Characterization of the microscopic SMA materials is an ongoing topic of research at the NASA Langley Research Center. A lot of attention is currently being given to finding a more appropriate patterning technique for performing microscopic 3D-DIC through a microscope lens. Furthermore, Future efforts should be made to obtain a detailed analysis of the stress field around the crack tip from the DIC data so that a complete understanding of the mechanics surrounding the microscopic SMA particles is achieved. In this way, a more detailed characterization of the SMA material being used may be performed.

6.4 Conclusion

This thesis presents an overview of phenomenal methods for characterizing SMAs, particularly attesting to the power of DIC, and demonstrating the combined use of DIC and infra-red thermography. The methods are designed to reduce the number of experiments necessary for characterization compared to traditional characterization methods, as well as provide accurate and detailed information for each type of characterization.

REFERENCES

Anand, L., & Gurtin, M. E. (2003). Thermal effects in the superelasticity of crystalline shape-memory materials. *Journal of the Mechanics and Physics of Solids*, *51*(6), 1015 - 1058.

ASTM Standard F2004. (2010). *Test method for transformation temperature of nickel-titanium alloys by thermal analysis.* ASTM International, West Conshohocken, PA.

ASTM Standard F2005. (2005). *Standard terminology for nickel-titanium shape memory alloys.* ASTM International, West Conshohocken, PA.

ASTM Standard F2082. (2006). *Test method for determination of transformation temperature of nickel-titanium shape memory alloys by bend and free recovery.* ASTM International, West Conshohocken, PA.

Auricchio, F., Taylor, R. L., & Lubliner, J. (1997). Shape-memory alloys: Macro-modelling and numerical simulations of the superelastic behavior. *Computer Methods in Applied Mechanics and Engineering*, *146*(3), 281–312.

Avril, S., Bonnet, M., Bretelle, A.-S., Grdiac, M., Hild, F., et al. (2008). Overview of identification methods of mechanical parameters based on full-field measurements. *Experimental Mechanics*, *48*(4), 381-402.

Bay, B., Smith, T., Fyhrie, D., & Saad, M. (1999). Digital volume correlation: Three-dimensional strain mapping using X-ray tomography. *Experimental Mechanics*, *39*(3), 217-226.

Berfield, T., Patel, J., Shimmin, R., Braun, P., Lambros, J., & Sottos, N. (2007). Micro-and nanoscale deformation measurement of surface and internal planes via digital image correlation. *Experimental Mechanics*, *47*(1), 51–62.

Bo, Z., & Lagoudas, D. C. (1999). Thermomechanical modeling of polycrystalline SMAs under cyclic loading, Part I: Theoretical derivations. *International Journal of Engineering Science*, *37*(9), 1089–1140.

Bogdanoff, P., & Fultz, B. (2001). The role of phonons in the thermodynamics of the martensitic transformation in NiTi. *Philosophical Magazine B: Physics of Condensed Matter; Statistical Mechanics, Electronic, Optical and Magnetic Properties*, *81*(3), 299 - 311.

Boley, B., & Weiner, J. (1960). *Theory of thermal stresses*. Hoboken, NJ: John Wiley & Sons, Inc.

Boyd, J. G., & Lagoudas, D. C. (1996). A thermodynamical constitutive model for shape memory materials. Part I. the monolithic shape memory alloy. *International Journal of Plasticity*, *12*(6), 805–842.

Brinson, L., Bekker, A., & Hwang, S. (1996). Deformation of shape memory alloys due to thermo-induced transformation. *Journal of Intelligent Material Systems and Structures*, *7*(1), 97-107.

Bromley, R. (1956). Two-dimensional strain measurement by moiré. *Proceedings of the Physical Society. Section B*, *69*(3), 373-381.

Bushnell, G. S., Arbogast, D., & Ruggeri, R. (2008). Shape control of a morphing structure (rotor blade) using a shape memory alloy actuator system. In *The 15th International Symposium on: Smart Structures and Materials & Nondestructive Evaluation and Health Monitoring* (pp. 69282A–69282A). SPIE.

Calkins, F. T., & Mabe, J. H. (2010). Shape memory alloy based morphing aerostructures. *Journal of Mechanical Design*, *132*(11), 111012.

Chimisky, Y., Meraghni, F., Echchorfi, R., Cornell, S., & Bourgeois, N. (2013). Identification of model parameters for the simulation of SMA structures using full field measurements. In *ASME 2013 Conference on Smart Materials, Adaptive*

Structures and Intelligent Systems.

Christensen, R. (1979). *Mechanics of composite materials.* Hoboken, NJ: John Wiley & Sons, Inc.

Churchill, C., Shaw, J., & Iadicola, M. (2009a). Tips and tricks for characterizing shape memory alloy wire Part II: Fundamental isothermal responses. *Experimental Techniques*, *33*(1), 51–62.

Churchill, C., Shaw, J., & Iadicola, M. (2009b). Tips and tricks for characterizing shape memory alloy wire Part III: Localization and propagation phenomena. *Experimental Techniques*, *33*(5), 70–78.

Churchill, C., Shaw, J., & Iadicola, M. (2010). Tips and tricks for characterizing shape memory alloy wire Part IV: Thermo-mechanical coupling. *Experimental Techniques*, *34*(2), 63–80.

Clingman, D. J., Calkins, F. T., & Smith, J. P. (2003). Thermomechanical properties of ni 60% weight ti 40% weight. In *Smart Structures and Materials 2003. Active Materials: Behaviour and Mechanics, 3-6 March 2003* (pp. 219–229). SPIE-International Society of Optical Engineering.

Coimbra, D., Greenwood, R., & Kendall, K. (2000). Tensile testing of ceramic fibres by video extensometry. *Journal of Materials Science*, *35*(13), 3341-3345.

Coleman, B., & Noll, W. (1963). The thermodynamics of elastic materials with heat conduction and viscosity. *Archive for Rational Mechanics and Analysis*, *13*(1), 167-178.

Cornell, S. R., Leser, W. P., Hochhalter, J. D., Newman, J. A., & Hartl, D. J. (2014). Development and characterization of embedded sensory particles using multi-scale 3d digital image correlation. In *ASME 2014 Conference on Smart Materials, Adaptive Structures and Intelligent Systems* (p. V002T02A010).

Correlated Solutions, Inc. (2014). *Correlated Solutions VIC-2D Software.* Retrieved

May 2014, from www.correlatedsolutions.com/vic-2d/

Dally, J., & Read, D. (1993). Electron beam moiré. *Experimental Mechanics*, *33*(4), 270–277.

Dally, J., & Sanford, R. (1987). Strain-gage methods for measuring the opening-mode stress-intensity factor, KI. *Experimental Mechanics*, *27*(4), 381–388.

De Almeida, O., Lagattu, F., & Brillaud, J. (2008). Analysis by a 3D-DIC technique of volumetric deformation gradients: Application to polypropylene/EPR/talc composites. *Composites Part A: Applied Science and Manufacturing*, *39*(8), 1210 - 1217.

Doyle, F. (1964). Historical development of analytical photogrammetry. *Photogrammetric Engineering*, *30*(2), 254 - 265.

Francois, P., Gaucher, V., & Seguela, R. (1994). Local-scale analysis of the longitudinal strains in strongly necking materials by means of video-controlled extensometry. *Journal of Physics: Condensed Matter*, *6*(42), 8959.

Frick, C., Ortega, A., Tyber, J., Gall, K., & Maier, H. (2004). Multiscale structure and properties of cast and deformation processed polycrystalline NiTi shape-memory alloys. *Metallurgical and Materials Transactions A*, *35*(7), 2013–2025.

Gall, K., Sehitoglu, H., Anderson, R., Karaman, I., Chumlyakov, Y. I., & Kireeva, I. V. (2001). On the mechanical behavior of single crystal NiTi shape memory alloys and related polycrystalline phenomenon. *Materials Science and Engineering*, *317*(1), 85–92.

Gao, X., & Brinson, L. C. (2002). A simplified multivariant SMA model based on invariant plane nature of martensitic transformation. *Journal of Intelligent Material Systems and Structures*, *13*(12), 795–810.

G'Sell, C., Hiver, J., Dahoun, A., & Souahi, A. (1992). Video-controlled tensile testing of polymers and metals beyond the necking point. *Journal of Materials*

Science, *27*(18), 5031–5039.

Gupta, V. K., Willard, S. A., Hochhalter, J. D., & Smith, S. W. (2014). Microstructure-scale in-situ correlation-based study of grain deformation and crack tip displacements in al-cu alloys. *Materials Performance and Characterization*, *In Review*.

Hall, E. O. (1951). The deformation and ageing of mild steel, part II: Characteristics of the Lüders deformation. *Proceedings of the Physical Society. Section B*, *64*(9).

Hartl, D., Lagoudas, D., Calkins, F., & Mabe, J. (2010). Use of a Ni60Ti shape memory alloy for active jet engine chevron application Part I: Thermomechanical characterization. *Smart Materials and Structures*, *19*(1), 015020.

Hartl, D. J., & Lagoudas, D. C. (2007). Aerospace applications of shape memory alloys. *Proceedings of the Institution of Mechanical Engineers, Part G: Journal of Aerospace Engineering*, *221*(4), 535–552.

Hartl, D. J., Mooney, J. T., Lagoudas, D. C., Calkins, F. T., & Mabe, J. H. (2010). Use of a ni60ti shape memory alloy for active jet engine chevron application part II: Experimentally validated numerical analysis. *Smart Materials and Structures*, *19*(1), 015021.

Helm, D., & Haupt, P. (2003). Shape memory behaviour: Modelling within continuum thermomechanics. *International Journal of Solids and Structures*, *40*(4), 827 - 849.

Hiruma, Y., Aoyagi, R., Nagata, H., & Takenaka, T. (2004). Piezoelectric properties of $BaTiO_3 - (Bi_{1/2}K_{1/2})TiO_3$ ferroelectric ceramics. *Japanese Journal of Applied Physics, Part I: Regular Papers and Short Notes and Review Papers*, *43*(11R), 7556 - 7559.

Jani, J., Leary, M., Subic, A., & Gibson, M. A. (2014). A review of shape memory

alloy research, applications and opportunities. *Materials and Design*, *56*, 1078–1113.

Kammers, A., & Daly, S. (2011). Small-scale patterning methods for digital image correlation under scanning electron microscopy. *Measurement Science and Technology*, *28*(12), 125501.

Karaca, H., Karaman, I., Basaran, B., Chumlyakov, Y., & Maier, H. (2006). Magnetic field and stress induced martensite reorientation in NiMnGa ferromagnetic shape memory alloy single crystals. *Acta Materialia*, *54*(1), 233 - 245.

Lagoudas, D. (2008). *Shape memory alloys: Modeling and engineering applications*. New York, NY: Springer.

Lagoudas, D., Hartl, D., Chemisky, Y., Machado, L., & Popov, P. (2012). Constitutive model for the numerical analysis of phase transformation in polycrystalline shape memory alloys. *International Journal of Plasticity*, *32*, 155-183.

Lagoudas, D. C., Entchev, P. B., Popov, P., Patoor, E., Brinson, L. C., & Gao, X. (2006). Shape memory alloys, Part II: Modeling of polycrystals. *Mechanics of Materials*, *38*(5), 430–462.

Lagoudas, D. C., Entchev, P. B., Popov, P., Patoor, E., Brinson, L. C., et al. (2006). Shape memory alloys, Part II: Modeling of polycrystals. *Mechanics of Materials*, *38*(5), 430–462.

Lenoir, N., Bornert, M., Desrues, J., Bsuelle, P., & Viggiani, G. (2007). Volumetric digital image correlation applied to X-ray microtomography images from triaxial compression tests on argillaceous rock. *Strain*, *43*(3), 193-205.

Li, N., Guo, S., & Sutton, M. A. (2011). Recent progress in e-beam lithography for SEM patterning. In *MEMS and Nanotechnology, Volume 2* (pp. 163–166). Springer.

Lord, J., Penn, D., & Whitehead, P. (2008). The application of digital image

correlation for measuring residual stress by incremental hole drilling. *Applied Mechanics and Materials*, *13-14*, 65-73.

Lucas, B. D., Kanade, T., et al. (1981). An iterative image registration technique with an application to stereo vision. In *International Joint Conferences on Artificial Intelligence* (Vol. 81, pp. 674–679).

Machida, K., & Yamada, H. (2004). Automatic stress analyzing system by digital speckle photography using 2-D hybrid method. *Key Engineering Materials*, *270*, 800–807.

Meraghni, F., Chemisky, Y., Piotrowski, B., Echchorfi, R., Bourgeois, N., et al. (2013). Identification and interpretation of material parameters of a shape memory alloy (SMA) model. In *Proceedings of the 9th European Symposium on Martensitic Transformations, ESOMAT 2012* (Vol. 738-739, p. 276-280). Pfaffikon, Switzerland: Trans Tech Publications Ltd.

Meuwissen, M., Oomens, C., Baaijens, F., Petterson, R., & Janssen, J. (1998). Determination of the elasto-plastic properties of aluminium using a mixed numericalexperimental method. *Journal of Materials Processing Technology*, *75*(1), 204–211.

Miller, D. A., & Lagoudas, D. C. (2001). Influence of cold work and heat treatment on the shape memory effect and plastic strain development of NiTi. *Materials Science and Engineering:*, *308*(12), 161 - 175.

Minkina, W., & Dudzik, S. (2009). *Infrared thermography: Errors and uncertainties.* Hoboken, NJ: John Wiley & Sons, Ltd.

Morgan, N. B. (2004). Medical shape memory alloy applications - the market and its products. *Materials Science and Engineering*, *378*(1), 16–23.

Morgeneyer, T., Helfen, L., Mubarak, H., & Hild, F. (2013). 3D digital volume correlation of synchrotron radiation laminography images of ductile crack initiation:

An initial feasibility study. *Experimental Mechanics*, *53*(4), 543-556.

Nechval, N., Nechval, K., Purgailis, M., & Strelchonok, V. (2011). Planning inspections in the case of damage tolerance approach to service of fatigued aircraft structures. *International Journal of Performability Engineering*, *7*(3), 279.

Nishioka, T., Kurio, K., & Nakabayashi, H. (2000). An intelligent hybrid method to automatically detect and eliminate experimental measurement errors for linear elastic deformation fields. *Experimental Mechanics*, *40*(2), 170–179.

Oehler, S. D., Hartl, D. J., Lopez, R., Malak, R. J., & Lagoudas, D. C. (2012). Design optimization and uncertainty analysis of SMA morphing structures. *Smart Materials and Structures*, *21*(9), 094016.

Orgéas, L., & Favier, D. (1998). Stress-induced martensitic transformation of a NiTi alloy in isothermal shear, tension and compression. *Acta Materialia*, *46*(15), 5579–5591.

Otsuka, K., & Wayman, C. M. (1999). *Shape memory materials*. New York, NY: Cambridge University Press.

Patoor, E., Eberhardt, A., & Berveiller, M. (1996). Micromechanical modelling of superelasticity in shape memory alloys. *Le Journal de Physique IV*, *6*(C1), C1–277.

Patoor, E., Lagoudas, D. C., Entchev, P. B., Brinson, L. C., & Gao, X. (2006). Shape memory alloys, Part I: General properties and modeling of single crystals. *Mechanics of Materials*, *38*(5), 391–429.

Peters, W. H., & Ranson, W. F. (1982). Digital imaging techniques in experimental stress analysis. *Optical Engineering*, *21*(3), 427-431.

Poulain, X., Kohlman, L., Binienda, W., Roberts, G., Goldberg, R., & Benzerga, A. (2013). Determination of the intrinsic behavior of polymers using digital image correlation combined with video-monitored testing. *International Journal of*

Solids and Structures, *50*(1112), 1869 - 1878.

Qidwai, M., & Lagoudas, D. (2000). On thermomechanics and transformation surfaces of polycrystalline NiTi shape memory alloy material. *International Journal of Plasticity*, *16*(1011), 1309 - 1343.

Reedlunn, B., Daly, S., Hector, L., Zavattieri, P., & Shaw, J. (2011). Tips and tricks for characterizing shape memory wire Part V: Full field strain measurement by digital image correlation. *Experimental Techniques*, *37*(3), 62–78.

Schajer, G. (2010). Advances in hole-drilling residual stress measurements. *Proceedings of the Society for Experimental Mechanics, Inc.*, *67*(2), 159-168.

Scrivens, W., Luo, Y., Sutton, M., Collette, S., Myrick, M., et al. (2007). Development of patterns for digital image correlation measurements at reduced length scales. *Experimental Mechanics*, *47*(1), 63-77.

Sebastiani, M., Eberl, C., Bemporad, E., & Pharr, G. (2011). Depth-resolved residual stress analysis of thin coatings by a new FIB-DIC method. *Materials Science and Engineering A*, *528*(27), 7901-7908.

Shaw, J., & Kyriakides, S. (1997). Initiation and propagation of localized deformation in elasto-plastic strips under uniaxial tension. *International Journal of Plasticity*, *13*(10), 837–871.

Shaw, J. A., Churchill, C. B., & Iadicola, M. (2008). Tips and tricks for characterizing shape memory alloy wire Part I: Differential scanning calorimetry and basic phenomena. *Experimental Techniques*, *32*(5), 55–62.

Shaw, J. A., & Kyriakides, S. (1995). Thermomechanical aspects of NiTi. *Journal of the Mechanics and Physics of Solids*, *43*(8), 1243–1281.

Silva, M., & Ravichandran, G. (2009). Determination of stress field in damaged composites using thermal imaging. In *24th Annual Technical Conference of the American Society for Composites 2009 and First Joint Canadian-American*

Technical Conference on Composites (Vol. 3, p. 1541 - 1549). Newark, DE.

Sutton, M., Wolters, W., Peters, W., Ranson, W., & McNeill, S. (1983). Determination of displacements using an improved digital correlation method. *Image and Vision Computing*, *1*(3), 133 - 139.

Sutton, M. A., Orteu, J.-J., & Schreier, H. W. (2009). *Image correlation for shape, motion and deformation measurements: Basic concepts, theory and applications*. New York, NY: Springer.

Van Humbeeck, J. (1999). Non-medical applications of shape memory alloys. *Materials Science and Engineering*, *273*, 134–148.

Wu, X., Sun, G., & Wu, J. (2003). The nonlinear relationship between transformation strain and applied stress for nitinol. *Materials Letters*, *57*(7), 1334 - 1338.

Zhao, Y., Lei, Z., Xing, Y., Hou, X., & Bai, P. (2014). Fabricating parameters optimization of high frequency grating by multi-scanning electron beam method. *Experimental Mechanics*, *54*(1), 45-55.